

# JMO

Journal for  
Modeling in  
Ophthalmology

**Journal for Modeling in Ophthalmology (JMO)** was created in 2014 with the aim of providing a forum for interdisciplinary approaches integrating mathematical and computational modeling techniques to address open problems in ophthalmology.

The Editorial Board members include experts in ophthalmology, physiology, mathematics, and engineering, and strive to ensure the highest scientific level of the contributions selected for publication. JMO aims to be the voice for this rapidly growing interdisciplinary research and we hope you will join us on this exciting journey.

JMO welcomes articles that use modeling techniques to investigate questions related to the anatomy, physiology, and function of the eye in health and disease.

For further information on JMO's focus and scope as well as manuscript submissions:

**[www.modeling-ophthalmology.com](http://www.modeling-ophthalmology.com)**  
**[info@modeling-ophthalmology.com](mailto:info@modeling-ophthalmology.com)**

## Copyright

Authors who publish in JMO agree to the following terms:  
a. Authors retain copyright and grant the journal JMO right of first publication, with the work twelve (12) months after publication simultaneously licensed under a Creative Commons Attribution License that allows others to share the work with an acknowledgement of the work's authorship and initial publication in JMO.

## Chief editors

Alon Harris  
Giovanna Guidoboni

## Managing editor

Giovanna Guidoboni

## Editorial board

Makoto Araie  
Fabio Benfenati  
Richard J. Braun  
Thomas Ciulla  
Vital Paulino Costa  
Ahmed Elsheikh  
Jean-Frederic Gerbeau  
Rafael Grytz  
Michaël Girard  
Gabor Hollo  
Ingrida Januleviciene  
Jost Jonas  
Larry Kagemann  
Fabian Lerner  
Anat Loewenstein  
Toru Nakazawa  
Colm O'Brien  
Anna Pandolfi  
Peter Pinsky  
Rodolfo Repetto  
Riccardo Sacco  
Einar Stefansson  
Fotis Topouzis  
Emanuele Trucco  
Zoran Vatauvuk  
Joanna Wierzbowska

## Publisher

Kugler Publications  
P.O. Box 20538  
1001 NM Amsterdam  
The Netherlands  
[info@kuglerpublications.com](mailto:info@kuglerpublications.com)  
[www.kuglerpublications.com](http://www.kuglerpublications.com)

## ISSN

Online: 2468-3930

Print: 2468-3922

## Manuscript submissions

Author guidelines and templates are available via the website, through which all manuscripts should be submitted. For inquiries please contact us via e-mail.

## Publication frequency

JMO is published four issues per year (quarterly) electronically. A selection is published in print twice a year and distributed free of charge at congresses through Kugler Publications or partners.

## Advertising inquiries

JMO offers online and in print sponsorship and advertising opportunities. Please contact Kugler Publications to for inquiries.

b. After 12 months from the date of publication, authors are able to enter into separate, additional contractual arrangements for the non-exclusive distribution of JMO's published version of the work, with an acknowledgement of its initial publication in JMO.

## Open access policy

The first volume of JMO is fully open access (after registration) without requiring any publication fee from the authors. However, we are currently evaluating various models to cover the publications costs while keeping knowledge as accessible as possible, which remains our first priority. Possible models include subscription fees, publication fees, and advertisement venues, or a combination. Please share your thoughts with us on this hot topic via e-mail.

## Disclaimers

All articles published, including editorials and letters, represent the opinions of the authors and do not reflect the official policy of JMO, its sponsors, the publisher or the institution with which the author is affiliated, unless this is clearly specified. Although every effort has been made to ensure the technical accuracy of the contents of JMO, no responsibility for errors or omissions is accepted. JMO and the publisher do not endorse or guarantee, directly or indirectly, the quality or efficacy of any product or service described the advertisements or other material that is commercial in nature in any issue. All advertising is expected to conform to ethical and medical standards. No responsibility is assumed by JMO or the publisher for any injury and/or damage to persons or property as a matter of products liability, negligence or otherwise, or from any use or operation of any methods, products, instructions, or ideas contained in the material herein. Because of rapid advances in the medical sciences, independent verification of diagnoses and drug dosages should be made.



---

# Table of contents

**Editorial** . . . . . **4**  
*R.J. Braun*

## Meeting highlights articles

**A simple mathematical model for collagen fibril organization in normal and keratoconic corneas** . . . . . **7**  
*Peter M. Pinsky, Yanhui Ma, Yunjae Hwang, Sally Hayes, Keith M. Meek*

**Multiscale modeling of ocular physiology** . . . . . **12**  
*Lorenzo Sala, Riccardo Sacco, Giovanna Guidobon*

**A proposed mechanism for tear film breakup: a molecular level view by employing in-silico approach** . . . . . **19**  
*Lukasz Cwiklik, Adela Melcrova, Philippe Daull, Jean-Sebastien Garrigue*

**Dynamics of fluorescent imaging in glob-driven breakup** . . . . . **24**  
*Lan Zhong, Richard J. Braun, P. Ewen King-Smith, Carolyn G. Begley*

## Original articles

**Racial differences in the correlations between structural parameters and ocular blood flow in healthy eyes** . . . . . **29**  
*Koosha Ramezani, Alon Harris, Brent Siesky, Carine Olinde, Darrell WuDunn, Jennifer Eikenberry, Fang-I Chu, Leslie A. Tobe, Betül Kaskan, Lyne Racette*

**Using mathematics to avoid blindness in diabetics** . . . . . **42**  
*Arieh Helfgott, Ariella ER Helfgott, Sean Mullany*

**Condensation on intraocular lenses during vitrectomy: effect of perfluorocarbon liquids** . . . . . **71**  
*Yann J. Dacquay, Joseph R. Lee, Andrea Govetto, Matthias Elgeti, Wayne L Hubbell, Pirouz Kavehpour, Jean-Pierre Hubschman*



---

# ARVO 2017 highlights in mathematical modeling

R.J. Braun<sup>1</sup>

<sup>1</sup>Department of Mathematical Sciences, University of Delaware, Newark, DE, USA

**Keywords:** cornea, dry eye, lipid layer, mathematical modeling, tear film

At the ARVO annual meeting, the contributions that involve significant mathematical modeling of ocular physiology and procedures is on the increase. There has long been significant use of statistical methods for understanding data from a variety of uses such as *in-vivo* measurements and human trials of various sorts. Beyond those important uses of statistical and mathematical tools, a growing number of researchers are developing mathematical and computational models, often based on fluid and solid mechanics principles, that provide insights into ocular phenomena. A number of areas had noticeable contributions involving applications of models, such as tear production, tear film dynamics, corneal biomechanics, retinal blood flow, and glaucoma. We list a number of such contributions in this introduction, and five extended abstracts summarize some of the studies mentioned here.

Corneal biomechanics was an active area. The contribution from Francis and coworkers<sup>1</sup> sought to quantify the effect on the changes to corneal biomechanics due to incisions and subsequent healing from SMILE and FS-LASIK procedures using finite element modeling in an inverse problem approach. A contribution from Mengchen Xu and coworkers<sup>2</sup> sought to estimate collagen fibril properties using an inverse problem approach. Seven and coworkers<sup>3</sup> used a finite element method to study outcomes of post-PRK corneal tomographies. In this issue, there is an extended abstract from Pinsky and coworkers<sup>4</sup> that develops a simple yet effective continuum model for the collagen fiber arrangement in the stroma. The model fits wide angle x-ray scattering data from both normal and keratoconic human corneas. The model does a good job of capturing orientation dependence, and is suitable for use in finite element modeling the cornea. The model could enable significant insights into keratoconus, among other corneal phenomena.

Contributions using fluid mechanics approaches included models from the retina to the ocular surface. There were a number of papers studying mathematical

---

**Correspondence:** R.J. Braun, Department of Mathematical Sciences, University of Delaware, Newark, DE, USA.  
E-mail: rjbraun@udel.edu

---

blood flow in the retina related to glaucoma and other pathologies. These include two efforts<sup>5</sup> described in this issue. Sacco and coworkers<sup>5</sup> studied the effect of nitric oxide on the neurovascular coupling to regulate blood flow in the retina using a compartment model. Sala and coworkers<sup>6</sup> investigated a mathematical model of the blood flow in the lamina cribosa and retina that combined porous medium and compartment models that can be tailored to specific patients. An extended abstract in this issue briefly discusses results from these two projects. Another patient-specific modeling approach was presented by Krishnan *et al.*<sup>7</sup> that used finite element methods to compute mechanical response of the optic nerve head to, *e.g.*, various values of intraocular pressure. Incorporating realistic properties into such models was the focus of the study of Grytz *et al.*<sup>8</sup>

Moving forward into the posterior chamber, Repetto and coworkers<sup>9</sup> presented results on finite element models for the stresses generated on the retina as vitreous fluid detached from the posterior side. The work identified shapes of vitreous detachment that could generate large tractions on the retina.

At the ocular surface, the tear supply was of interest. Radke *et al.*<sup>10</sup> developed a relatively simple ordinary differential equation model that recovered experimentally observed profiles for tear production in Schirmer strips. This model clarifies interpretation of the different kinds of cases observed.

Two contributions studying tear film flow are included in this issue. One is a mathematical model for imaging using fluorescein in rapid tear break up (TBU) from Lan Zhong *et al.*<sup>11</sup> The model hypothesized that globs of excess lipid can drive strong tangential tear film flows that promote very rapid TBU. Their fluid dynamics model simplifies glob-driven flow and fluorescence from instilled dye to just a few partial differential equations that match observed time and space scales from *in-vivo* experiments. They find that unlike evaporatively-driven TBU, fluorescein concentrations below the critical value were better for estimating tear film thickness for rapid TBU that takes only a second or less. Another tear film contribution is from Cwiklik and co-workers.<sup>12</sup> In their approach, molecular dynamics is used on the various lipid molecules of a model lipid layer atop an aqueous layer. The lipid layer includes both non-polar and polar lipid molecules so that spreading of the lipid can occur, while some aspects of the molecules, such as the hydrocarbon tails, are simplified. They found that there could be small gaps in the spreading of the lipid layer, which could promote evaporation and TBU. This work is among the very few efforts that examines the molecular arrangement of the lipid layer itself. The approach is promising for improving our understanding of lipid layer structure, and could help lead to better treatments for dry eye and other ocular surface issues.

We hope that you enjoy the extended abstracts here as much as we enjoyed learning about these and other results at ARVO 2017.

## Acknowledgements

This work was supported by US National Science Foundation (NSF) Grant 1412085 and National Institutes of Health (NIH) Grant 1R01EY021794, and does not necessarily represent the official views of the NSF or NIH.

## References

1. Francis M, Pahuja N, Shetty R, Devanapalli K, Roy AS. A novel inverse finite element approach to analyze corneal deformation after SMILE and LASIK. ARVO Annual Meeting. Baltimore, MD, 2017; Abstract 4317–A0118.
2. Xu M, Funkenbush DP, Lerner AL, Yoon G. Estimating the material properties of collagen fibril using optical behavior of the human cornea. ARVO Annual Meeting. Baltimore, MD, 2017; Abstract 4332–A0133.
3. Seven I, Stefano VSD, Hardy D, Dupps WJ. Patient-specific computational analysis of photorefractive keratectomy: a clinical validation study. ARVO Annual Meeting. Baltimore, MD, 2017; Abstract 4320–A0121.
4. Pinsky P, Ma Y, Hwang Y, Hayes S, Meek K. A simple mathematical model for the collagen architecture of normal and keratoconic human corneas. ARVO Annual Meeting. Baltimore, MD, 2017; Abstract 4312–A0113.
5. Sacco R, Mauri AG, Cardani A, et al. Increased levels of nitric oxide may pathologically affect functional hyperemia in the retina: model and simulation. ARVO Annual Meeting. Baltimore, MD, 2017; Abstract 214–B0245.
6. Sala L, Prada CP, Salerni F, et al. Patient-specific virtual simulator of tissue perfusion in the lamina cribrosa. ARVO Annual Meeting. Baltimore, MD, 2017; Abstract 727–B0474.
7. Krishnan K, Libertiaux V, Grytz R, Girkin CA. Eye-specific finite element modeling of human optic nerve head (ONH) biomechanics. ARVO Annual Meeting. Baltimore, MD, 2017; Abstract 2457.
8. Grytz R, Krishnan K, Libertiaux V, Girkin CA, Downs JCC. Incorporating realistic anisotropic and heterogeneous material properties into eye-specific multi-scale models of the human optic nerve head. ARVO Annual Meeting. Baltimore, MD, 2017; Abstract 2458.
9. Repetto R, Michele FD, Tatone A. A mathematical model of posterior vitreous detachment and generation of vitreoretinal tractions. ARVO Annual Meeting. Baltimore, MD, 2017; Abstract 1595.
10. Radke CJ, Kim YH, Li W, Lin MC. Schirmer strips provide reliable tear-production rates. ARVO Annual Meeting. Baltimore, MD, 2017; Abstract 478–A0403.
11. Zhong L, Braun RJ, King-Smith PE, Begley CG. Dynamics of fluorescent imaging in glob-driven breakup. ARVO Annual Meeting. Baltimore, MD, 2017; Abstract 2613–A0203.
12. Cwiklik L, Melcrova A, Daull P, Garrigue J-S. Tear film break-up: a molecular level view by employing in silico approach. ARVO Annual Meeting. Baltimore, MD, 2017; Abstract 4312–A0113.



# A simple mathematical model for collagen fibril organization in normal and keratoconic corneas

Peter M. Pinsky<sup>1</sup>, Yanhui Ma<sup>2</sup>, Yunjae Hwang<sup>1</sup>, Sally Hayes<sup>2</sup>, Keith M. Meek<sup>2</sup>

<sup>1</sup>*Department of Mechanical Engineering, Stanford University, Stanford, California, USA,*

<sup>2</sup>*School of Optometry and Vision Sciences, Cardiff University, Cardiff, UK*

**Key words:** anisotropy, collagen fibril organization, cornea, keratoconus, x-ray scattering

## 1. Background and purpose

Wide-angle x-ray scattering techniques have been used to provide quantitative information about the angular distribution and preferred orientation of collagen fibrils throughout the cornea Meek, Boote [1]. Using this technique, it has been shown that collagen fibrils in the human cornea exhibit a preferential alignment in the inferior-superior and nasal-temporal directions Aghamohammadzadeh et al. [2]. However, this arrangement is often seen to be absent or disturbed in cases of keratoconus Hayes et al. [3] and Meek et al. [4], a dystrophy in which the cornea becomes progressively thin and weak, resulting in the appearance of a cone-shaped cornea.

The elasticity of stromal tissue depends on the distribution of collagen fibrils throughout the cornea, and preferential fibril alignments imply that the tissue is mechanically anisotropic. Finite element models for corneal biomechanics can account for this mechanical anisotropy by employing a fibril angular orientation probability function based on x-ray scattering patterns Cheng et al. [5]. However, the scattering patterns are obtained only at a discrete set of collection points, whereas finite element models need a continuous representation over the cornea. To address this need, a mathematical modeling approach is proposed that converts the x-ray data at the collection points into a single continuous function over the cornea Ma et al. [6]. This representation of the x-ray data is necessary for finite element analysis, as well as valuable for quantitatively analyzing and comparing fibril organization in normal and keratoconic corneas.

---

**Correspondence:** Peter M. Pinsky, Department of Mechanical Engineering, Stanford University, Stanford, CA 94305-4040, USA.

E-mail: [pinsky@stanford.edu](mailto:pinsky@stanford.edu)

---

## 2. Methods

The modeling approach uses two fitting steps, both based on least squares. First, the x-ray scattering data at each collection point is modeled as a continuous function of the x-ray scan angle,  $\theta$ , using the following representation:

$$s_1(\theta; \mathbf{p}) = a_1 \cos^{n_1}(\theta - \beta_1) + a_2 \sin^{n_2}(\theta - \beta_2) + c, \quad (1)$$

where  $\mathbf{p} = \{a_1, a_2, \beta_1, \beta_2, c\}$  are five parameters determined from a non-linear least squares problem (trials indicated that  $n_1 = n_2 = 6$  in all cases). In this way, x-ray scattering patterns at each collection point are reduced to five parameter values. In the second fitting step, the five parameters at each collection point are given a continuous representation over the corneal unit disk using Zernike basis functions, such that:

$$s_2(r', \varphi; \theta) = \left( \sum_{i=1}^{p_{a_1}} \widehat{\kappa}_{a_1}^i Z_i(r', \varphi) \right) \cos^6 \left( \theta - \sum_{i=1}^{p_{\beta_1}} \widehat{\kappa}_{\beta_1}^i Z_i(r', \varphi) \right) \\ + \left( \sum_{i=1}^{p_{a_2}} \widehat{\kappa}_{a_2}^i Z_i(r', \varphi) \right) \sin^6 \left( \theta - \sum_{i=1}^{p_{\beta_2}} \widehat{\kappa}_{\beta_2}^i Z_i(r', \varphi) \right) + \sum_{i=1}^{p_c} \widehat{\kappa}_c^i Z_i(r', \varphi), \quad (2)$$

where  $(r', \varphi)$  are polar coordinates on the unit disk and the five summations are expansions for the five parameters in  $\mathbf{p}$  using Zernike basis functions  $Z_i(r', \varphi)$ . The coefficients  $\widehat{\kappa}_p^i$ , for  $p \in \mathbf{p}$ , are obtained by solving a linear least squares problem. To prevent over-fitting and to maximize interpolation accuracy, multiple applications of ten-fold cross-validation Geisser [7] were used to establish the optimal radial order of the Zernike expansions in Equation (2).

## 3. Results

Data from four normal post-mortem corneas and four severe keratoconus corneal disks (removed during routine transplant surgery), were analyzed. X-ray scattering data were collected over the entire cornea in the case of the healthy samples and over a central 8 mm corneal disk in the case of the keratoconic samples. The accuracy of Equation (1) in reproducing the raw x-ray scattering plots for normal and keratoconic corneas at three typical collection points is illustrated in Figure 1. Fittings based on Equation (1) for both healthy and keratoconic corneas were obtained with high precision in all cases. In the second fitting step based, on Equation (2), ten-fold cross-validation studies determined that the maximum Zernike radial order is case-dependent; for normal corneas the optimal radial order was near 10, while for keratoconic corneas the optimal order was near 15. Figure 2 (row 1) illustrates the result of

the second fitting, showing the contours of the  $\beta_1$  and  $\beta_2$  coefficients (phase-shift of preferred orientations) for a normal and a keratoconic cornea. By integrating Equation (2) over  $\theta \in [0, 2\pi]$ , maps of total collagen mass and aligned collagen mass can be obtained. This is illustrated in Figure 2 (row 2), which contrasts mass contours for a normal and a keratoconic cornea.

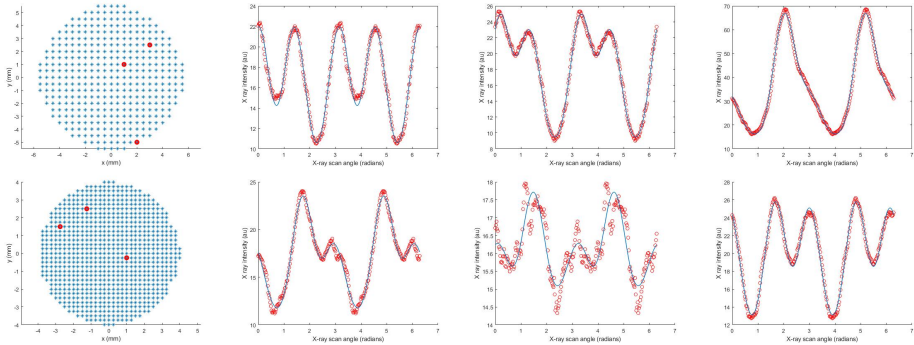


Fig. 1. Comparison of x-ray scattering data (red circles) and fitting by Equation (1) (blue curve). (Top row, left to right) Collection points and fit at three selected points for a healthy cornea. (Bottom row, left to right) Collection points and fit at three selected points for a keratoconic cornea.

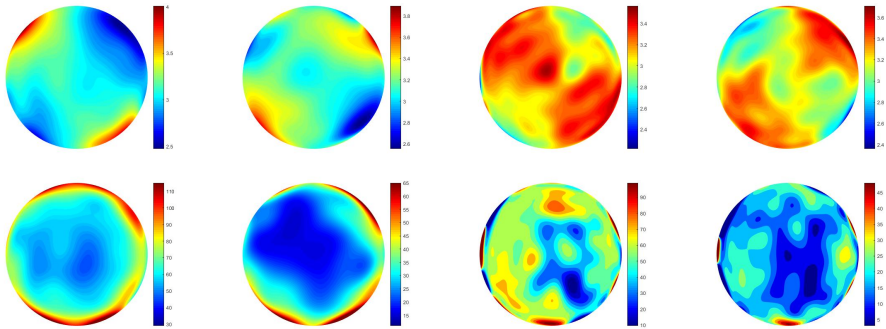


Fig. 2. Selected results from the second fitting based on Equation (2). (Top row, left to right) Contours of  $\beta_1$  and  $\beta_2$  for a normal cornea and for a keratoconic cornea. (Bottom row, left to right) Contours of predicted total collagen mass and aligned (anisotropic) collagen mass for a normal cornea and for a keratoconic cornea.

## 4. Conclusions and future perspectives

The proposed mathematical approach is based on two sequential fittings. The first fitting, based on the Fourier-type form given by Equation (1), proved to be accurate for every cornea analyzed. The Zernike expansion of the coefficients, expressed by Equation (2), also proved to have high predictive accuracy, but requires strict adherence to the optimal radial order as determined by the cross-validation studies.

Total and aligned collagen mass contours of the normal corneal pair have been previously published and agree with contours found from the model, providing a measure of the overall accuracy of the model. While keratoconic corneas may appear to exhibit great irregularity in collagen angular orientation, it is significant that Equation (1) models the x-ray data of both healthy and keratoconic corneas with high precision, suggesting that keratoconic collagen organization, even in severe cases, may result from a redistribution of the normal arrangement, possibly by lamellar slippage Meek *et al.* [4]. This conclusion is further reinforced by considering, for example, the contours of  $\beta_1$  and  $\beta_2$  shown in Figure 2. The normal cornea shows values that agree with preferred orientations in the inferior-superior and nasal-temporal directions; likewise, the keratoconic cornea has an essentially similar pattern except that it has become profoundly diffuse.

All completed tests have confirmed that the proposed modeling approach can accurately describe collagen organization in normal and keratoconic corneas. Next steps include implementation in a finite element analysis code and further geometric analysis to map the model onto the corneal sphere in order to reveal an improved interpretation of collagen organization.

## Acknowledgements

This work has been supported by a Medical Research Council UK Programme Grant MR/K000837/1 awarded to Keith M. Meek. We thank Diamond Light Source (UK) for access to beamline IO2 for the collection of x-ray scattering data, Mr. Stephen Tuft for the provision of keratoconus corneas, and the UK National Health Service Blood and Transplant for the provision of healthy donor corneas. A travel grant awarded to Yanhui Ma from the PGR International Experience Fund, Cardiff University (UK), is acknowledged.

## References

1. Meek K, Boote C. The use of X-ray scattering techniques to quantify the orientation and distribution of collagen in the corneal stroma. *Prog Retin Eye Res.* 2009;28(5): 369–392.
2. Aghamohammadzadeh H, Newton R, Meek K. X-ray scattering used to map the preferred collagen orientation in the human cornea and limbus. *Prog Retin Eye Res.* 2004;12(2): 249–256.
3. Hayes S, Boote C, Tuft S, Quantock A, Meek K. A study of corneal thickness, shape and collagen organisation in keratoconus using videokeratography and X-ray scattering techniques. *Exp Eye Res.* 2007;84(3): 423–434.

4. Meek K, Tuft S, Huang Y, Gill P, Hayes S, Newton R. Changes in collagen orientation and distribution in keratoconus corneas. *Invest Ophthalmol Vis Sci.* 2005;46(6): 1948–1956.
5. Cheng X, Petsche S, Pinsky P. A structural model for the in vivo human cornea including collagen-swelling interaction. *JR Soc Interface.* 2015;12(109): doi: 10.1098/rsif.2015.0241.
6. Ma Y, Hwang Y, Hayes S, Meek K, Pinsky P. A simple mathematical model for collagen fibril organization in normal and keratoconic corneas. *Proceedings, ARVO Annual Meeting, Baltimore, MD, 2017.*
7. Geisser S. *Predictive inference.* Chapman and Hall, 1993.



# Multiscale modeling of ocular physiology

Lorenzo Sala<sup>1</sup>, Riccardo Sacco<sup>2</sup>, Giovanna Guidoboni<sup>3</sup>

<sup>1</sup>*Institute for Advanced Mathematical Research, UMR 7501, National Center for Scientific Research, University of Strasbourg, Strasbourg, France,* <sup>2</sup>*Department of Mathematics, Politecnico di Milano (Polytechnic University of Milan), Milan, Italy,* <sup>3</sup>*Department of Electrical Engineering and Computer Science, University of Missouri, Columbia, MO, USA*

**Key words:** multiscale mathematical modeling, neurovascular coupling, ocular blood flow, optic nerve head perfusion

## 1. Background and purpose

Our purpose is to devise mathematical models that can serve as synergistic complements to experimental and clinical studies and deepen the current knowledge of ocular physiology in health and disease. One of the main challenges in developing a mathematical description of ocular physiology stems from the inherent multiscale nature of life in time and space. For example, the time scales of cellular biochemical reactions, cardiac cycle, circadian rhythm, and aging differ by several orders of magnitude, and yet they all matter when studying diseases such as glaucoma. Similarly, the length scales of ion channels, cells, tissues, and organs span from nanometers to centimeters, and yet they all interact to determine our bodily functions.

In this article, we highlight two recent contributions towards the multiscale modeling of ocular physiology that our group presented at the 2017 Annual Meeting of the Association for Research in Vision and Ophthalmology (ARVO, 7-11 May, 2017, Baltimore, MD, USA). The first contribution presents a Mathematical Virtual Simulator (MVS), henceforth indicated as *model M1*, to simulate the biomechanics and the tissue perfusion of the lamina cribrosa (LC).<sup>1</sup> Model M1 may serve as a computational tool to visualize hemodynamic and biomechanic parameters in the LC, such as LC displacement, blood flow velocity and pressure, and predict their spatial and temporal variability. The aim of model M1 is to leverage partial data available on some parts of the eye (e.g., blood velocity in the central retinal vessels and ocular geometry) to provide

---

**Correspondence:** Université de Strasbourg, CNRS, IRMA UMR 7501, 7 rue René-Descartes, 67084 Strasbourg Cedex, France.

E-mail: sala@unistra.fr

---

further information on other parts of the eye that are very important from a clinical viewpoint, but that may not be easily accessible with standard research instruments.

The second contribution presents a mathematical model, henceforth indicated as *model M2*, to theoretically investigate the role of neural nitric oxide (nNO), jointly with 20-hydroxyeicosatetraenoic acid (20-HETE) and epoxyeicosatrienoic acid (EET), in the regulation of retinal neurovascular coupling.<sup>2</sup> The analysis is motivated by experimental data of flicker light-induced functional hyperemia (FH) in humans, indicating that increased nitric oxide levels mediated by 20-HETE reduce vasodilation.<sup>3</sup> The aim of model M2 is to provide quantitative predictions of the effect of increased levels of nNO on the vasodilation of retinal arterioles to theoretically investigate the conjecture that increased nitric oxide levels may be responsible for suppressing flicker-evoked vasodilation in diabetic retinopathy.<sup>3</sup>

## 2. Methods

In both models, M1 and M2, a deterministic multiscale approach is adopted, in which equations are derived by general physical principles, such as balance of mass and linear momentum. In addition, both models are designed so that their input data include quantities that can be determined in a clinical setting, such as systolic and diastolic blood pressure (SBP and DBP), intraocular pressure (IOP), and ocular geometry.

Model M1 employs a system of partial differential equations to provide a detailed spatial and temporal characterization of the physical variables within the LC, combining a 3-D porous-media model for LC perfusion with a circuit-based model for blood flow in the retrobulbar and ocular posterior segments (Fig. 1). The whole coupled system is solved using advanced computational and visualization methods.<sup>4</sup>

Model M2 employs a system of ordinary differential equations to provide a systemic view of retinal hemodynamics, combining an equivalent electrical circuit of resistive and capacitive compartments for the retinal vasculature (Fig. 2b) with a cellular scale chemomechanical description of neurovascular coupling as the resulting interaction between vasoactive agents synthesized by active neurons, astrocytes, and smooth muscle cell contraction/dilation (Fig. 2a). Kirchhoff current law is solved at each node of the equivalent electrical circuit to determine the time evolution of nodal blood pressures and compartment diameters.<sup>5</sup>

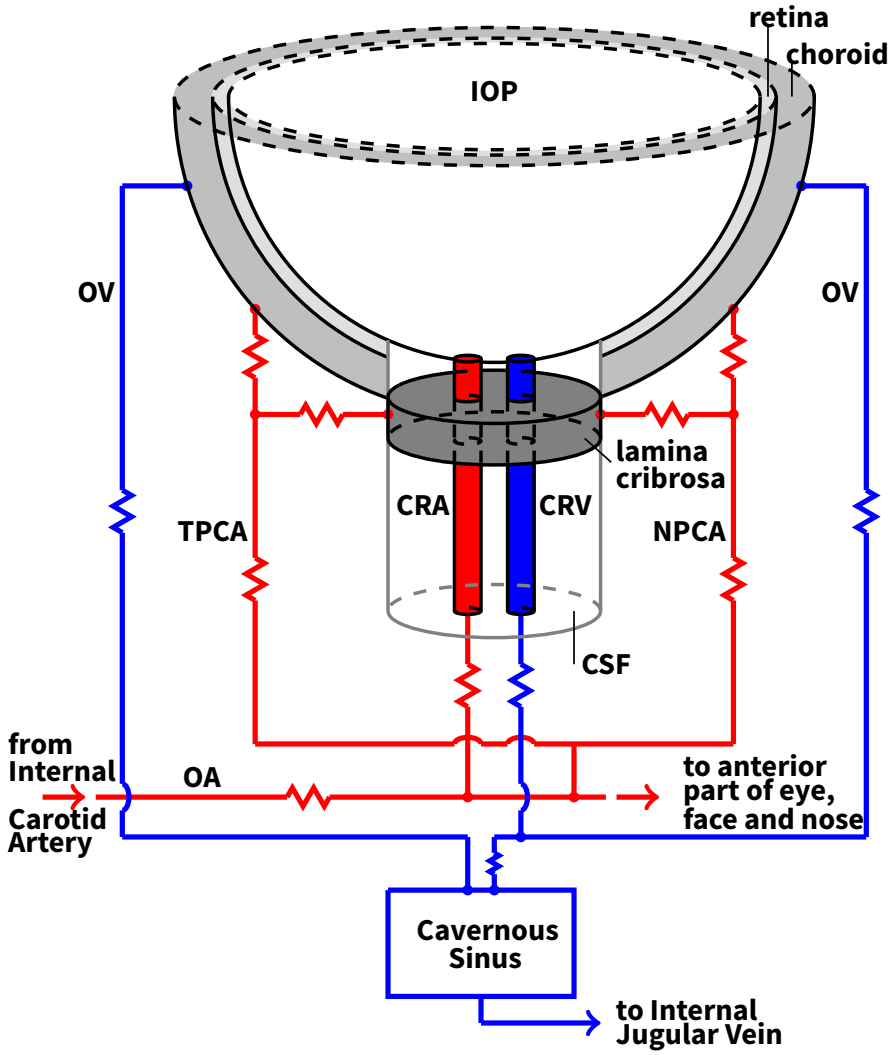


Fig. 1. MVS multiscale scheme. Schematic representation of the ocular blood supply.

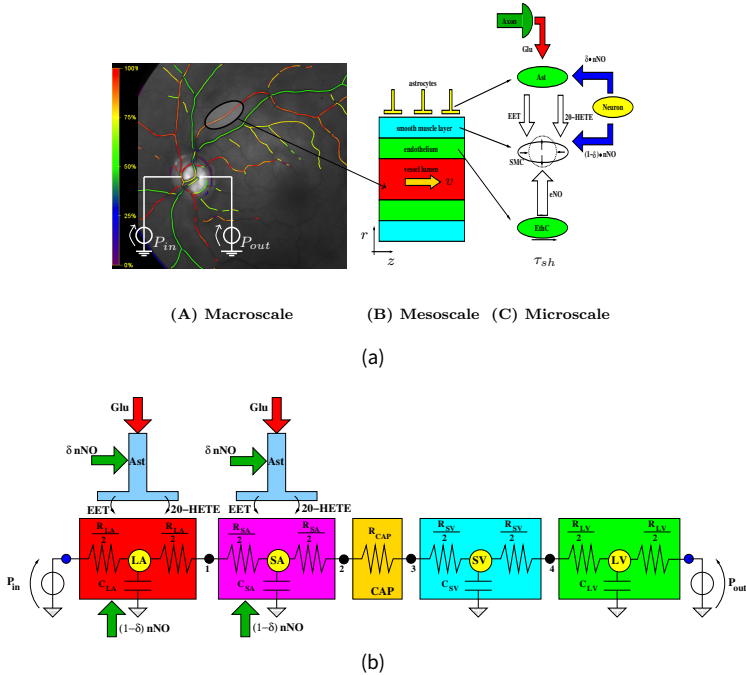


Fig. 2. (a) Multiscale description of neurovascular coupling in the retina. The model inputs at the *Macroscale* (A) are the blood pressures at the inlet and outlet of the retinal circulation,  $P_{in}$  and  $P_{out}$ . The *Mesoscale* (B) focuses on arterioles, whose walls comprise endothelium and smooth muscle cells. The *Microscale* (C) entails the biochemistry at the cellular level that governs the change in smooth muscle shape. (b) *Macroscale*, *Mesoscale*, and *Microscale* are effectively combined in a single model by means of appropriate equivalent resistances.

### 3. Results

Figure 3a reports the M1 visualization of ocular geometry. Simulations performed using the MVS show that:

1. LC displacement (Fig. 3f) is not highly influenced by the presence of the central retinal artery (CRA)/central retinal vein (CRV) opening,<sup>6</sup> and the values are comparable to those reported in experimental studies;<sup>7</sup>
2. LC blood pressure distribution (Fig. 3d) is highly influenced by the values of SBP/DBP imposed at the inlet of the circuit model and attains realistic values,<sup>8</sup> in particular on the lateral boundary;
3. LC perfusion (Fig. 3b) increases with SBP/DBP, particularly near the nasal area; and
4. CRA and CRV blood velocities (Figs. 3c and 3e, respectively) are comparable to

those obtained via direct imaging modalities.<sup>9</sup>

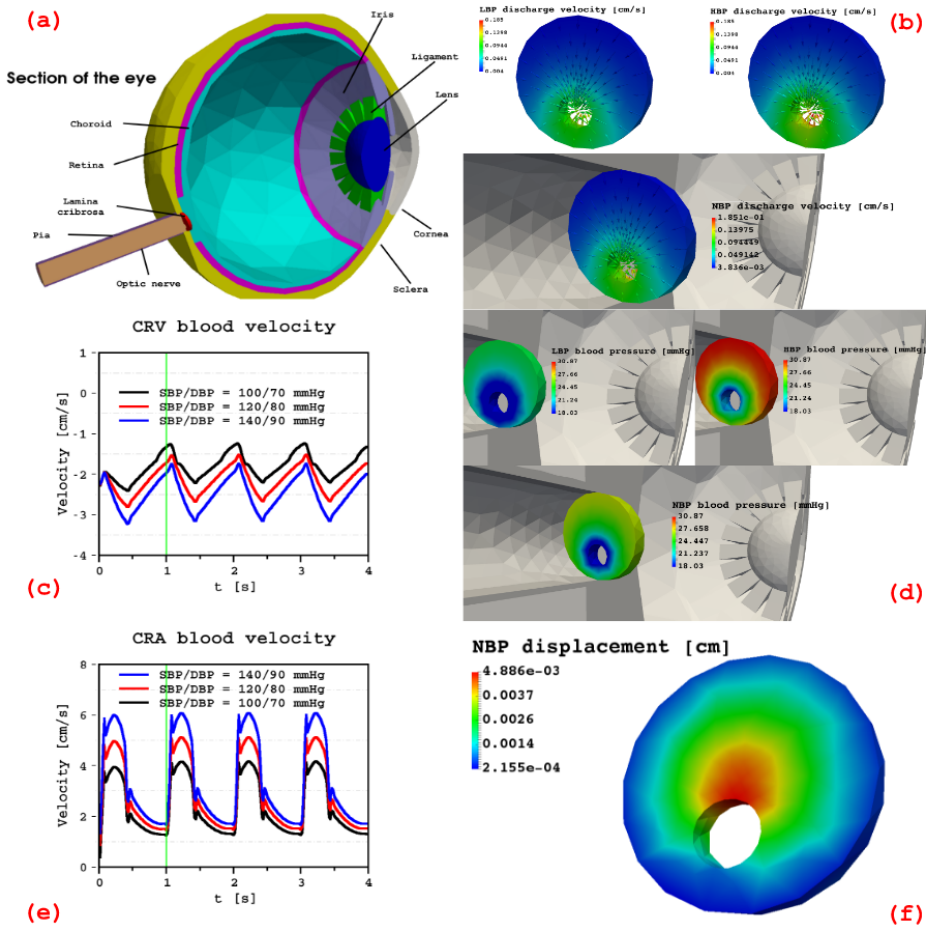


Fig. 3. LC perfusion simulated using the MVS in the case of low, normal, and high blood pressure, denoted by LBP, NBP, and HBP, respectively. (a) Digitalized geometry of the eye. (b) Simulated discharge velocity. (c) Simulated blood velocity in the CRV. (d) Simulated pressure distribution. (e) Simulated blood velocity in the CRA. (f) Simulated LC displacement. Only NBP displacement is shown because simulations in LBP and HBP conditions yield similar results.

Figure 4 shows the results of model M2 in the simulation of FH in humans under flicker light stimulation (FLS).<sup>3</sup> In the top and central panels, FLS is modeled by a triangular glutamate (GLU) input signal of  $0.07 \mu\text{M}$  for 20 seconds. Simulations are performed for two different nNO levels (baseline value: nNO<sub>b</sub>, black line; increased value: nNO<sup>+</sup> > nNO<sub>b</sub>, red line). In the bottom left panel, FH in humans is simulated with the triangular GLU signal, nNO = nNO<sub>b</sub>, and different neurovascularly active (NVA) segments.

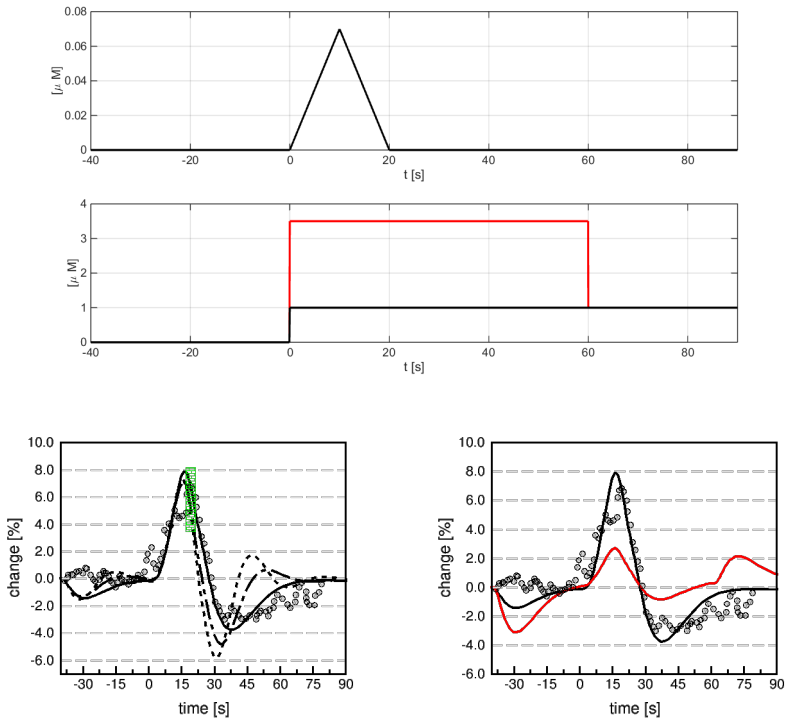


Fig. 4. Neurovascular coupling simulations. (Top) Glutamate stimulus. (Center) Baseline (black) and elevated (red) levels of nNO. (Bottom left) Simulated % change in MAD. Black circles: experimental data in Newman;<sup>3</sup> green rectangle: data variation at the end of the GLU stimulus; dashed line: only one LA is NVA; dash-dotted line: network where only LA are NVA; solid black line: network where both LA and SA are NVA. (Bottom right) Simulated % change in MAD. Black circles: experimental data in Newman;<sup>3</sup> solid black line: network where both LA and SA are NVA,  $nNO = nNO^0$ ; red black line: network where both LA and SA are NVA,  $nNO = nNO^+$ .

The y-axis is the % change in mean arterial diameter (MAD). Black circles indicate the experimental data in Newman;<sup>3</sup> the green rectangle highlights data variation at the end of the GLU stimulus; the dashed line shows the model prediction using only one large arteriole (LA); the dash-dotted line is the model prediction using the network in Figure 2b, where only LA are assumed to be NVA; the solid black line shows the model prediction using the network in Figure 2b, where both LA and small arterioles (SA) are assumed to be NVA. Results indicate that FH is correctly represented only if both LA and SA are assumed to be NVA. In the bottom right panel, we illustrate the simulated effect on vasodilation due to the GLU signal and a 60 s stimulus of  $nNO = nNO^+$ . Results indicate that elevated nNO may reduce vasodilation by a factor of 4.



# A proposed mechanism for tear film breakup: a molecular level view by employing *in-silico* approach

Lukasz Cwiklik<sup>1</sup>, Adela Melcrova<sup>1</sup>, Philippe Daul<sup>2</sup>, Jean-Sebastien Garrigue<sup>2</sup>

<sup>1</sup>J. Heyrovsky Institute of Physical Chemistry, Czech Academy of Sciences, Prague, Czech Republic; <sup>2</sup>Novagali Innovation Center, Santen SAS, Evry, France

**Keywords:** dry eye disease, molecular dynamics, molecular simulations, tear film, tear film lipid layer

## 1. Background and purpose

Upon eyelid opening after a blink, tear film (TF) is in a non-equilibrium state and undergoes a complex structural evolution.<sup>1</sup> In the final stages of this development, the film loses its continuity, which results in so called tear film breakup (TFBU). This phenomenon is critical because it leads to deterioration of the protective role of TF. Importantly, in dry eye disease (DED) the TFBU time is typically shortened according to different patterns, demonstrating that the disease is related to reduced TF stability.<sup>2,3</sup> The aqueous tear layer at the corneal surface is stabilized by the presence of a relatively thin layer of lipids at the water-air interface, the so-called tear film lipid layer (TFLL).<sup>4</sup> It has been demonstrated that DED is accompanied by an alteration in TFLL composition, and that TFBU time depends on the properties of TFLL.

Even though TF deterioration and breakup are of key importance for understanding DED, neither the breakup mechanism nor the role played by lipids are understood at a very basic level; such an understanding is required for developing new DED treatments. For instance, it was observed that exogenous and relatively simple surfactant molecules, such as cetalkonium chloride (CKC), are able to stabilize TF in DED in mice and humans.<sup>5,6</sup> Hence, it would be beneficial to understand the role of natural lipids in TFLL as well as the interactions between its endo- and exogenous components. We hypothesize that various lipid classes of TFLL play

---

**Correspondence:** Lukasz Cwiklik, J. Heyrovsky Institute of Physical Chemistry CAS, Dolejskova 2155/3, 18223 Prague, Czech Republic  
E-mail: lukasz.cwiklik@jh-inst.cas.cz

---

specific roles both during the onset of TF breakup and in maintaining TF stability. We also postulate that, through specific interactions with TF lipids, CKC enhances film stability.<sup>7</sup> We focus on the behavior of TFLL models deficient in individual lipid components as mimics of DED tear film.

## 2. Methods

*In-silico* molecular dynamics (MD) simulations are unique in providing molecular-level information regarding organization and dynamics of thin films at interfaces. Here, we simulated lipid films at water-air interface employing a coarse grain MARTINI model.<sup>8</sup> Such an approach was proven to realistically model TF and TFLL in our earlier studies.<sup>9,10</sup> Lipid composition of TFLL was approximated by using main lipid classes found in human tears in lipidomics studies.<sup>11</sup> More specifically, 1-palmitoyl-2-oleoyl-phosphatidylcholine (POPC); 1-palmitoyl-2-oleoyl-phosphatidylethanolamine (POPE); N-palmitoyl-d-erythro-sphingosine (PPCE); and N-palmitoyl-d-erythro-sphingosylphosphorylcholine (PPCS) were used as polar lipids in the ratio found in the lipidome of human TF.<sup>11</sup> Non-polar lipids were represented by an equimolar mixture of glycerine trioleate (TO) and cholesteryl oleate (CO). Additionally, cations of CKC were incorporated in the lipid film in some of the simulated systems. Lipid films deficient in: polar, non-polar, or both polar and non-polar lipids were considered. The simulation box typically consisted of 6-25 thousand lipids with 90-350 thousand water beads. Lateral sizes between 25 x 25 nm<sup>2</sup> and 34 x 34 nm<sup>2</sup> were considered. MD trajectories of ~2 μs length were simulated both under equilibrium and non-equilibrium conditions. In the former case, a lipid film completely covering the water surface was equilibrated at the water-air interface and its properties were analyzed. In the non-equilibrium case, initial system configurations were generated from the previous equilibrium simulations by removing half of the already equilibrated lipid film in such a way that the remaining lipids formed a small patch of rectangular shape at the water surface. The resulting MD simulations were hence probing a non-equilibrium process of wetting the water surface by the TFLL.

## 3. Results

We evaluated three main models of TF. First, we considered TF with “non-deficient” TFLL, consisting of such an amount of polar and non-polar lipids that a full lipid film was formed at the water-air interface. In this system, polar lipids resided in a monolayer form with 0.67 nm<sup>2</sup> area per lipid, while non-polar lipids formed a multilayer cover atop the polar monolayer. Such a system may be considered a model of relaxed TF, as described in our previous study.<sup>9</sup> Second, we simulated the

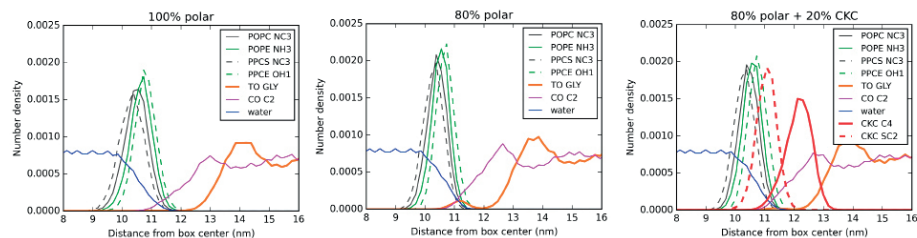


Fig 1. Density profiles calculated for the system with full content of polar lipids (*left*), the system with 80% of polar lipids (*middle*), and the system with 80% of polar lipids supplemented with CKC (*right*). The area under each number density is normalized to unity. The density of the choline (POPC, PPCS), amine (POPE), and hydroxyl groups (PPCE) is shown. In TO, the glycerol group is depicted, and the terminus of C20-C27 side chain is shown for CO. In CKC, the terminus of the non-polar chain (C4), as well as the charged headgroup (SC2), are presented.

system with only 80% polar lipids with regard to the previous model. This can be regarded as polar lipid-deficient TF. Third, the system with 80% polar lipids was enriched in 20% (with regard of the initial polar lipid content) of CKC molecules. This model can be viewed as polar lipid-deficient TF supplemented with CKC-containing emulsions. In Figure 1, density profiles corresponding to the three simulated systems are presented. These results were collected in equilibrium MD simulations, *i.e.*, with the lipid film equilibrated at the water-air interface.

In all three models, polar lipids reside at the water-air interface, with their polar groups in contact with water. Hence, polar lipids attain a monolayer-like arrangement. Regarding non-polar lipids, they are spread atop of the polar layer, but their detailed arrangement varies. Namely, in “non-deficient” TFL, TO molecules penetrate much closer toward polar lipids than the molecules of CO, as evidenced from the partially overlapping density profiles of TO and polar lipids. A further inspection of MD trajectories reveals that there is significant overlap and interdigitation between tails of CO and tails of polar lipids. At the same time, TO molecules do not overlap with the polar layer and are effectively separated from polar lipids by CO.

In the case of the polar lipids-deficient system, a minor peak at the density profile of TO appears in the region occupied by polar lipids (~11.2 nm). It indicates that the shortage of polar lipids leads to involvement of some TO molecules in direct contact with their polar counterparts. Inspection of the trajectories show that there are multiple pores formed in the polar monolayer occupied by TO lipids, and hence, contributing to the observed TO-water contacts. Interestingly, when the system is supplemented with CKC, which incorporates in-between polar lipids, the small peak at the TO density profiles virtually disappears. Hence, the presence of CKC leads to diminished TO-polar lipids contact, even in the case of polar lipids deficiency.

In Figure 2, the results of TFL spreading simulated at the water-air interface are

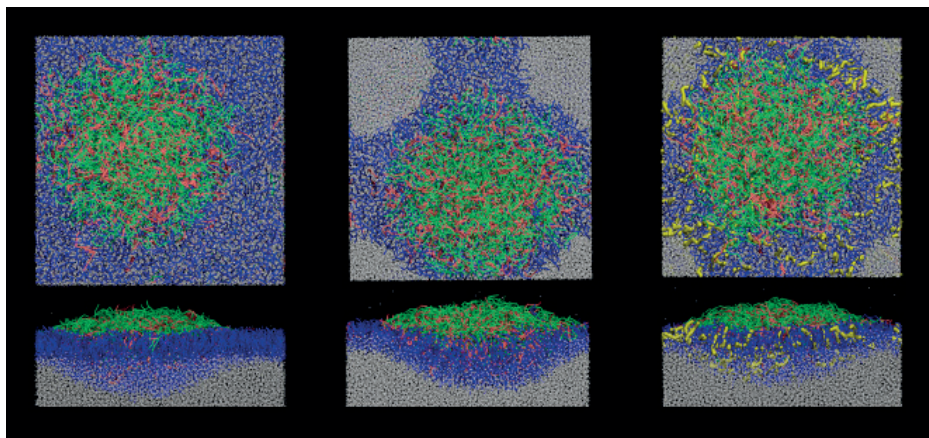


*Fig. 2.* Representative snapshots of the simulated systems recorded in the final stages of TFLL spreading at the water-air interface in non-equilibrium MD simulations upon equilibration in the non-equilibrium simulations. The system with full content of polar lipids (*left*), the system with 80% of polar lipids (*middle*), and the system with 80% of polar lipids supplemented with CKC (*right*) are shown. The first row depicts a view from the gas phase (top view) and the second row presents a cross-section through the middle of the lipid patch (side view). Water is shown in gray, polar lipids in blue, TO in green, CO in brown, CKC in yellow.

presented. In the case of “non-deficient” TFLL, part of the interface is covered by a lipid lens-like multilayer structure resembling the relaxed TFLL, as obtained in our equilibrium cases. At the same time, some of the polar lipids spread homogeneously at the rest of the interface, forming an expanded monolayer. In the case of polar lipids-deficient system, the lens-like multilayer structure is also present. However, the reduced overall amount of polar lipids allows for only partial covering of the interface. Interestingly, the polar lipids are concentrated close to the lens-like structure, not forming an expanded monolayer. In the system supplemented with CKC, the covering of the interface by polar lipids increases, so that CKC effectively promotes spreading of polar lipids in otherwise polar-lipid deficient TFLL.

#### 4. Conclusions and future perspectives

The coarse grain MD simulations of the considered TF mimics indicate that when polar lipids are diminished in TFLL, the polar monolayer undergoes poration, leading to enhanced contacts between non-polar triglycerides and water. It can be presumed that, due to unfavorable nature of such non-polar-polar interactions, the lipid film becomes less stable, which can then lead to film breakup. Reduction of polar lipid content also results in less efficient spreading of the lipid film at the water-air interface. The effects of both the unfavorable water-lipids interactions

and reduced film spreading can be prevented to some extent by the presence of CKC cations. These findings open new perspectives for understanding both TF breakup and spreading mechanisms at the molecular level, as well as for finding new surfactant molecules able to help stabilize TF.

## Acknowledgements

This work was supported by Grant 15-14292S from the Czech Science Foundation. Lukasz Cwiklik and Adela Melcrova have a commercial relationship with Santen SAS (Evry, France).

## References

1. Braun RJ. Dynamics of the tear film. *Annu Rev Fluid Mech.* 2012;44:267-297.
2. King-Smith PE, Bailey MD, Braun RJ. Four characteristics and a model of an effective tear film lipid layer (TFLL). *Ocul Surf.* 2013;11:236-245.
3. Yokoi N, Georgiev GA, Kato H, et al. Classification of fluorescein breakup patterns: a novel method of differential diagnosis for dry eye. *Am J Ophthalmol.* 2017; 180,72-85.
4. Cwiklik L. Tear film lipid layer: A molecular level view. *Biochim Biophys Acta-Biomembranes.* 2016;10:2421-2430.
5. Quentric Y, Daull P, Feraille L, Elena P-P, Garrigue J-S. Efficacy of a preservative-free cationic emulsion vehicle eye drop in a mouse model of dry eye. *Invest Ophthalmol Vis Sci.* 2016;57:422.
6. Amrane M, Cruzot-Garcher C, Robert P-Y, et al. Ocular tolerability and efficacy of a cationic emulsion in patients with mild to moderate dry eye disease—A randomised comparative study. *J Fr Ophtalmol.* 2014;37:589-598.
7. Cwiklik L, Melcrova A, Daull P, Garrigue J-S. Tear film break-up: a molecular level view by employing in silico approach. *Invest Ophthalmol Vis Sci.* 2017;58:472.
8. Marrink SJ, Risselada HJ, Yefimov S, Tieleman DP, de Vries AH. The MARTINI force field: coarse grained model for biomolecular simulations. *J Phys Chem B.* 2007;111:7812-7824.
9. Wizert A, Iskander DR, Cwiklik L. Organization of lipids in the tear film: a molecular-level view. *Plos One.* 2014;9,e92461.
10. Olżyńska A, Cwiklik L. Behavior of sphingomyelin and ceramide in a tear film lipid layer model. *Ann Anat.* 2017;210:128-134.
11. Rantamaki AH, Seppanen-Laakso T, Oresic M, Jauhiainen M, Holopainen JM. Human tear fluid lipidome: from composition to function. *PLoS One.* 2011;6:e19553.



# Dynamics of fluorescent imaging in glob-driven breakup

Lan Zhong<sup>1</sup>, Richard J. Braun<sup>1</sup>, P. Ewen King-Smith<sup>2</sup>, Carolyn G. Begley<sup>3</sup>

<sup>1</sup>Department of Mathematical Sciences, University of Delaware, Newark, DE, USA,

<sup>2</sup>College of Optometry, The Ohio State University, Columbus, OH, USA, <sup>3</sup>School of Optometry, Indiana University, Bloomington, IN, USA

*Key words:* dry eye, fluorescence imaging, tangential flow, tear film breakup

## 1. Background and purpose

Fluorescent imaging has been widely used when imaging tear breakup (TBU) and diagnosing dry eye. However, the accuracy of using fluorescein images to quantify TBU is still an active area of research. Mathematical models have studied different mechanisms of tear film (TF) dynamics and dry eye.<sup>1</sup> Recent findings from mathematical models simulating evaporative TBU indicate that TF fluorescein concentrations higher than approximately 0.2% work well when visualizing TBU.<sup>2</sup>

In this work, we are more interested in imaging TBU caused by another mechanism: tangential flow. Our experimental results suggest that tangential flow can be responsible for rapid thinning, where TBU occurs in under a second. The tangential flow can be driven by a glob in the lipid layer; the glob is hypothesized to have more lipid than the surrounding area, which can cause Marangoni flow that rapidly thins the tear film and may cause TBU.<sup>3</sup> Due to a much shorter time scale and a different mechanism for rapid thinning, we expect the dynamics of fluorescein in the tears to be different. By building mathematical models which simulate the strong tangential flow, we studied solute movement inside the aqueous layer and its effects on fluorescent imaging. The results from the mathematical models suggest that a dilute TF fluorescein concentration may be the best for approximating TF thickness in rapid TBU.

## 2. Methods

We developed partial differential equation (PDE) models which capture the important dynamics in rapid thinning. The models include evaporative ( $J$ ), tangential, and

---

**Correspondence:** L. Zhong, 501 Ewing Hall, University of Delaware, Newark, DE 19719, USA.  
E-mail: lanzhong@udel.edu

---

osmotic flows. The evaporation is specified within experimental ranges based on the assumptions of the composition of globs. Tangential flow is driven by assuming that the surface tension at the glob is low; strong tangential flow is then induced by the Marangoni effect. Osmotic flow is assumed to be proportional to the osmolarity difference across the corneal surface. The TF is very thin, which allows us to use lubrication theory to non-dimensionalize the governing equations from fluid mechanics and reduce them to four PDEs.

The models are solved numerically in Matlab (MathWorks, Natick, MA, USA) using method of lines in time and Chebyshev spectral discretization in space. The resulting differential-algebraic equations are solved by ode15s in Matlab; this method is stable for the parameters we studied here. We solve the model for aqueous TF thickness ( $h$ ), pressure ( $p$ ), lipid concentration ( $\Gamma$ ), osmolarity ( $c$ ), and fluorescein concentration ( $f$ ). We initialize our model to be a uniformly flat TF with a single glob in the center; the glob has a higher  $\Gamma$  than the surrounding area. The evaluated  $h$  help us track the thinning process of the TF. With  $h$  and  $f$  from the models, we can calculate the fluorescein intensity, ( $I$ ).<sup>4</sup>  $I$  is the quantitative data usually measured directly for interpreting TF thickness in clinical settings. By comparing the computed  $I$  and  $h$  from our model, we estimate the accuracy to approximate  $h$  for rapid TBU.

### 3. Results

Within appropriate range of glob size ( $r_I$ ), TBU can happen in about a second or less. Our model successfully captured the short time scale in rapid TBU. Figure 1 shows that  $h$  thins to  $0.25 \mu\text{m}$  at  $0.57 \text{ s}$ , which is the threshold for TBU defined in our model. At the same time,  $\Gamma$  spreads to the region on the right, acting as a source that keeps driving the tangential flow. Due to the short time and our assumed evaporation profile (see Eq. 5 in the Appendix),  $c$  and  $f$  increased only slightly under the glob. We assume the evaporation rate is uniform. The concentration of solutes increases in percentage due to a thinner TF under the glob. Tangential flow does not change solute concentration in the aqueous layer. Comparing the first column with the last column, we see that  $I$  appears to be proportional to  $h$  when initial concentration  $f_0 = 0.2\%$ .

When using higher concentrations of fluorescein in rapid TBU, the proportionality between  $I$  and  $h$  is lost. Figure 2 shows results with  $f_0 = 0.8\%$ . Figure 3 summarizes results for various  $f_0$ . Here,  $a = 1/\sqrt{I_0}$  is the constant that normalizes  $I$  to unity for  $h = 1$  at  $t = 0$ .

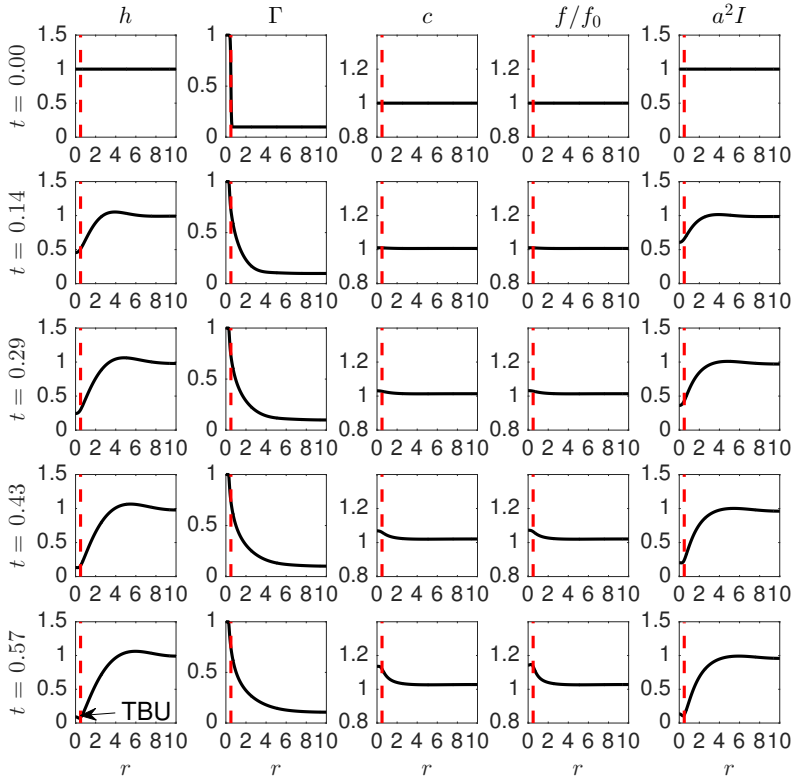


*Fig. 1.* Dynamics of the tear thinning. The vertical dashed line represents the edge of the glob. The dimensionless glob size in this figure is  $r_I = 0.5$  (0.037 mm), the domain size is 0.74 mm, and the initial fluorescein concentration is  $f_0 = 0.2\%$ .

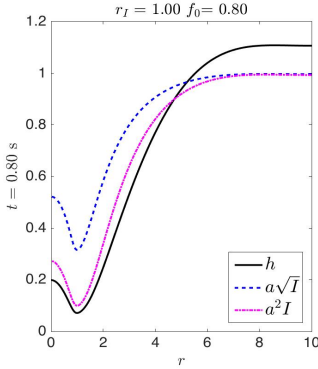


Fig. 2. TBU occurs in 0.80 s when  $r_I = 1$ . Fluorescein intensity does not accurately represent TF thickness when  $f_0 = 0.8\%$  for rapid TBU.

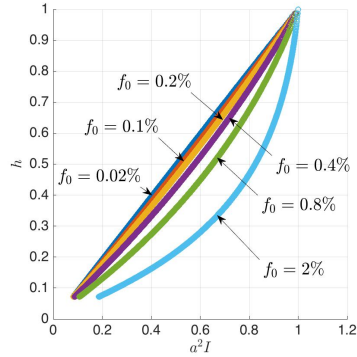


Fig. 3. Scatter plot of scaled fluorescein intensity and TF thickness with different  $f_0$ . When  $f_0$  is lower than 0.2%,  $a^2I$  can roughly linearly indicate tear thinning.

## 4. Conclusions and future perspectives

Rapid TBU as described here occurs in about a second or less.<sup>5,6</sup> Evaporation only slightly increases fluorescein concentration in such a short time. Our models suggest that initial fluorescein concentration at the critical value or less is recommended when imaging rapid TBU. Concentrations beginning at 0.2% or higher are appropriate for evaporative TBU.<sup>2,4,7</sup>

Another hypothesis regarding rapid TBU is that it is caused by dewetting of the corneal surface; we did not study this case here.<sup>5</sup> Further work that isolates dewetting as a cause of rapid TBU would be highly desirable. A more comprehensive version of this work will be submitted elsewhere. In future work, the models discussed here should be extended to more realistic glob shapes and mobile globs.

## Acknowledgements

This work was supported by US National Science Foundation (NSF) Grant 1412085 (Richard J. Braun), US National Institutes of Health (NIH) Grant R01EY17951 (P. Ewen King-Smith), and NIH Grant 1R01EY021794 (Carolyn G. Begley), and does not necessarily represent the official views of the NSF or NIH.

## Appendix

Dimensionless model for circular-shape glob-driven TBU in axisymmetric cylindrical coordinates:

$$\partial_t h = -J + P_c(c - 1) - \frac{1}{r} \partial_r (r h \bar{u}), \quad (1)$$

$$\partial_t \Gamma = \left[ \text{Pe}_\Gamma^{-1} \left( \frac{1}{r} \partial_r (r \partial_r \Gamma) \right) - \frac{1}{r} \partial_r (r \Gamma u_r) \right] B(r), \quad (2)$$

$$h \partial_t s = \text{Pe}_s^{-1} \frac{1}{r} \partial_r (r h \partial_r s) + J s - P_c (c - 1) s - h \bar{u} \partial_r s, \quad (3)$$

where  $s = c$  or  $f$ ,  $B(r)$  blends the glob and tear/air interfaces, and:

$$0 = p + \frac{1}{r} \partial_r (r \partial_r h) + A h^{-3}, \quad (4)$$

$$J = v \quad (5)$$

$$\bar{u} = \frac{-\frac{1}{3} \partial_r p h^2 [B(r) + \frac{1}{4} h (1 - B(r))] - \frac{1}{2} h B(r) \partial_r \Gamma}{B(r) + (1 - B(r)) h}, \quad (6)$$

$$u_r(r, h, t) = \frac{-\frac{1}{2} \partial_r p h^2 B(r) - \partial_r \Gamma B(r) h}{B(r) + (1 - B(r)) h}, \quad (7)$$

$$B(r; r_I, r_W) = 0.5 + 0.5 \tanh \left( \frac{r - r_I}{r_W} \right). \quad (8)$$

The constants in the equations are non-dimensional forms for the following quantities:

1. the uniform evaporation rate,  $v = 9.75 \times 10^{-4}$  (dimensionally,  $10 \mu\text{m}/\text{min}$ );
2. the transition width for the blend function  $r_W = 0.05$ ;
3. the Hamaker constant for wetting,  $A = 2.86 \times 10^{-4}$ ;
4. the permeability of the corneal surface to water,  $P_c = 3.82 \times 10^{-10}$ ;
5. the Peclet number for solutes in the aqueous layer,  $\text{Pe}_c = 168$ ,  $\text{Pe}_f = 690$ ; and
6. the surface Peclet number for polar lipid,  $\text{Pe}_\Gamma = 8.97$ .

## References

1. Braun RJ. Dynamics of the tear film. *Ann Rev Fluid Mech.* 2012;44: 267–297.
2. Braun RJ, Driscoll TA, Begley CG, King-Smith PE, Siddique JI. On tear film breakup (TBU): dynamics and imaging. *Math Med Biol.* 2017. doi: 10.1093/imamb/dqw023.
3. King-Smith PE, Reuter KS, Braun RJ, Nichols JJ, Nichols KK. Tear film breakup and structure studied by simultaneous video recording of fluorescence and tear film lipid layer images. *Invest Ophthalmol Vis Sci.* 2013;54(7): 4900–4909.
4. Nichols JJ, King-Smith PE, Hinel EA, Thangavelu M, Nichols KK. The use of fluorescent quenching in studying the contribution of evaporation to tear thinning evaporation contribution to tear thinning. *Invest Ophthalmol Vis Sci.* 2012;53(9): 5426–5432.
5. Yokoi N, Georgiev GA. Tear-film-oriented diagnosis and therapy for dry eye. *Dry eye syndrome: basic and clinical perspectives.* London: Future Medicine Ltd, 2013; Chapter 7, p. 96–108.
6. Braun RJ, King-Smith PE, Begley CG, Li L, Gewecke NR. Dynamics and function of the tear film in relation to the blink cycle. *Prog Ret Eye Res.* 2015;45: 132–164.
7. Braun RJ, Gewecke NR, Begley CG, King-Smith PE, Siddique JI. A model for tear film thinning with osmolarity and fluorescein. *Invest Ophthalmol Vis Sci.* 2014;55(2): 1133–1142.



# Racial differences in the correlations between structural parameters and ocular blood flow in healthy eyes

Koosha Ramezani<sup>1,2</sup>, Alon Harris<sup>1</sup>, Brent Siesky<sup>1</sup>, Carine Olinde<sup>1</sup>, Darrell WuDunn<sup>1</sup>, Jennifer Eikenberry<sup>1</sup>, Fang-I Chu<sup>1</sup>, Leslie A. Tobe<sup>1</sup>, Betül Kaskan<sup>1</sup>, Lyne Racette<sup>1,2</sup>

<sup>1</sup>Eugene and Marilyn Glick Eye Institute, Indiana University School of Medicine, Department of Ophthalmology, Indianapolis, IN, USA; <sup>2</sup>Department of Ophthalmology, School of Medicine, University of Alabama at Birmingham, Birmingham, AL, USA

## Abstract

**Purpose:** This study aimed to assess differences in the relationship between structural parameters and ocular blood flow between persons of African (AD) and European descent (ED) with healthy eyes.

**Methods:** The relationship between structural and ocular blood flow parameters was assessed in 46 participants (20 AD, 26 ED) with healthy eyes. Disc area (DA), rim area (RA), and retinal nerve fiber layer thickness (RNFLT) were measured. Retrobulbar blood flow was assessed in the ophthalmic (OA), central retinal (CRA), nasal (NPCA), and temporal short posterior ciliary arteries (TPCA). Peak systolic velocity (PSV), end diastolic velocity (EDV), and resistive index (RI) were assessed. Retinal capillary blood flow was also evaluated. Differences between the correlations were determined using the Fisher r-to-z transformation.

**Results:** Significant differences in correlations were observed between the AD and ED groups in the CRA, where PSV and DA were positively correlated in AD ( $r = 0.43$ ) and negatively correlated in ED ( $r = -0.36$ ) ( $\Delta r = 0.79$ ;  $P = 0.01$ ). A similar finding was observed for PSV and RA (AD:  $r = 0.39$ ; ED:  $r = -0.23$ ;  $\Delta r = 0.62$ ;  $P = 0.04$ ). In the inferior hemifield, for the ED group only, the percentage of avascular space and RNFLT were positively correlated ( $r = 0.51$ ,  $P = 0.01$ ), while mean retinal flow and RNFLT were

---

**Correspondence:** Lyne Racette, PhD, Department of Ophthalmology, University of Alabama at Birmingham, Callahan Eye Hospital, 1720 University Blvd, Suite 609, Birmingham, AL 35294, USA.  
E-mail: lracette@uabmc.edu

---

negatively correlated ( $r = -0.50$ ,  $P = 0.01$ ).

*Conclusion:* The relationship between structural parameters (DA and RA) and the blood flow index (PSV) in the CRA, which supplies blood to the superficial layer of the optic nerve head, was significantly different in the healthy eyes of AD compared to ED. More research is required to show how these differences may affect glaucomatous risk.

*Keywords:* glaucoma, ocular blood flow, posterior segment, racial difference

## 1. Introduction

Primary open-angle glaucoma (POAG) is the leading cause of irreversible blindness in the African American population of the United States.<sup>1</sup> Persons of AD are up to six times more likely to be affected by POAG compared to persons of ED.<sup>2,3</sup> In addition, persons of AD are susceptible to earlier development of POAG, higher disease severity, more rapid progression of the disease, and greater visual field impairment compared to persons of ED.<sup>3</sup> The mechanisms underlying the differences in the development and progression rates of POAG between persons of AD and ED remain unknown.

Large population-based trials have linked reduced ocular perfusion pressure (OPP) to the prevalence, incidence, and progression of glaucoma.<sup>4,5</sup> Retinal,<sup>6</sup> choroidal,<sup>7</sup> and retrobulbar<sup>8</sup> blood flow deficiencies have been reported in patients with POAG. Other vascular conditions such as systemic hypertension,<sup>9</sup> aging of the vasculature,<sup>10</sup> and optic disc hemorrhage<sup>11</sup> have also been associated with POAG. Moreover, ocular vascular conditions have been shown to correlate with visual field loss.<sup>6,9</sup> Persons of AD tend to have higher rates of systemic vasculature abnormalities, and it is possible that vascular factors may play a greater role in their higher vulnerability to development and progression of POAG. For example, POAG patients of AD have been shown to have significantly lower blood flow values in all retrobulbar vessels compared to ED patients.<sup>12</sup> One study also showed that in POAG patients of AD, the correlation between changes in ocular blood flow and optic nerve head (ONH) morphology parameters are stronger than in patients of ED. Taken together, this suggests that patients of AD may have a stronger vascular component in the pathogenesis of glaucoma than patients of ED.<sup>13,14</sup>

In healthy eyes, studies have shown thinner corneas, larger optic discs, deeper maximum cup depth, higher intraocular pressure (IOP), and worse performance on visual field tests in persons of AD.<sup>15</sup> Lower blood flow in retrobulbar vessels has been reported in the healthy eyes of AD compared to ED.<sup>16</sup>

A missing element in understanding vascular contributions to the POAG process could be an established knowledge of blood flow changes over the course of development and with aging. Therefore, developing a normative database and

baseline parameters is important with regard to studying racial differences in the development of POAG. Establishing a normative database for ocular blood flow measurements, however, has been historically challenging due to significant overlap between healthy and glaucomatous populations in ocular blood flow measurements, lack of standardization of measurements, and multiple vascular tissue beds relevant to the glaucomatous disease process.<sup>17</sup> The aim of this study was to assess the differences in the correlation between structural parameters and ocular blood flow in the healthy eyes of individuals of AD and ED.

## 2. Materials and methods

One randomly selected eye from 46 participants (20 AD, 26 ED) with healthy eyes based on a complete ocular examination were included in the study. All eyes had open angles, symmetric optic discs with normal appearance (asymmetry of vertical cup-to-disc ratio (CDR)  $\leq 0.2$ ), no hemorrhages or RNFL defects, and IOP of  $< 22$  mmHg. Participants were excluded if they had previously undergone intraocular surgery (except for uncomplicated cataract surgery) or if they had evidence of other ocular diseases. In addition, participants with controlled systemic blood pressure exceeding 140/90 and uncontrolled systemic blood pressure were excluded from the study. Inclusion and exclusion criteria are described in detail elsewhere.<sup>16</sup> All study procedures conformed to the tenets of the Declaration of Helsinki and were approved by the Institutional Review Board at Indiana University School of Medicine. All subjects signed an informed consent prior to entry into the study.

### 2.1. General methodology

Participants were seen on three different visits, each performed at least one day apart. In order to ensure that the eyes remained healthy throughout the duration of the study, all visits were performed over a short time frame (mean of  $41 \pm 35$  days; range of 5 to 200 days). At baseline, participants underwent a complete ocular examination. The ocular blood flow and structural parameters reported in this study were assessed on the third visit. IOP (measured by Goldmann applanation tonometry) and central corneal thickness (CCT, measured by Pachette 2 ultrasonic pachymeter; DGH Technologies, Exton, PA, USA) were obtained based on the average of two and three measurements, respectively. OPP was calculated as  $2/3$  mean arterial pressure (MAP) – IOP.

Retinal capillary blood flow was measured utilizing Heidelberg confocal scanning laser Doppler flowmetry (HRF; Heidelberg Engineering, Heidelberg, Germany), which has been shown to be reproducible.<sup>18</sup> Retrobulbar blood flow velocities were assessed with color Doppler imaging (CDI with the Philips HDI 5000 SonoCT Ultrasound System with the microvascular small parts clinical option; Philips Medical Systems, Bothell, WA, USA) using a 7.5 MHz linear probe. The OA, CRA, NPCA, and

Table 1. Demographics and general health data for the AD and ED groups

	AD (n = 20)	ED (n = 26)	P-value
Age (years)	54.00 ± 8.62	53.36 ± 8.67	0.80
Sex (% female)	55	38	0.41
Family history of glaucoma (%)	25	8	0.21
CCT (µm)	548.34 ± 38.19	563.01 ± 29.52	0.16
IOP (mmHg)	15.20 ± 1.85	15.19 ± 2.04	0.99
MAP (mmHg)	96.22 ± 8.54	94.46 ± 7.92	0.48
OPP (mmHg)	48.94 ± 6.53	47.78 ± 5.35	0.52
Diabetes mellitus (%)	0	0	NA
Heart disease (%)	5	12	0.62

µm: micron; mmHg: millimeters of mercury; NA: not applicable; CCT: central corneal thickness; IOP: intraocular pressure; MAP: mean arterial pressure; OPP: ocular perfusion pressure

TPCA were assessed for PSV and EDV blood flow velocities, and Pourcelot's vascular RI, calculated as  $RI = (PSV - EDV)/PSV$ .<sup>19</sup> Structural assessment included DA, RA, CDR, and RNFLT using the Heidelberg Retina Tomograph III (Heidelberg Engineering, Heidelberg, Germany). Only images with mean pixel height standard deviation of less than 50 µm were used in the analyses.<sup>20</sup>

## 2.2. Statistical analysis

The Fisher's exact test and the 2-tailed, unpaired t-tests were used to compare participant-specific categorical and continuous variables, respectively. Associations between structural parameters and ocular blood flow were derived using the Pearson correlation coefficient. Differences between the correlations in the AD and ED groups were assessed using the Fisher r-to-z transformation. The power of this test is lower than that of tests that consider a single correlation.<sup>21</sup> Given sample sizes of 20 (AD) and 26 (ED), and with the significance level set at  $\alpha = 0.05$ , the power to detect a difference of 0.2 between the correlations of each sample ranged between 0.10 to 0.47 using the Fisher r-to-z transformation.<sup>21</sup> A difference of 0.2 is a convention used when a correlation measure is unknown but different from 0. All statistical analyses were performed using R (R Foundation for Statistical Computing, Vienna, Austria)<sup>22</sup> and Microsoft Excel 2013 (Microsoft, Seattle, WA, USA). The level of significance ( $\alpha$ ) was set at 0.05. Multiple testing corrections were not initially applied for the report in the results.

Table 2. A comparison of the results for retrobulbar blood flow velocities and peripheral vascular resistance, measured by CDI, between participants of AD (n = 20) and ED (n = 26) is presented. Measurements were taken from the OA, CRA, and NPCA/TPCA. In each vessel, PSV and EDV were determined and the Pourcelot vascular RI was calculated (multiple testing corrections are not applied).

		AD (n = 20)		ED (n = 26)		P-value
		Mean	SD	Mean	SD	
<b>OA</b>						
	PSV	22.66	7.64	25.64	9.52	0.24
	EDV	5.44	1.65	6.94	2.56	<b>0.02</b>
	RI	1.08	1.44	0.72	0.07	0.28
<b>CRA</b>						
	PSV	8.30	2.07	8.72	2.62	0.55
	EDV	2.31	0.70	2.96	1.14	<b>0.02</b>
	RI	0.72	0.09	0.66	0.07	<b>0.03</b>
<b>NPCA</b>						
	PSV	7.48	1.42	8.16	2.26	0.22
	EDV	2.44	0.69	2.98	1.28	0.07
	RI	0.67	0.08	0.64	0.08	0.14
<b>TPCA</b>						
	PSV	7.59	1.49	8.55	2.22	0.08
	EDV	2.26	0.48	3.12	1.22	<b>0.002</b>
	RI	0.70	0.07	0.64	0.08	<b>0.01</b>

### 3. Results

No significant differences were observed in demographics and general health data between participants of AD and ED including age, sex, family history of glaucoma, cardiovascular diseases, IOP, MAP, CCT, and OPP (Table 1). Persons of AD were found to have significantly lower EDV in the OA ( $P = 0.02$ ), CRA ( $P = 0.02$ ), and TPCA ( $P = 0.002$ ), and higher RI in the CRA ( $P = 0.03$ ) and TPCA ( $P = 0.01$ ) compared to persons of ED (Table 2). No significant differences between groups were observed for all other retrobulbar blood flow, retinal capillary blood flow, or structural parameters.

Within each group, we assessed the correlations between structural and vascular parameters. In the ED group, significant negative correlations were observed

Table 3. Correlations ( $r$ ) and correlation comparisons ( $\Delta r$ ) between structural and ocular blood flow parameters between participants of AD ( $n = 20$ ) and ED ( $n=26$ )

			AD		ED		$\Delta r$
			$r$	P-value	$r$	P-value	P-value
OA	PSV	DA	-0.11	0.66	-0.22	0.29	0.73
		RA	-0.01	0.96	-0.06	0.77	0.88
		CDR	-0.09	0.70	-0.09	0.65	0.99
		RNFLT	0.01	0.97	0.03	0.89	0.95
	EDV	DA	-0.14	0.56	-0.15	0.45	0.96
		RA	0.03	0.90	-0.20	0.33	0.47
		CDR	-0.16	0.49	0.16	0.43	0.30
		RNFLT	0.19	0.42	-0.06	0.76	0.42
	RI	DA	0.14	0.56	-0.13	0.53	0.40
		RA	-0.02	0.93	0.19	0.35	0.50
		CDR	0.18	0.45	-0.40	<b>0.05</b>	0.06
		RNFLT	0.02	0.92	0.14	0.51	0.73

			AD		ED		$\Delta r$
			$r$	P-value	$r$	P-value	P-value
CRA	PSV	DA	0.43	0.06	-0.36	0.07	<b>0.01</b>
		RA	0.39	0.09	-0.23	0.27	<b>0.04</b>
		CDR	0.15	0.53	-0.28	0.17	0.18
		RNFLT	0.08	0.75	-0.15	0.46	0.47
	EDV	DA	0.29	0.21	-0.29	0.15	0.06
		RA	0.13	0.57	-0.38	0.06	0.09
		CDR	0.28	0.23	0.00	0.98	0.36
		RNFLT	0.10	0.66	-0.18	0.37	0.37
	RI	DA	0.18	0.45	-0.04	0.85	0.50
		RA	0.29	0.21	0.32	0.11	0.94
		CDR	-0.15	0.53	-0.40	<b>0.04</b>	0.39
		RNFLT	-0.08	0.73	0.11	0.60	0.55

			AD		ED		$\Delta r$
			r	P-value	r	P-value	P-value
NPCA	PSV	DA	0.27	0.25	-0.31	0.13	0.06
		RA	0.08	0.73	-0.30	0.14	0.23
		CDR	0.17	0.48	-0.02	0.92	0.56
		RNFLT	-0.36	0.12	-0.24	0.24	0.67
	EDV	DA	0.06	0.80	-0.20	0.34	0.42
		RA	0.03	0.91	-0.38	0.06	0.19
		CDR	0.00	0.99	0.21	0.30	0.51
		RNFLT	-0.09	0.70	-0.24	0.24	0.63
	RI	DA	0.12	0.61	-0.14	0.51	0.42
		RA	0.03	0.89	0.27	0.19	0.45
		CDR	0.10	0.67	-0.46	<b>0.02</b>	0.06
		RNFLT	-0.22	0.36	0.16	0.45	0.23

			AD		ED		$\Delta r$
			r	P-value	r	P-value	P-value
TPCA	PSV	DA	-0.02	0.93	-0.19	0.36	0.60
		RA	0.04	0.88	-0.26	0.20	0.35
		CDR	-0.14	0.55	0.00	1.00	0.65
		RNFLT	-0.38	0.09	-0.21	0.31	0.54
	EDV	DA	-0.19	0.41	-0.04	0.83	0.63
		RA	-0.17	0.48	-0.26	0.20	0.76
		CDR	0.02	0.93	0.27	0.19	0.44
		RNFLT	0.00	1.00	-0.07	0.72	0.82
	RI	DA	0.28	0.22	-0.14	0.49	0.17
		RA	0.27	0.24	0.12	0.58	0.60
		CDR	-0.07	0.76	-0.41	<b>0.04</b>	0.26
		RNFLT	-0.26	0.27	-0.12	0.56	0.65

OA: ophthalmic artery; CRA: central retinal artery; NPCA/TPCA: nasal/temporal short posterior ciliary arteries; PSV: peak systolic velocity; EDV: end diastolic velocity; RI: resistive index; DA: disc area; RA: rim area; CDR: cup-to-disc ratio; RNFLT: retinal nerve fiber layer thickness

Table 4. Correlations ( $r$ ) and correlation comparisons ( $\Delta r$ ) between structural and HRF parameters in the superior and inferior hemifields between participants of AD and ED

			AD (n = 19)		ED (n = 24)		$\Delta r$
			r	P-value	r	P-value	P-value
Inferior hemifield	Mean retinal flow (AU)	DA	-0.01	0.96	0.16	0.47	0.61
		RA	-0.08	0.75	0.12	0.57	0.54
		CDR	0.01	0.97	-0.21	0.31	0.49
		RNFLT	0.07	0.79	-0.50	<b>0.01</b>	0.06
	Zero flow pixel (%)	DA	-0.04	0.86	-0.12	0.57	0.80
		RA	0.00	0.99	0.23	0.28	0.49
		CDR	-0.11	0.66	-0.14	0.52	0.92
		RNFLT	0.13	0.59	0.51	<b>0.01</b>	0.19
			AD (n = 19)		ED (n = 22)		$\Delta r$
			r	P-value	r	P-value	P-value
Superior hemifield	Mean retinal flow (AU)	DA	-0.30	0.21	0.06	0.79	0.27
		RA	-0.20	0.42	0.18	0.41	0.25
		CDR	-0.18	0.45	-0.32	0.15	0.67
		RNFLT	0.14	0.58	-0.41	0.06	0.09
	Zero flow pixel (%)	DA	0.12	0.63	-0.12	0.60	0.49
		RA	-0.01	0.97	0.10	0.65	0.74
		CDR	0.08	0.73	-0.17	0.45	0.45
		RNFLT	-0.28	0.24	0.25	0.26	0.11

DA: disc area; RA: rim area; CDR: cup-to-disc ratio; RNFLT: retinal nerve fiber layer thickness; AU: arbitrary unit

between RI and CDR in all arteries ( $r$  coefficients range:  $-0.46$  to  $-0.40$ ). These correlations were not significant in the AD group ( $r$  coefficients range:  $-0.15$  to  $0.18$ ) (Table 3). Similar results were observed in retinal capillary blood flow, where significant correlations were observed between both mean retinal flow ( $r = -0.50$ ,  $P = 0.01$ ) and zero flow pixel ( $r = 0.51$ ,  $P = 0.01$ ), and RNFLT (in the inferior hemifield) in the ED group only (Table 4).

Finally, we determined whether the correlations between structural and blood flow parameters were different between the AD and ED groups. Significant differences were observed in the CRA, where PSV and DA were positively correlated in the AD group ( $r = 0.43$ ) and negatively correlated in the ED group ( $r = -0.36$ ) ( $\Delta r = 0.79$ ;  $P = 0.01$ ) (see Fig. 1; Table 3). A similar finding was observed for PSV and

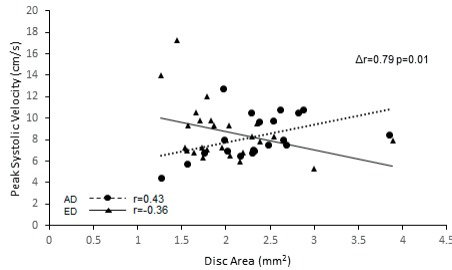


Fig. 1. The association between PSV and DA in the CRA is shown.

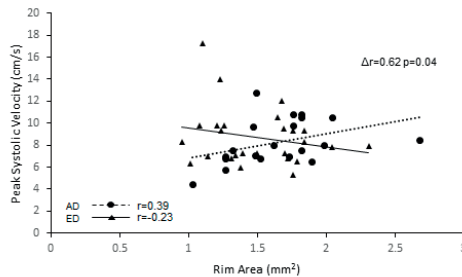


Fig. 2. The association between PSV and RA in the CRA is shown.

RA, with a positive correlation in the AD group ( $r = 0.39$ ) and a negative correlation in the ED group ( $r = -0.23$ ) ( $\Delta r = 0.62$ ;  $P = 0.04$ ) (see Fig. 2; Table 3).

## 4. Discussion

The present study aimed to investigate differences in correlations between ONH morphology and retrobulbar and retinal blood flow in healthy eyes between persons of AD and ED. Some reports have shown correlations between structural measurements (e.g., RNFLT, CDR) and ONH blood flow in POAG patients. Resch *et al.*,<sup>23</sup> for example, have reported that ONH blood flow was negatively correlated with CDR and positively correlated with the RNFLT cross-sectional area in POAG patients. In addition, Siesky *et al.*<sup>24</sup> reported significant differences in correlations between reductions in retrobulbar and retinal capillary blood flow and changes in ONH and retinal morphology between patients of AD and ED in a longitudinal cohort of patients with POAG. Our study assessed whether such differences in correlations exist between healthy eyes of AD and ED. If so, these differences could explain, at least in part, disparities in glaucoma development and progression between these populations.

In the present cross-sectional pilot study, we observed different correlations

between structural parameters and ocular blood flow in the AD and ED groups with healthy eyes. In the CRA, which nourishes the superficial layers of the ONH, we found a positive correlation between PSV and both DA and RA in the AD group, while these correlations were negative in the ED group. Although the correlations in each group did not reach statistical significance, the difference in correlations between the two groups was significant.

We found an unanticipated uniform pattern of significant negative correlations between RI and CDR in all retrobulbar arteries in the ED group only. Although RI is known to be highly correlated to downstream vascular resistance in blood vessels, it is not equal to vascular resistance, as it may be influenced by several anatomical and physiological parameters not related to resistance such as vascular compliance and blood pressure profile.<sup>25</sup> Because of the variability in the size of the disc in healthy eyes, CDR can be quite variable in persons with healthy eyes and may not accurately represent all changes at the ONH.<sup>26</sup> The rise in vascular resistance may lead to defective ONH circulation, neuroretinal rim thinning, and expanding CDR. While our sample size was relatively small, we observed a trend of significant correlation between RI and CDR in all retrobulbar vessels in healthy eyes of the ED group only. Although, our study did not look at patients with POAG, it is possible that the difference in trends that we observed between the AD and ED healthy eyes plays a role in explaining the vulnerability of people of AD to develop POAG. This should be explored in future studies, perhaps longitudinally, to determine how this racial difference impacts the development of POAG.

Similar to the results we reported in Kaskan *et al.*,<sup>16</sup> we found significant differences between persons of AD and ED in retrobulbar blood flow. This was expected, given that a subset of participants was included in both studies (22 persons of the ED and 11 persons of the AD group). After correcting for multiple comparisons, EDV was significantly lower and RI was significantly higher in the TPCA in the AD compared to the ED group. These racial differences were observed in healthy eyes, in the absence of differences in IOP, diabetes, systemic blood pressure, and heart disease between the two groups. No significant differences between the groups were observed either in retinal capillary blood flow or in the correlations of ONH morphology and retinal capillary blood flow. However, in the inferior hemifield of the ED healthy eyes, a negative correlation was observed between mean retinal blood flow and RNFLT, and a positive correlation between capillary sparsity and RNFLT. A recent study by Kanakamedala *et al.* longitudinally assessed the correlations between changes of ONH parameters (such as cup area, RA, and linear CDR) and changes in retinal capillary blood flow in POAG patients of AD and ED.<sup>13</sup> In their study, only patients of AD showed significant and positive correlations between changes in retinal capillary blood flow of the temporal retina and changes in ONH morphology. These correlations were weak and not significant in patients of ED. Unlike their finding, we observed significant correlation between structural parameters and retinal capillary blood flow measurements only in the ED group.

The present study has several limitations. First, race was determined based on self-report. However, self-reported race has been shown to correlate well with more sophisticated racial classification, such as genetic admixture techniques.<sup>27</sup> Second, participants with controlled systemic hypertension and family history of glaucoma were included, although both groups had a similar percentage of individuals with systemic hypertension and family history. Third, the power to detect significant differences between the AD and ED groups using Fisher *r*-to-*z* transformation was relatively low. However, we found significant differences between the AD and ED groups despite relatively low statistical power. This not only suggests that the differences in correlations exist, but that they are likely greater than 0.2. Additionally, the lack of significant findings between the groups for some of the other correlations may be due to lack of power rather than lack of an underlying difference.

Several factors, such as ocular structural properties and blood flow, as well as ethnicity, may contribute individually, or synergistically, to the development and progression of POAG. While the correlation between many of these factors has been previously studied, isolating each of these factors has been a challenge. Many mathematical approaches have been suggested in conjunction with clinical studies over the last decade in order to quantify the contribution of each possible risk factor for POAG development.<sup>28</sup> The differences in structural and ocular blood flow parameters in healthy eyes which were investigated in our study could be implemented in mathematical models in the future. This could deepen our understanding of the mechanisms underlying racial differences in the development and progression of glaucoma.

In conclusion, the findings of this study suggest the presence of differences in the relationship between structural and ocular vascular parameters in healthy eyes of persons of AD and ED. Our results can be helpful in designing future research to identify the specific mechanisms, including possible vascular factors, which contribute to the POAG disease disparity experienced by persons of AD.

## Acknowledgements

This study was presented at the 2016 Annual Meeting of the Association for Research in Vision and Ophthalmology (ARVO). The study was supported in part by: a Biomedical Research Grant from Indiana University School of Medicine (IN, USA) (Lyne Racette); an Indiana University–Purdue University Indianapolis Enhanced Mentoring Program with Opportunities for Ways to Excel in Research (EMPOWER) award (IN, USA) (Lyne Racette); EyeSight Foundation of Alabama (AL, USA); and by an unrestricted grant from Research to Prevent Blindness (NY, USA). Dr. Alon Harris would like to disclose that he receives remuneration from Stemnion (USA), Biolight (Israel), NanoRetina (Israel), AdOm (Israel), Science Based Health (USA), Isarna Therapeutics (Germany), CIPLA (India), and Shire (Ireland) and Ono Pharmaceuticals

(Taiwan) for serving as a consultant. Alon Harris also holds an ownership interest in AdOm (Israel), Nano Retina (Israel), and Oxymap (Iceland). All relationships listed above are pursuant to Indiana University's policy on outside activities. The authors have no conflict of interest to disclose pertaining to this study.

## References

1. Congdon N, O'Colmain B, Klaver CC, et al. Causes and prevalence of visual impairment among adults in the United States. *Arch Ophthalmol.* 2004;122(4):477-485.
2. Friedman DS, Wolfs RC, O'Colmain BJ, et al. Prevalence of open-angle glaucoma among adults in the United States. *Arch Ophthalmol.* 2004;122(4):532-538.
3. Racette L, Wilson MR, Zangwill LM, Weinreb RN, Sample PA. Primary open-angle glaucoma in blacks: a review. *Surv Ophthalmol.* 2003;48(3):295-313.
4. Leske MC, Wu S-Y, Nemesure B, Hennis A. Incident open-angle glaucoma and blood pressure. *Arch Ophthalmol.* 2002;120(7):954-959.
5. Tielsch JM, Katz J, Sommer A, Quigley HA, Javitt JC. Hypertension, perfusion pressure, and primary open-angle glaucoma: a population-based assessment. *Arch Ophthalmol.* 1995;113(2):216-221.
6. Chung HS, Harris A, Kagemann L, Martin B. Peripapillary retinal blood flow in normal tension glaucoma. *Br J Ophthalmol.* 1999;83(4):466-469.
7. Yin ZQ, Vaegan, Millar TJ, Beaumont P, Sarks S. Widespread choroidal insufficiency in primary open-angle glaucoma. *J Glaucoma.* 1997;6(1):23-32.
8. Harris A, Sergott RC, Spaeth GL, Katz JL, Shoemaker JA, Martin BJ. Color Doppler analysis of ocular vessel blood velocity in normal-tension glaucoma. *Am J Ophthalmol.* 1994;118(5):642-649.
9. Galassi F, Sodi A, Ucci F, Renieri G, Pieri B, Baccini M. Ocular hemodynamics and glaucoma prognosis: a color Doppler imaging study. *Arch Ophthalmol.* 2003;121(12):1711-1715.
10. Ehrlich R, Kheradiya NS, Winston DM, Moore DB, Wirostko B, Harris A. Age-related ocular vascular changes. *Graefes Arch Clin Exp Ophthalmol.* 2009;247(5):583-591.
11. Drance S, Anderson DR, Schulzer M. Collaborative Normal-Tension Glaucoma Study G. Risk factors for progression of visual field abnormalities in normal-tension glaucoma. *Am J Ophthalmol.* 2001;131(6):699-708.
12. Siesky B, Harris A, Racette L, et al. Differences in ocular blood flow in glaucoma between patients of African and European descent. *J Glaucoma.* 2015;24(2):117.
13. Kanakamedala P, Harris A, Siesky B, et al. Optic nerve head morphology in glaucoma patients of African descent is strongly correlated to retinal blood flow. *Br J Ophthalmol.* 2014;98(11):1551-1554.
14. Siesky B, Harris A, Racette L, et al. Differences in ocular blood flow in glaucoma between patients of African and European descent. *J Glaucoma.* 2015;24(2):117-121.
15. Racette L, Liebmann JM, Girkin CA, et al. African Descent and Glaucoma Evaluation Study (ADAGES): III. Ancestry differences in visual function in healthy eyes. *Arch Ophthalmol.* 2010;128(5):551-559.
16. Kaskan B, Ramezani K, Harris A, et al. Differences in ocular blood flow between people of African and European descent with healthy eyes. *J Glaucoma.* 2016;25(9):709-715.
17. Rusia D, Harris A, Pernic A, et al. Feasibility of creating a normative database of colour Doppler imaging parameters in glaucomatous eyes and controls. *Br J Ophthalmol.* 2011;95(9):1193-1198.
18. Jonescu-Cuyper C, Harris A, Wilson R, et al. Reproducibility of the Heidelberg retinal flowmeter in determining low perfusion areas in peripapillary retina. *Br J Ophthalmol.* 2004;88(10):1266-1269.
19. Williamson TH, Harris A. Color Doppler ultrasound imaging of the eye and orbit. *Surv Ophthalmol.* 1996;40(4):255-267.

20. Fingeret M, Flanagan J, Liebmann JM. The essential HRT primer. San Ramon: Jocoto Advertising; 2005.
21. Kenny DA. Statistics for social and behavioral science. Library of Congress; 1987.
22. R Core Team. R: A language and environment for statistical computing. Vienna, Austria: R Foundation for Statistical Computing; 2017. Available from: <http://www.R-project.org/>.
23. Resch H, Schmidl D, Hommer A, et al. Correlation of optic disc morphology and ocular perfusion parameters in patients with primary open angle glaucoma. *Acta Ophthalmol.* 2011;89(7):e544-549.
24. Siesky B, Harris A, Carr J, et al. Reductions in retrobulbar and retinal capillary blood flow strongly correlate with changes in optic nerve head and retinal morphology over 4 years in open-angle glaucoma patients of African descent compared with patients of European descent. *J Glaucoma.* 2016;25(9):750-757.
25. Stalmans I, Vandewalle E, Anderson DR, et al. Use of colour Doppler imaging in ocular blood flow research. *Acta Ophthalmol.* 2011;89(8):e609-e630.
26. Balazsi AG, Drance SM, Schulzer M, Douglas GR. Neuroretinal rim area in suspected glaucoma and early chronic open-angle glaucoma: correlation with parameters of visual function. *Arch Ophthalmol.* 1984;102(7):1011-1014.
27. Rosenberg NA, Pritchard JK, Weber JL, et al. Genetic structure of human populations. *Science.* 2002;298(5602):2381-2385.
28. Guidoboni G, Harris A, Arciero JC, et al. Mathematical modeling approaches in the study of glaucoma disparities among people of African and European descents. *J Coupled Syst Multiscale Dyn.* 2013;1(1):1-21.



---

# Using mathematics to avoid blindness in diabetics

Arieh Helfgott<sup>1,2</sup>, Ariella ER Helfgott<sup>3,4</sup>, Sean Mullany<sup>5,6</sup>

<sup>1</sup>The Australian Mathematical Society, Canberra, Australia; <sup>2</sup>The Cardiac Society of Australia and New Zealand, Sydney, Australia; <sup>3</sup>Copernicus Institute of Sustainable Development, Utrecht University, Utrecht, The Netherlands; <sup>4</sup>Environmental Change Institute, University of Oxford, Oxford, UK; <sup>5</sup>The Royal Adelaide Hospital, Adelaide, Australia; <sup>6</sup>Department of Medicine, Flinders University, Adelaide, Australia

## Abstract

*Purpose:* Avoid diabetic-blindness by applying five simple mathematically-inspired treatments that achieve life-long recovery from advanced diabetic retinopathy (ADR), without laser treatments or Avastin (Hoffmann-La Roche, Basel, Switzerland) injections.

*Methods:* A mathematical model of ADR is derived; it is based on fluid leakage from abnormal ‘holes’ in small retinal blood vessels. First, the volume of a microscopic fluid droplet leaking from a single small vein-hole during a single heartbeat is derived from the Navier-Stokes flow-equations. Then, total fluid volume leaking into the retina from all M vein holes in N heartbeats is determined. Six parameters in the equations of the model with significant influence on leakage *rates* and leaked *volumes* are identified. These insights are used to design and then apply five simple, novel, and efficient therapeutic treatments, T1 to T5, that may achieve recovery from ADR without laser surgery or Avastin injections. Daily rates, as well as total volumes, of macular fluid *accumulation*, *removal* (by eye-pumps), and *leakage* are calculated from optical coherence tomography (OCT)-measured macular thicknesses.

*Results:* Ten years ago, this paper’s primary author, Arieh Helfgott (AH), suffered from ADR that no longer responded to laser surgery. After *simultaneous* application of treatments T1-T5, AH recovered from ADR in 42 days and has been free of ADR for over ten years, without needing Avastin injections. Leakage-volumes were shown to be very sensitive to small changes in hole diameters. In ADR, modest increases of 2.4%, 5.7%, 10.7%, 15%, and 19% in hole diameters induce impressive 10%, 25%,

---

**Correspondence:** Dr. Arieh Helfgott E-mail: [ariehhelfgott@bigpond.com](mailto:ariehhelfgott@bigpond.com)

---

50%, 75%, and 100% (volume-doubling) increases in leakage volumes, respectively. In recovery from ADR, modest decreases of  $-2.6\%$ ,  $-5.4\%$ ,  $-8.5\%$ ,  $-12\%$ , and  $-15.9\%$  in hole diameters induce equally impressive  $-10\%$ ,  $-20\%$ ,  $-30\%$ ,  $-40\%$ , and  $-50\%$  (volume-halving) decreases in leakage volumes, respectively.

*Conclusion:* In AH's case, mathematics helped in avoiding blindness from ADR. *Simultaneous* application of mathematics-inspired treatments T1-T5 resulted in reduced leakage from holes, elimination of retinal swelling (RS), and sustained recovery from ADR. With high sensitivity to hole diameters, advancing DR can easily become unmanageable, while recovery from ADR may possibly be achievable in approximately six weeks using efficient blood pressure (BP) control and small 'repairs' leading to reduction in hole diameters. The pumping rate of the eye is colossal; eye pumps can remove a macula-volume-equivalent in approximately 44 days. This is very helpful in recovery from ADR, and spectacular for such microscopic pumps.

*Keywords:* advanced diabetic retinopathy (ADR) treatment, blindness, blood flow, diabetic retinopathy (DR), diabetes, leaking blood vessels, macula, mathematical model, retina

## 1. Introduction

### 1.1 Diabetic retinopathy (DR)

DR is a serious sight-threatening complication of diabetes. In 2013, the Australian Baker Institute reported that DR is a leading cause of irreversible blindness in Australian adults, and the leading cause of blindness in working age adults in the world.<sup>1</sup> More recent epidemiological studies confirm that DR is a leading cause of vision loss and blindness *globally* (e.g., 2015 review by Lee *et al.*).<sup>2</sup> As rates of diabetes rise in both developed and developing countries, and as ageing and life expectancy of the population with diabetes increase, vision impairment and blindness caused by diabetic eye disease is an issue of growing global significance.<sup>2</sup>

The excellent texts by Gloria Wu<sup>3</sup> and Jon Walker<sup>4</sup> describe the basic data on DR, its epidemiology, pathogenesis, and current guidelines for treatment. Over time, diabetes gradually damages tiny blood vessels in the microcirculation of the retina (arterioles, capillaries, venules, etc). This damage can eventually lead to formation of abnormal 'holes' in retinal blood vessel walls.<sup>3,4</sup> DR occurs when the vessels leak blood and fluids from the holes into the retina, which causes retinal tissue to swell (retinal edema). The result is cloudy or blurred vision. DR usually affects both eyes. The longer a person has diabetes, the more likely they will develop DR.<sup>3,4,5</sup> If left untreated, DR can cause blindness.

In advancing DR, retinal blood vessels eventually become so abnormal and full of *leaking holes* (Table 15.9 in Wu),<sup>3</sup> that they lose significant functionality. In an attempt to improve retinal blood circulation, new blood vessels begin to grow

in the retina and into the vitreous. This proliferative retinal neo-vascularization is the more advanced form of DR. The new blood vessels are abnormal; they are very *thin-walled*, fragile, and ‘leakier’ than ordinary retinal vessels, and so they may leak blood into the back of the eye, blocking vision.<sup>3,4</sup>

Even though there is no cure for DR, there are available treatments;<sup>3</sup> laser treatment (photocoagulation) is usually very effective at preventing vision loss if it is done before the retina has been severely damaged. Sometimes, injections of an anti-vascular endothelial growth factor (VEGF) drug, such as Avastin, help in shrinking *new* blood vessels in proliferative DR. In general, the earlier DR is detected, the easier it is to treat and the more likely vision will be preserved. Also, controlling blood sugar levels is always important, even after successful treatments for DR, since this will keep DR from getting worse.

Retinal thickness at various retinal locations is a good quantifier of RS. It is measured in microns (1 micron = 1 millionth of a meter). In normal eyes, average foveal thickness at the center of the macula is about 200 microns or less.<sup>6</sup> In ADR, foveal thickness can increase further and further and, if not treated, can reach about 800 microns (Fig. 1 in Browning)<sup>7</sup> at which point the patient is considered clinically blind. The status of current clinical thinking on DR can be summarized as follows:<sup>3,4</sup>

1. DR is a complication of diabetes that affects the eyes. Vision loss or blindness can occur.
2. DR is caused by damage to blood vessels in retinal tissue at the back of the eye.
3. Treatment can help, but this condition cannot be cured.
4. DR requires a medical diagnosis.
5. Laboratory tests or imaging are always required.
6. DR is chronic: it can last for years or be life-long.
7. Poorly controlled blood sugar level is a significant risk factor.
8. Early symptoms include floaters, blurriness, dark areas of vision, and difficulty perceiving colors.
9. Mild cases of DR may be treated with careful diabetes management.
10. Advanced DR cases may require laser treatment, surgery, or injections of an anti-VEGF drug such as Avastin.

This paper presents an alternative perspective, namely, that ADR cases may perhaps also be successfully treated with simultaneous application of five other measures, T1 to T5, described in the Methods section below.

## **1.2. Some basic retina details for mathematicians and engineers**

The retina is the light-sensitive lining at the back of the eye. The macula is a small but vital area of the retina, about 5.5 mm in diameter, and is the part of the retina that is the most densely packed with seeing cells. The macula produces clear central (focused) vision, allowing us to see fine detail and colors. The rest of the retina is for side (peripheral) vision.

Blood vessels at the back of the eye nourish the retina. The inner layers of the retina get their blood supply from retinal arteries and veins, which run within the retina itself. The arteries help carry oxygen and nutrients to the retina, and veins drain blood away from the retina and back towards the heart. The fovea is a tiny pit at the very center of the macula that provides the clearest vision of all. Only in the fovea are the layers of the retina spread aside to let light fall directly on the cones, the cells that provide the sharpest image. It is also called the central fovea (fovea centralis).

### 1.3. Retinal and macular thickness and volume

OCT is commonly used to reliably measure macular *thickness* and *volume*. In the north China Handan Eye Study,<sup>8</sup> macular thickness in 2230 eyes of healthy normal subjects was measured with Zeiss Stratus OCT Model 3000 scans. Scans were performed over maculae within a diameter  $D_m = 6$  mm, divided into three regions (central, inner, and outer, with a diameter of 1, 3, and 6 mm, respectively), and nine quadrants (one in the central region, and four each in the inner and outer regions). The study<sup>8</sup> found mean total macular volume in normal subjects to be  $V_{m\infty} = 6.76$  mm<sup>3</sup>. The macular surface area contained within diameter  $D_m = 6$  mm is  $S_m = 28.274$  mm<sup>2</sup> ( $\pi \times 9$ ). Hence, mean total macular thickness in normal subjects is  $H_{m\infty} = 0.239$  mm = 239 microns ( $6.76$  mm<sup>3</sup> /  $28.274$  mm<sup>2</sup>). Here the infinity symbol,  $\infty$ , stands for time-unchanging thickness or volume, and  $m$  for macula. In studies of different ethnic groups,<sup>8</sup> measured  $V_{m\infty}$  was: 6.486 mm<sup>3</sup> (India); 6.660 mm<sup>3</sup> (USA); 7.100 mm<sup>3</sup> (China); and 6.780 (UK). The mean of the four ethnic groups was again  $V_{m\infty} = 6.76$  mm<sup>3</sup>; hence, this value was used in this paper.

The older Zeiss Stratus is a time-domain device (TD-OCT), whereas most new devices, like the Zeiss Cirrus or Heidelberg Spectralis, are spectral-domain (SD-OCT) devices. The new SD-OCT devices can acquire much more information in much less time, providing *more accurate* measurements of thickness and volume.<sup>4</sup> However, different new OCT devices can produce noticeably different results, a comparison of which is beyond the scope of this paper.

The above mean macular thickness and volume were obtained with ‘old’ TD-OCT machines, available more than ten years ago. The macular OCT scans of this paper’s primary author (AH), which form the basis of calculations in the Methods section, were also obtained more than ten years ago with an old TD-OCT machine. For compatibility reasons, it was therefore appropriate to use  $V_{m\infty} = 6.76$  mm<sup>3</sup> in this paper. The average surface area of the *whole* retina,  $S$ , is now a known parameter. Most recently (2017), using magnetic resonance imaging, Nagra<sup>9</sup> reported an average  $S$  of 1363 mm<sup>2</sup>. OCT scans for diameters greater than  $D_m = 6$  mm are currently not available in the clinical setting.

#### 1.4. Proposed mechanism of fluid leakage from abnormal holes in retinal blood vessels

In what follows, blood vessels of the retinal microcirculation (arterioles, pre-capillaries, capillaries, venules, etc.) are collectively referred to as ‘small veins’ or just ‘veins’, and all pressures are defined relative to the atmospheric pressure.

Pressure within small veins is pulsatile, showing periodic fluctuations that can be quite considerable.<sup>10</sup> In normal cats, the pressure consists of a virtually constant pressure, upon which small cardiac oscillations are superimposed. Normal amplitude of oscillations is approximately 1-2 mmHg (2-4 mmHg total pressure variation), but amplitude could increase to about twice this level, *i.e.*, 2-4 mmHg (4-8 mmHg total pressure variation), if the precapillary sphincter became dilated (p. 371 and Fig. 13.19 in Caro *et al.*).<sup>10</sup> In *hypertensive* cats, amplitude of oscillations can be approximately 1 mmHg greater than in normo-tensive cats (estimated from Figs. 13.16 and 13.18 in Caro *et al.*).<sup>10</sup> Hence, in hypertensive cats, amplitude of oscillations can be approximately 3-5 mmHg, and so *periodic cardiac pressure fluctuations inside small veins can be approximately 6-10 mmHg.*

Information gained from the cat studies provides a clear idea of temporal cardiac pressure variations inside small veins. Cats (felines) are commonly and successfully used in cardiovascular research due to their similarity in anatomical basis and physiological functions with humans. Accordingly, in this study it was assumed that the above cat information also applies to *human subjects* and, in particular, to *hypertensive diabetic human subjects*. That is, it was assumed that in ADR, periodic cardiac pressure fluctuations can be of the order of 6-10 mmHg, due to increased pulsatile pressure in larger central arteries (aorta, etc.).

Let:

1.  $P_1(t) = P_{\text{VEIN}}(t)$  = Transient pulsatile pressure inside small retinal veins, at the inlet to abnormal holes in their walls (intravascular pressure); and
2.  $P_2(t) = P_{\text{RET}}(t)$  = Pressure in the interstitial retinal space outside abnormal holes (extravascular pressure).

Extravascular pressure  $P_{\text{RET}}(t)$  in retinal tissue surrounding leaking veins can vary with time, but is normally fairly *constant* and slightly sub-atmospheric (p. 376-377 in Caro *et al.*).<sup>10</sup> But intravascular pressure  $P_{\text{VEIN}}(t)$  inside small veins varies during the cardiac cycle, being low during diastole and higher during systole. In normotensive subjects, temporal cardiac pressure variations are small, but in hypertensive human subjects with ADR they can be much larger (6-10 mmHg).

Transmural pressure (TP) drop,  $P_{\text{VEIN}}(t) - P_{\text{RET}}(t)$ , provides the *driving force* for fluid leakage from abnormal holes into the retina. Since  $P_{\text{RET}}(t)$  is almost constant, TP fluctuations are primarily determined by fluctuations in pressure  $P_{\text{VEIN}}(t)$ , the major contributor to TP drop. Because venous pressures  $P_{\text{VEIN}}(t)$  in micro-vessels are generally very low, they were traditionally, and understandably, considered clinically unimportant and were ignored (AH experienced this personally). In ADR,  $P_{\text{VEIN}}(t)$  drives leakage flow from vein holes, and therefore, it should never be ignored.

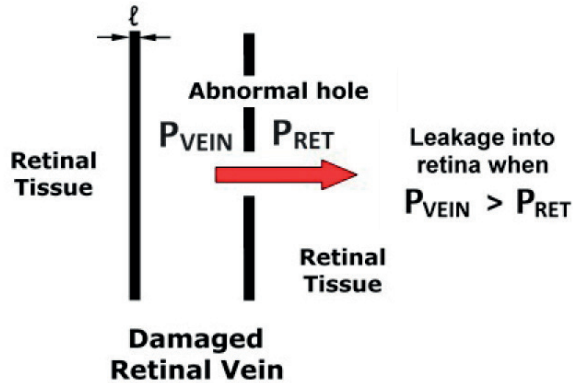


Fig. 1. Diagram illustrating fluid leaking from a tiny abnormal hole in a vein's wall into surrounding retinal tissue. This happens when  $P_{VEIN} > P_{RET}$ , that is, when pressure inside the vein exceeds pressure in the surrounding tissue just outside the vein.  $l$  = blood vessel wall-thickness = abnormal hole length.

Figure 1 graphically illustrates fluid leaking from an abnormal vein-hole into surrounding retinal tissue when pressure  $P_{VEIN} > P_{RET}$  (inside pressure exceeds outside pressure). The positive TP difference forces fluid to leak sideways into the retina through the hole's exit cross-section. Figure 2 diagrammatically illustrates temporal pressure  $P_{VEIN}(t)$  variations inside a small vein during a single cardiac cycle. Pressure rises from low diastolic levels to higher systolic levels, then drops back again to low diastolic levels. Leakage occurs when  $P_{VEIN} > P_{RET}$ , but does not occur when  $P_{VEIN} \leq P_{RET}$ , i.e., when inside pressure is below outside pressure. Fluid leakage starts the moment  $P_{VEIN}$  rises above  $P_{RET}$ , and continues until eventually  $P_{VEIN}$  drops below  $P_{RET}$ , at which point leakage stops (colored peaks in Fig. 2). The longer leaking lasts, the larger the volume of fluid leaking into the retina will be. For *hypertensive* subjects ('High vein BP' curve in Fig. 2), the gold-colored peak area is significantly larger than the green-colored peak area of *normotensive* subjects ('Normal vein BP' curve' in Fig. 2). An important observation can now be made:

*In hypertensive diabetic subjects suffering from ADR, each heartbeat contributes to fluid accumulation in retinal tissues, and so with each successive heartbeat, a diabetic subject gets closer and closer to blindness! This is an unusual and unique medical condition in which one's heartbeats act against one's interests.*

Fortunately, the eye has many pumps capable of removing fluids from the retina. Let  $Q_{PUMP}$  and  $Q_{LEAK}$  denote fluid removal rate by pumps and fluid leakage rate from holes in veins, respectively. In *normotensive* subjects,  $Q_{PUMP} > Q_{LEAK}$ , and the pumps can easily remove excess fluids from the retina because  $Q_{PUMP}$  is larger than the normally low  $Q_{LEAK}$  of normal subjects. This is, however, not the case for *hypertensive* diabetic subjects. In hypertension,  $Q_{PUMP} < Q_{LEAK}$ , and the pumps can no longer cope with the abnormally large leakage rates, thus leading to unwanted RS.

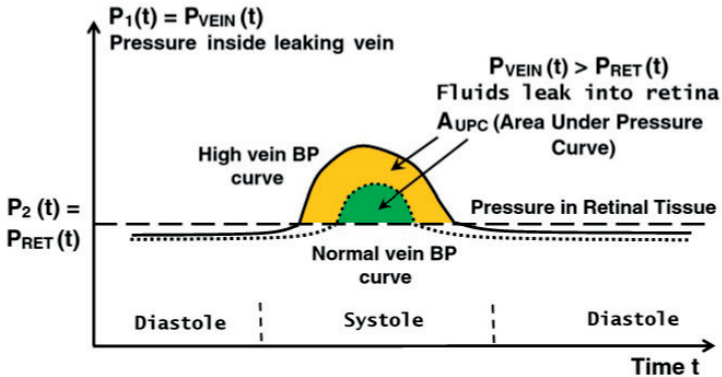


Fig. 2. Diagram showing temporal pressure  $P_{VEIN}(t)$  variations inside a damaged small retinal vein during a single cardiac cycle. Pressure rises from low diastolic levels to higher systolic levels, then drops again to low diastolic levels. Fluid starts leaking when  $P_{VEIN}$  rises above  $P_{RET}$  (pressure in retinal tissue outside vein), and continues leaking until  $P_{VEIN}$  drops below  $P_{RET}$  (see colored peaks). The longer leaking lasts, the larger the amount of fluid leaking into retinal tissues will be. For hypertensive subjects ('High vein BP' curve), the area of the gold-colored peak is significantly larger than the area of the green-colored peak of normotensive subjects ('Normal vein BP' curve).

In AH's ADR, this problem was overcome with five effective treatments that *reduced* (not eliminated!) the rate of fluid leakage from veins, thus restoring the ability of the pumps to cope again with leakages from veins (described below).

## 2. Methods

In this section, a mathematical model of advanced DR is derived; it is based on flow equations describing fluid leakage from abnormal holes in small veins. First, the volume of a fluid droplet leaking into the retina from a single microscopic hole in a single heartbeat is determined. Then, the total volume of fluid leaking into the retina from  $M$  holes in  $N$  heartbeats is calculated by summing up individual droplet volumes over  $M$  holes and  $N$  heartbeats.

Mathematical description of pulsatile flow through a vein's hole requires analysis of unsteady (transient) flows in *very short* tubes. Since there are no fluid mechanics texts that analyze this type of a flow (not even Batchelor's mathematically advanced fluid dynamics book),<sup>11</sup> leakage flow equations were derived from the fundamental continuity and Navier-Stokes equations, after establishing first upper bounds for Reynolds numbers, Womersley numbers, and entrance lengths in abnormal holes 'created' by DR or ADR.

The model is based on the assumption that fluid filtration out of blood micro-ves-

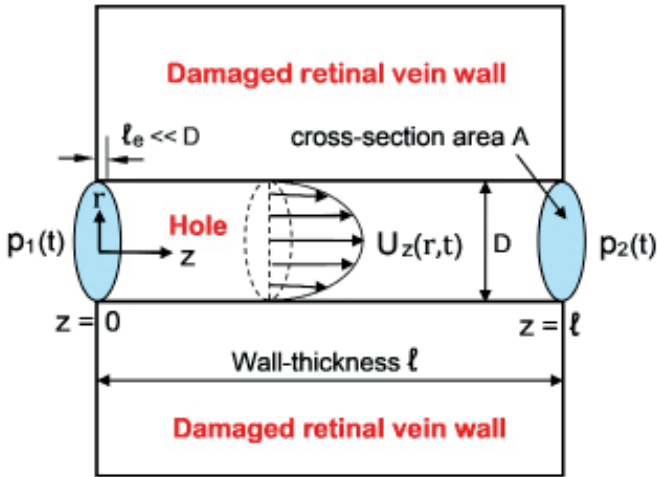


Fig. 3. Schematic diagram of transient leakage flow through a tiny microscopic hole of length  $\ell$  in a damaged blood vessel's wall (enlarged for clarity).  $\ell$  is also the blood vessel's wall-thickness. The flow is subject to the action of a time-changing positive pressure difference  $p_1(t) - p_2(t)$ . Transient fluid velocity  $u_z(r,t)$  has a fully developed parabolic profile that does not change in the  $z$ -direction when  $z > \ell_e$ , where  $\ell_e$  is the entrance length.

sels is entirely due to  $P_{\text{VEIN}}(t) - P_{\text{RET}}(t)$ , the transmural drop in *mechanical* pressure (TDMP). *Oncotic pressure* differences (OPD) have been ignored because in advanced DR, the OPD plays a much less important role in fluid filtration than the TDMP. The following notes support this assumption. A small vein's wall is a semi-permeable membrane, permeable to water, electrolytes, and small molecules within the blood plasma, but not to large protein molecules such as albumin. This establishes an OPD, *i.e.*, an osmotic pressure difference, opposing the TDMP and proportional to the large molecules' transmural concentration difference. Albumin constitutes about 80% of the total OPD. In normal small veins, the wall has a *low* but definite permeability to large molecules such as albumin (p. 409 in Caro *et al.*),<sup>10</sup> implying that some pores in the wall allow transport of larger molecules across the wall. In ADR, a much larger number of pores (holes) have abnormally larger diameters, allowing an increased transport of large molecules across the wall. This results in a large *fall* in concentration difference across the wall, and in a large *reduction* in oncotic pressure differences.

## 2.1. Volume of a fluid droplet leaking into the retina from a single hole in a single heartbeat

The volume of a tiny microscopic fluid droplet,  $V_{\text{DROPLET}}$ , leaking from a *single* vein's hole during a *single* heartbeat is derived in this subsection. In a damaged small vein (Fig. 1), consider the leakage flow in a lateral direction from a hole in the feeding

vein's wall. For simplicity, the hole is viewed as a straight circular pipe of constant cross-section (Fig. 3). In a cylindrical coordinate system ( $r, \theta, z$ ), flow velocity components are  $u_r$  (radial),  $u_\theta$  (circumferential), and  $u_z$  (axial). Velocities  $u_r$  and  $u_\theta$  are taken to be zero (unidirectional flow), and so the focus is on the *time-dependent* axial velocity  $u_z(r, t)$ , which determines the nature of flow within the hole. For unsteady, unidirectional, axisymmetric, incompressible, and viscous flow, the mass conservation (continuity) and Navier-Stokes equations simplify to (e.g., Batchelor):<sup>11</sup>

$$\text{Unidirectional axisymmetric flow } u_r = 0, \quad u_\theta = 0, \quad \frac{\partial u_z}{\partial \theta} = 0 \quad (1)$$

$$\text{Continuity } \frac{\partial u_z}{\partial z} = 0, \quad \text{implying } u_z = u_z(r, t) \quad (2)$$

$$r, \theta - \text{momentums } \frac{\partial p}{\partial r} = 0, \quad \frac{\partial p}{\partial \theta} = 0, \quad \text{implying } p = p(z, t) \quad (3a)$$

$$z - \text{momentum } \rho \frac{\partial u_z}{\partial t} = -\frac{\partial p}{\partial z} + \mu \frac{1}{r} \frac{\partial}{\partial r} \left( r \frac{\partial u_z}{\partial r} \right) \quad (3b)$$

Here  $u_z(r, t)$  is axial velocity,  $p(z, t)$  is pressure,  $\rho$  is fluid density, and  $\mu$  is fluid dynamic viscosity. Since neither the first nor the last term in Equation (3b) depends on  $z$ , we can write:

$$\frac{\partial p}{\partial z} = -G(t) \quad (\text{for } G(t) > 0, \text{ flow is in positive } z\text{-direction}) \quad (4)$$

When  $G(t)$  is positive, pressure  $p(z, t)$  falls in the positive  $z$ -direction, driving fluid sideways out of the vein. For any small retinal vein or abnormal hole of diameter  $D$ , the important Reynolds number is defined by:

$$R_e = \frac{\rho \bar{U} D}{\mu} = \frac{\bar{U} D}{\nu} = \frac{\text{Inertia Forces}}{\text{Viscous Forces}} \quad (5a)$$

where  $\rho$  is density,  $\bar{U}$  is average flow velocity,  $\mu$  is fluid dynamic viscosity, and  $\nu = \mu/\rho$  is fluid kinematic viscosity. Low Reynolds numbers correspond to slow viscous flow in damaged veins and abnormal holes in them. A number of researchers<sup>12,13,14,15</sup> measured the diameter of venules and capillaries at four macula quadrants of *diabetic* and *non-diabetic* human subjects (first two columns in Table 1). Using Equation (5a), corresponding Reynolds numbers for venules and capillaries were calculated for each macular zone (fourth column in Table 1). The averages for the whole macula were:

Non-diabetics:	Venule <sup>12</sup>	$\bar{D}_v = 105.8$ microns,	Venule $R_e = 0.053$
	Capillary <sup>13,14,15</sup>	$\bar{D}_c = 6.9$ microns,	Capillary $R_e = 0.0017$
(5b)			
Diabetics:	Venule <sup>12</sup>	$\bar{D}_v = 110.4$ microns,	Venule $R_e = 0.055$
	Capillary <sup>15</sup>	$\bar{D}_c = 6.3$ microns,	Capillary $R_e = 0.0016$

Table 1. Reynolds number, Womersley number, and entrance length in retinal venules and capillaries

Measured diameters (D) of retinal venules and capillaries		Known <sup>10</sup>	Calculated flow parameters		
Vessel	Diameter (micron)	Average velocity $\bar{U}$ (cm / sec)	Reynolds Number Re	Womersley Number Nw	Entrance Length $\ell_e = 0.06 \times D \times Re$
RETINAL BLOOD VESSELS IN NORMALS <sup>12</sup>					
Venule in upper temporal quadrant	112.6	0.2	0.056	0.080	0.0034 x D
Venule in lower temporal quadrant	107.5	0.2	0.054	0.077	0.0032 x D
Venule in upper nasal quadrant	112.7	0.2	0.056	0.081	0.0034 x D
Venule in lower nasal quadrant	90.2	0.2	0.045	0.064	0.0027 x D
Venule averages (of 4 quadrants)	105.8	0.2	0.053	0.076	0.0032 x D
Capillary (average of all retinal capillaries) <sup>13</sup>	8.3	0.1	0.0021	0.0059	0.00012 x D
Capillary (average of parafoveal capillaries) <sup>15</sup>	7.3	0.1	0.0018	0.0052	0.00011 x D
Capillary (near rim of foveal avascular zone) <sup>14</sup>	5.1	0.1	0.0013	0.0036	0.00008 x D
Capillary averages (of above three)	6.9	0.1	0.0017	0.0049	0.00010 x D
RETINAL BLOOD VESSELS IN DIABETICS <sup>12</sup>					
Venule in upper temporal quadrant	124.9	0.2	0.062	0.089	0.0037 x D
Venule in lower temporal quadrant	102.9	0.2	0.051	0.074	0.0031 x D
Venule in upper nasal quadrant	117.8	0.2	0.059	0.084	0.0035 x D
Venule in lower nasal quadrant	96.1	0.2	0.048	0.069	0.0029 x D
Venule averages (of 4 quadrants)	110.4	0.2	0.055	0.079	0.0033 x D
Diabetic capillaries averages - parafoveal zone <sup>15</sup>	6.3	0.1	0.0016	0.0045	0.00009 x D

<sup>12,13,14,15</sup> are reference numbers;  $Re = \bar{U}D/V =$  Reynolds number;  $\bar{U}$  = average fluid flow velocity in blood vessels;  $D$  = blood vessel diameter;  $V = 0.04$  is fluid kinematic viscosity in  $cm^2/sec$ ;  $Nw = D(\pi f / 2v)^{0.5} =$  Womersley number;  $f = 1.3$  Hz (78 bpm);  $\ell_e =$  entrance length  $= 0.06 \cdot D \cdot Re$

The diameter of abnormal holes is usually smaller than the diameter of the parent micro-vessels, implying that abnormal holes have Reynolds numbers even smaller than those listed in Equation (5b). Thus, the Reynolds numbers listed in Equation (5b) provide *upper bounds* for Reynolds numbers in abnormal holes of micro-vessels. For such very small Reynolds numbers ( $Re \ll 1$ ), inertia (mass) effects were ignored and inertia term  $\partial/\partial t$  was eliminated on the left side of Equation (3b) to give:

$$\mu \frac{1}{r} \frac{\partial}{\partial r} \left( r \frac{\partial u_z}{\partial r} \right) = \frac{\partial p}{\partial z} = -G(t) \quad (3c)$$

The solution of Equation (3c) is found simply by integrating it twice with respect to radius  $r$  and applying boundary conditions:

$$u_z(r, t) = -\frac{r^2}{4\mu} G(t) + C_1 \ln(r) + C_2 \quad (6a)$$

where  $C_1$  and  $C_2$  are integration constants. As  $u_z$  needs to be finite at the hole's center ( $r=0$ ), it follows that  $C_1=0$ . The no-slip boundary condition at the hole's wall requires that  $u_z=0$  at  $r=R$  (radius of hole), yielding:

$$C_2 = \frac{R^2}{4\mu} G(t) . \quad (6b)$$

The final expression for the *time-dependent* pulsatile axial flow velocity  $u_z$  in abnormal holes is then:

$$u_z(r, t) = \frac{(R^2 - r^2)}{4\mu} G(t) , \quad z > \ell_e \text{ (entrance length)} \quad (6c)$$

The *transient* velocity distribution (profile) described by Equation (6c) is *Poiseuille in form*; it is *pulsatile* and *parabolic* at any cross-section along a *very short* hole (short tube), but not parabolic in the *entrance region*  $0 > z < \ell_e$ . So, Equation (6c) is valid only beyond the very short entrance region shown in Figure 3. Note that the parabolic velocity profile described by Equation (6c) remains unchanged at any  $z$ -location. But this  $z$ -unchanged velocity profile varies periodically with time during each heartbeat and from heartbeat to heartbeat. When analyzing this unique transient flow in a very short tube, conditions at the entrance region must be given special consideration. The unsteady pulsating flow in the entrance region depends on both Womersley and Reynolds numbers. The Womersley number determines the nature of this unsteady pulsatile flow and is defined by:<sup>10</sup>

$$N_w = \frac{D}{2} \left( \frac{\omega}{\nu} \right)^{0.5} = D \left( \frac{\pi f}{2\nu} \right)^{0.5} = \frac{\text{Transient Inertia Forces}}{\text{Viscous Forces}} \quad (5c)$$

where  $D$  is small vein or abnormal hole diameter in cm,  $\omega$  is the angular frequency of unsteady pulsatile flow in radians/sec ( $\omega = 2\pi f$ , where  $f$  is heart rate in cycles/sec), and  $\nu=0.04$  is kinematic viscosity in  $\text{cm}^2/\text{sec}$ .

Time-dependent periodic variations in entrance length  $\ell_e$  occur during the pulsatile cycle.<sup>10,16</sup> At high values of  $N_w$  ( $N_w > 1$ ), inertial forces dominate, and these variations can be quite considerable. At very low values of  $N_w$  ( $N_w \ll 1$ ), periodic variations in entrance length  $\ell_e$  can be ignored, because viscous forces dominate, and inertia and time effects can be neglected. For  $N_w \ll 1$ , the entrance length is approximately the same as the steady-state entrance length, primarily dependent on the Reynolds number, and quite well estimated with (e.g., Munson):<sup>17</sup>

$$\ell_e = 0.06 \cdot D \cdot R_e \text{ (laminar flow)} \quad (5d)$$

For retinal venules and capillaries, calculated Womersley numbers in *non-diabetics* were 0.076 and 0.0049, respectively, and in *diabetics* they were 0.079 and 0.0045, respectively (see fifth column in Table 1). There was no difference between diabetics and non-diabetics. For small abnormal holes in retinal venules or capillaries, Womersley numbers for diabetics are even smaller than 0.079 and 0.0045, respectively. This makes Equation (5d) suitable for entrance length calculations. The 0.079 and 0.0045 values provide *upper bounds* for  $N_w$  in abnormal holes located in venules and capillaries of diabetics.

Entrance lengths  $\ell_e$  at various macular quadrants were calculated with Equation (5d) and listed in the last column of Table 1. For macular venules and capillaries, entrance lengths in *non-diabetics* were  $0.0032 \cdot D$  and  $0.0001 \cdot D$ , respectively, whereas in *diabetics* they were  $0.0033 \cdot D$  and  $0.00009 \cdot D$ , respectively. There was no difference between diabetics and non-diabetics. For *holes* in venules or capillaries of diabetics, entrance lengths are even shorter than  $0.0033 \cdot D$  and  $0.00009 \cdot D$ , respectively. So, entrance length is a very small multiple of the holes' diameter in micro-vessels of diabetics (Fig. 3). The  $0.0033 \cdot D$  and  $0.00009 \cdot D$  values provide *upper bounds* for entrance lengths in abnormal holes of macular micro-vessels of diabetics.

For very short entrance lengths ( $\ell_e \ll D$ ), it was assumed that  $\ell_e \approx 0$  and that velocity profiles are fully developed and parabolic along the entire z-length of the hole. Figure 3 shows the vanishingly small entrance region of a hole. Let  $R = \frac{1}{2}D$  be the radius,  $A = \frac{1}{4} \pi D^2$  the cross-sectional area, and  $\ell$  the length of the hole. Note that the hole length  $\ell$  is actually the vein's wall-thickness. On the basis of two recent studies, hole-length is on average 18 microns.<sup>18,19</sup> Solving Equation (4) subject to pressure  $p = p_1(t)$  at  $z = 0$  and  $p = p_2(t)$  at  $z = \ell$ , yielded the pressure distribution  $p(z, t)$  along the z-direction inside the hole:

$$p(z, t) = p_1(t) - G(t)z = p_1(t) - \frac{[p_1(t) - p_2(t)]}{\ell} z \quad (7a)$$

$$\text{in which } G(t) = \frac{[p_1(t) - p_2(t)]}{\ell} \quad (7b)$$

At any given instant of time  $t$ , pressure drops linearly with  $z$  along the hole, but is constant across each cross-section. This linear z-pressure-drop varies, however,

with time  $t$  during a single heartbeat. With  $u_z(r, t)$  known from Equation (6c), the *transient* rate of fluid volume leaking from the hole's exit cross-section is given by the time-dependant rate relation:

$$Q(t) = \int_0^R u_z 2\pi r dr = \frac{\pi R^4}{8\mu} G(t) = \frac{\pi R^4}{8\mu\ell} [p_1(t) - p_2(t)] \quad , \quad \text{for } p_1(t) > p_2(t) \quad (8a)$$

in which we have used Equation (7b). In terms of diameter  $D = 2R$ , or area  $A = \pi R^2$ ,  $Q(t)$  takes the forms:

$$Q(t) = \frac{\pi D^4}{128\mu\ell} [p_1(t) - p_2(t)] = \frac{1}{8\pi} \frac{A^2}{\mu\ell} [p_1(t) - p_2(t)] \quad , \quad \text{for } p_1(t) > p_2(t) \quad (8b)$$

Finally, noting that  $p_1 = P_{\text{VEIN}}$  and  $p_2 = P_{\text{RET}}$ , the volume of a single *droplet* of fluid leaking from the hole's exit cross-section during a single heartbeat is given by:

$$V_{\text{DROPLET}}^{\text{LEAK}} = \int_0^T Q(t) dt = \frac{\pi D^4}{128\mu\ell} A_{\text{UPC}} = \frac{1}{8\pi} \frac{A^2}{\mu\ell} A_{\text{UPC}} \quad , \quad \text{for } P_{\text{VEIN}}(t) > P_{\text{RET}}(t) \quad (9a)$$

$$\text{in which } A_{\text{UPC}} = \int_0^T [P_{\text{VEIN}}(t) - P_{\text{RET}}(t)] dt \quad , \quad \text{for } P_{\text{VEIN}}(t) > P_{\text{RET}}(t) \quad (9b)$$

Here,  $T$  is the duration of a single heartbeat (also known as 'cycle length'), and  $A_{\text{UPC}}$  is the area under the vein's pressure curve  $P_{\text{VEIN}}(t)$ , but above retinal interstitial pressure curve  $P_{\text{RET}}(t)$  (colored peaks in Fig. 2).

## 2.2. Total fluid volume leaking into the retina from M holes in N heartbeats

Equations are presented below for calculating the total volume of fluid leaking into the retina from a total of  $M$  holes in  $N$  heartbeats. With all holes in retinal blood vessels numbered from 1 to  $M$ , let  $i$  denote hole number  $i$  and  $j$  heartbeat  $j$ . In terms of  $i$  and  $j$ ,  $V_{\text{DROPLET}}^{\text{LEAK}}$  in Equations (9a and 9b) takes the form:

$$V_{\text{DROPLET}}^{\text{LEAK}}(i, j) = \frac{\pi D_i^4}{128\mu_i\ell_i} A_{\text{UPC}}^{i,j} = \frac{1}{8\pi} \frac{A_i^2}{\mu_i\ell_i} A_{\text{UPC}}^{i,j} \quad , \quad \text{for } P_{\text{VEIN}}^{i,j}(t) > P_{\text{RET}}^{i,j}(t) \quad (10)$$

Summing up individual contributions of  $V_{\text{DROPLET}}^{\text{LEAK}}$  from all  $M$  leaking holes, yielded the volume of fluid that leaks into the retina during a single heartbeat  $j$ :

$$V_{\text{1-BEATS}}^{\text{LEAK}}(j) = \sum_{i=1}^M V_{\text{DROPLET}}^{\text{LEAK}}(i, j) = \sum_{i=1}^M \frac{\pi D_i^4}{128\mu_i\ell_i} A_{\text{UPC}}^{i,j} = \sum_{i=1}^M \frac{1}{8\pi} \frac{A_i^2}{\mu_i\ell_i} A_{\text{UPC}}^{i,j} \quad , \quad \text{for } P_{\text{VEIN}}^{i,j}(t) > P_{\text{RET}}^{i,j}(t) \quad (11)$$

The total volume of fluid that leaks into the retina from  $M$  holes in  $N$  heartbeat is then:

$$\begin{aligned} V_{\text{N-BEATS}}^{\text{LEAK}} &= \sum_{j=1}^N V_{\text{1-BEAT}}^{\text{LEAK}}(j) = \sum_{j=1}^N \sum_{i=1}^M V_{\text{DROPLET}}^{\text{LEAK}}(i, j) = \sum_{j=1}^N \sum_{i=1}^M \frac{\pi D_i^4}{128\mu_i\ell_i} A_{\text{UPC}}^{i,j} = \\ &= \sum_{j=1}^N \sum_{i=1}^M \frac{1}{8\pi} \frac{A_i^2}{\mu_i\ell_i} A_{\text{UPC}}^{i,j} \quad , \quad \text{for } P_{\text{VEIN}}^{i,j}(t) > P_{\text{RET}}^{i,j}(t) \end{aligned} \quad (12)$$

Volumes of fluid leaking into the retina can also be expressed in terms of averages. The average volume of a fluid droplet leaking into the retina from M holes during N heartbeats is:

$$\bar{V}_{\text{DROPLET}}^{\text{LEAK}} = \frac{1}{NM} \sum_{j=1}^N \sum_{i=1}^M V_{\text{DROPLET}}^{\text{LEAK}}(i,j) \quad , \quad \text{for } P_{\text{VEIN}}^{ij}(t) > P_{\text{RET}}^{ij}(t) \quad (13)$$

Here, NM equals the total number of individual *episodes* of fluid droplet leakage into the retina. The double sum in Equation (13) equals the total volume of fluid leaking (not accumulating!) into the retina from M holes in N heartbeats, *i.e.*, in NM individual leaking episodes. Similarly, the average volume of fluid leaking into the retina from M holes in a single heartbeat is obtained from Equation (11):

$$\bar{V}_{\text{1-BEAT}}^{\text{LEAK}} = \frac{1}{N} \sum_{j=1}^N V_{\text{1-BEAT}}^{\text{LEAK}}(j) = \frac{1}{N} \sum_{j=1}^N \sum_{i=1}^M V_{\text{DROPLET}}^{\text{LEAK}}(i,j) \quad , \quad \text{for } P_{\text{VEIN}}^{ij}(t) > P_{\text{RET}}^{ij}(t) \quad (14)$$

Putting all this together, the total volume of fluid leaking into the retina from M holes in N heartbeats is:

$$V_{\text{N-BEATS}}^{\text{LEAK}} = N \bar{V}_{\text{1-BEAT}}^{\text{LEAK}} = NM \bar{V}_{\text{DROPLET}}^{\text{LEAK}} = \sum_{j=1}^N \sum_{i=1}^M V_{\text{DROPLET}}^{\text{LEAK}}(i,j) \quad , \quad \text{for } P_{\text{VEIN}}^{ij}(t) > P_{\text{RET}}^{ij}(t) \quad (15)$$

in which all three Equations (12, 13, 14) were used. Equations (1) to (15) will be called the ‘Retinal Fluid Volume Leakage’ (RFVL) Equations. The above leakage volumes were calculated from OCT-scans, obtained in five visits to the ophthalmologist, as follows.

### 2.3. Macular fluid accumulation, removal, and leakage

Three processes take place in DR or ADR. Fluid *leakage* from vein holes (‘leakage’), fluid *removal* from the retina by eye pumps (‘pumps’), and fluid *accumulation* in the retina (‘accumulation’). For retinal fluid: Volume accumulated = Volume leaked – Volume removed. A similar relation exists for *time-rates* of accumulation, leakage, and removal. Volume of accumulated fluid is known from two successive OCT-measured macular thicknesses. The *unique* case of *recovery* from ADR made it possible to calculate both the rate and volume of fluid removal from the retina by pumps. Leaked fluid volume is then simply the sum of volume accumulated plus volume removed (pumped out).

#### 2.3.1. Volume of fluid accumulated between OCT scans

Retinal thickness H varies from zone to zone in the retina, and so it is measured by OCT at K different retinal zones of interest. Let  $H_k$  denote average retinal thickness at zone k, then average retinal thickness is:

$$\bar{H} = \frac{1}{K} \sum_{k=1}^K H_k \quad (16)$$

The difference between two OCT measured retinal thicknesses, taken n-days apart, or N-heartbeats apart, is:

$$\Delta\bar{H}_n = \bar{H}_n - \bar{H}_0 \quad (17)$$

in which thickness  $\bar{H}_0$  is measured on day n = 0, and thickness  $\bar{H}_n$  on day n.  $\Delta\bar{H}_n$  represents excess fluid accumulated in the retina. The *volume* of accumulated fluid is obtained simply by multiplying  $\Delta\bar{H}_n$  with known retinal surface area S:

$$\bar{V}_{n\text{-days}}^{\text{ACUM}} = S\Delta\bar{H}_n = S(\bar{H}_n - \bar{H}_0) \quad (18)$$

Calculation of leaked and removed fluid volumes required prior knowledge of their time-rates of change.

### 2.3.2. Daily rates of fluid accumulation, leakage, and removal

The *daily rate* at which fluids *accumulate* in the retina,  $Q_{\text{ACUM}}$ , equals the difference between the daily rate of *fluid inflow*,  $Q_{\text{LEAK}}$  (leakage from small veins), and *fluid outflow*,  $Q_{\text{PUMP}}$  (removal by pumps), from the retina:

$$Q_{\text{ACUM}} = Q_{\text{LEAK}} - Q_{\text{PUMP}} \left\{ \begin{array}{ll} \text{Fluid accumulation in diabetics} & Q_{\text{ACUM}} > 0 \\ \text{Non diabetics} & Q_{\text{ACUM}} = 0 \\ \text{Fluid removal in recovering diabetics} & Q_{\text{ACUM}} < 0 \end{array} \right\} \quad (19a)$$

Dividing Equation (18) by n, yielded the average daily rate of fluid accumulation  $\bar{Q}_{\text{ACUM}}$ :

$$\bar{Q}_{\text{ACUM}} \approx \bar{Q}_{\text{ACUM}}^n = \bar{Q}_{\text{LEAK}}^n - \bar{Q}_{\text{PUMP}}^n = \frac{\bar{V}_{n\text{-days}}^{\text{ACUM}}}{n} = S \frac{\Delta\bar{H}_n}{n} = S \frac{\bar{H}_n - \bar{H}_0}{n} \quad (20a)$$

It required only two known measurements on the right side of Equation (20a) to estimate rate  $\bar{Q}_{\text{ACUM}}$ . The unique *case* of ‘*recovery*’ from ADR was used to estimate  $\bar{Q}_{\text{PUMP}}$ . Consider a diabetic patient recovering from ADR in a period of  $\tilde{n}$  days (squiggle denotes ‘recovery’). On day  $\tilde{n} = 0$  of recovery, measured retinal thickness was  $\bar{H}_{\tilde{0}}$ , and  $\tilde{n}$  days later it was back to normal at  $\bar{H}_{\infty}$ . The rate of fluid leakage into the retina was approximately *zero* during recovery, and so the eye’s pumps reduced retinal thickness from  $\bar{H}_{\tilde{0}}$  to  $\bar{H}_{\infty}$  in  $\tilde{n}$  days, and we can write:

$$n = \tilde{n}, \quad \bar{Q}_{\text{LEAK}}^{\tilde{n}} = 0, \quad \bar{H}_0 = \bar{H}_{\tilde{0}}, \quad \bar{H}_n = \bar{H}_{\infty} \quad (20b)$$

Substituting conditions (20b) into Equation (20a) yielded the formula for estimating average pumping rate  $\bar{Q}_{\text{PUMP}}$ :

$$\bar{Q}_{\text{PUMP}} \approx \bar{Q}_{\text{PUMP}}^{\tilde{n}} = -S \frac{\bar{H}_{\infty} - \bar{H}_{\tilde{0}}}{\tilde{n}} = S \frac{\bar{H}_{\tilde{0}} - \bar{H}_{\infty}}{\tilde{n}} > 0 \quad (20c)$$

Only two measurements,  $\bar{H}_0$  and  $\bar{H}_\infty$ , are needed to estimate  $\bar{Q}_{PUMP}$ . Note that  $\bar{H}_0$  and  $\tilde{n}$  are linked. The larger the starting value  $\bar{H}_0$  is, the longer the  $\tilde{n}$ -days recovery time to normal  $\bar{H}_\infty$  will be. Finally, inserting Equation (20c) into Equation (20a) yielded the formula for estimating  $\bar{Q}_{LEAK}$ , the average daily rate of fluid volume leakage into the retina:

$$\bar{Q}_{LEAK} \approx \bar{Q}_{LEAK}^n = \bar{Q}_{ACUM}^n + \bar{Q}_{PUMP}^{\tilde{n}} = S \frac{\bar{H}_n - \bar{H}_0}{n} + S \frac{\bar{H}_0 - \bar{H}_\infty}{\tilde{n}} \quad (20d)$$

Four OCT-measurements,  $\bar{H}_0$ ,  $\bar{H}_n$ ,  $\bar{H}_0$ ,  $\bar{H}_\infty$ , were required to estimate  $\bar{Q}_{LEAK}$  from Equation (20d).

The three rate equations (Eqs. 20 a, c, and d) apply to the whole retina, but were modified for use in the smaller macular region because OCT scans are confined to a macular area of  $S_m = 28.274 \text{ mm}^2$  within diameter  $D_m = 6 \text{ mm}$  (see Introduction). So macular  $\bar{Q}_{ACUM}$ ,  $\bar{Q}_{PUMP}$ ,  $\bar{Q}_{LEAK}$  were calculated from macular data as follows:

$$\bar{Q}_{ACUM} \approx \bar{Q}_{ACUM}^n = S_m \frac{\bar{H}_n - \bar{H}_0}{n}, \quad S_m = 28.274 \text{ mm}^2 \quad (21a)$$

$$\bar{Q}_{PUMP} = \bar{Q}_{PUMP}^{\tilde{n}} = S_m \frac{\bar{H}_0 - \bar{H}_\infty}{\tilde{n}}, \quad \bar{H}_\infty = \text{normal thickness on day } \tilde{n} \quad (21b)$$

$$\bar{Q}_{LEAK} = \bar{Q}_{ACUM} + \bar{Q}_{PUMP} \approx \bar{Q}_{LEAK}^n = S_m \frac{\bar{H}_n - \bar{H}_0}{n} + S_m \frac{\bar{H}_0 - \bar{H}_\infty}{\tilde{n}} \quad (21c)$$

### 2.3.3. Volumes of fluid removed and leaked between OCT scans

Multiplying  $\bar{Q}_{PUMP}$ ,  $\bar{Q}_{LEAK}$  in Equations (21b,c) by  $n$ , yielded macular fluid volumes removed by pumps and leaked from vein holes in the  $n$ -days period between successive scans, respectively:

$$\bar{V}_{PUMP}^{n\text{-days}} = n\bar{Q}_{PUMP}^{\tilde{n}} = \frac{n}{\tilde{n}} S_m (\bar{H}_0 - \bar{H}_\infty), \quad \bar{H}_\infty = \text{normal thickness on day } \tilde{n} \quad (22a)$$

$$\bar{V}_{LEAK}^{n\text{-days}} = n\bar{Q}_{LEAK}^n = S_m (\bar{H}_n - \bar{H}_0) + \frac{n}{\tilde{n}} S_m (\bar{H}_0 - \bar{H}_\infty), \quad \bar{H}_\infty = \text{normal thickness on day } \tilde{n} \quad (22b)$$

### 2.3.4. Volumes of fluid leaked in N-heartbeats, in 1-heartbeat, and in 1 droplet

At an average heart rate of  $f$  beats per minute (bpm) (e.g., 78 bpm = 1.3 Hz), the heart beats  $N$  times in  $n$ -days:

$$N = 60 \cdot 24 \cdot n \cdot f = 1440 \cdot n \cdot f \quad (22c)$$

Since the volumes of fluid leaked in  $n$ -days and in  $N$ -heartbeats are equal, Equation (22b) can be rewritten as:

$$\bar{V}_{N\text{-BEATS}}^{\text{LEAK}} = \bar{V}_{\text{LEAK}}^{\text{n-days}} = S_m(\bar{H}_n - \bar{H}_0) + \frac{n}{\bar{n}} S_m(\bar{H}_0 - \bar{H}_\infty), \quad \bar{H}_\infty = \text{normal thickness on day } \bar{n} \quad (22d)$$

Inserting Equation (22d) into RFVL Equation (15) yielded:

$$\bar{V}_{N\text{-BEATS}}^{\text{LEAK}} = N \bar{V}_{1\text{-BEAT}}^{\text{LEAK}} = NM \bar{V}_{\text{DROPLET}}^{\text{LEAK}} = S_m(\bar{H}_n - \bar{H}_0) + \frac{n}{\bar{n}} S_m(\bar{H}_0 - \bar{H}_\infty), \quad \bar{H}_\infty = \text{normal thickness on day } \bar{n} \quad (22e)$$

Finally, rearranging Equation (22e) yielded three separate equations (Eqs. 23a, b, and c) for calculating leaked macular fluid volume in N-heartbeats, in 1-heartbeat, and in 1 droplet from OCT-measured macular thicknesses:

$$\bar{V}_{N\text{-BEATS}}^{\text{LEAK}} = S_m(\bar{H}_n - \bar{H}_0) + \frac{n}{\bar{n}} S_m(\bar{H}_0 - \bar{H}_\infty), \quad \bar{H}_\infty = \text{normal thickness on day } \bar{n} \quad (23a)$$

$$\bar{V}_{1\text{-BEAT}}^{\text{LEAK}} = M \bar{V}_{\text{DROPLET}}^{\text{LEAK}} = \frac{S_m}{N}(\bar{H}_n - \bar{H}_0) + \frac{n}{\bar{n}} \frac{S_m}{N}(\bar{H}_0 - \bar{H}_\infty), \quad \bar{H}_\infty = \text{normal thickness on day } \bar{n} \quad (23b)$$

$$\bar{V}_{\text{DROPLET}}^{\text{LEAK}} = \frac{S_m}{NM}(\bar{H}_n - \bar{H}_0) + \frac{n}{\bar{n}} \frac{S_m}{NM}(\bar{H}_0 - \bar{H}_\infty), \quad \bar{H}_\infty = \text{normal thickness on day } \bar{n} \quad (23c)$$

Fluid volumes leaked in N-beats and in 1-beat were readily calculated from the known right sides of (23a,b). But M on the right side of Equation (23c) is not yet known, and so  $\bar{V}_{\text{DROPLET}}^{\text{LEAK}}$  could not be calculated. It could, however, be calculated once M becomes known in the future. Meanwhile, the *important product*  $M\bar{V}_{\text{DROPLET}}^{\text{LEAK}}$  was computed from the known right side of Equation (23b).

#### 2.4. Parameters in RFVL equations that control RS in ADR

From RFVL Equations (9), the volume of a single leaked droplet,  $V_{\text{DROPLET}}$ , is tightly controlled by D or A,  $\mu$ ,  $\ell$ , and  $A_{\text{UPC}}$ . In particular,  $V_{\text{DROPLET}}$  is very sensitive to diameter D, or area A. It grows with D to the power of 4, or A to the power of 2. So, remedies are clearly needed to reduce D or A. Furthermore, let  $N = N_{\text{RS}}$  be the number of heartbeats occurring when significant ADR-induced RS exists. Then RFVL Equations (12) and (15) show that  $N_{\text{RS}}$  and M also tightly control RS, because the *total* volume of fluid leaking into retina depends on both M (number of holes) and  $N = N_{\text{RS}}$ . The larger M and  $N_{\text{RS}}$  are, the larger excess fluid accumulation in the retina will be. Hence, in ADR, the list of clinically significant parameters identified with the RFVL equations includes:

1. D = Diameter of microscopic abnormal hole in a blood vessel's wall;
2.  $A = \frac{1}{4}\pi D^2$  = Cross-sectional area of a microscopic hole in a blood vessel's wall;
3.  $\mu$  = Blood or fluid dynamic viscosity;
4.  $\ell$  = Length of abnormal hole, or thickness of blood vessel's wall (Figs. 1 and 3);
5.  $A_{\text{UPC}}$  = Area under vein pressure curve  $P_{\text{VEIN}}(t)$ , but above pressure curve  $P_{\text{RET}}$

(t) (colored peaks in Fig. 2);

6.  $M$  = Total number of abnormal holes in vessels of the retinal micro-circulation; and

7.  $N_{RS}$  = Number of heartbeats in an ADR period when significant RS exists.

The RFVL equations indicate that fluid leakage into the retina will *decrease* when:

1.  $A_{UPC}$  is *decreased* as a result of a *decrease* in transmural pressure  $P_{VEIN} - P_{RET}$ ;
2. hole diameter  $D$ , or area  $A$ , is *decreased*;
3. blood or fluid viscosity  $\mu$  is *increased*;
4. length of hole  $\ell$  is *increased*;
5. total number  $M$  of leaking holes in retinal blood vessels is *decreased*; and
6. number of heartbeats  $N_{RS}$  during significant RS is *decreased*.

Note that hole length  $\ell$  is fixed and cannot be increased.

## 2.5. Five simple therapeutic treatments that induce recovery from ADR

During RS,  $\bar{Q}_{LEAK} > \bar{Q}_{PUMP}$  and so fluid accumulates in the retina. It is very difficult to reduce leakage from damaged blood vessels to *zero* in diabetics. However, this does actually occur, as was mentioned earlier. In general, it is not necessary to aim for  $\bar{Q}_{LEAK} = 0$ . Instead, to reduce swelling, it is sufficient to reduce leakage to levels where  $\bar{Q}_{LEAK} < \bar{Q}_{PUMP}$ . With reduced leakage rates below  $\bar{Q}_{PUMP}$ , the eye's pumps take control again and remove excess accumulated fluids until swelling disappears, and retinal thickness is restored to normal. Insights gained from the ADR model were used to design the following five simple therapeutic treatments T1 to T5 for recovery from ADR. Primary author AH applied T1-T5 to treat his ADR, with successful and beneficial outcome.

T1. Use of efficient anti-hypertensive drugs to reduce blood pressure. This can significantly *diminish* the leakage rate from vein holes due to reduced transmural pressure  $P_{VEIN} - P_{RET}$  and so reduced  $A_{UPC}$  (Fig. 2).

T2. Increase thiamine intake to a high dose of 300 mg per day so that vitamin B1 levels become normal again.<sup>20,21</sup> This is expected to help restore retinal veins to good health, 'repair' vein holes, and reduce hole diameter  $D$  or area  $A$  (see explanatory note below). Ensuring good diabetes control with other medications is also of great importance.

T3. Increase daily vitamin D intake if blood plasma levels are low.

T4. Stop intake of blood thinners such as aspirin (if permissible). This increases blood viscosity and reduces the rate of fluid leakage from holes in retinal blood vessels.

T5. Reduce daily consumption of cups of coffee.

### 2.5.1. Explanatory notes on T1-T5

**Treatment T1:** In hypertensive diabetics suffering from ADR, *efficient* anti-hypertensive drug therapy can cause both arterial and venous temporal blood pressure

fluctuations to drop to almost normal levels. Inserting a much-downsized oscillatory pressure  $P_{\text{VEIN}}(t)$  into Equations (9) results in greatly diminished  $A_{\text{UPC}}$  and in much-reduced fluid leakages into the retina. Leakage could even come to a complete halt when  $A_{\text{UPC}}$  is zero or very close to zero.

**Treatment T2:** Thiamine (vitamin B1) is an essential co-factor involved in cellular metabolism. It plays a fundamental role in intracellular *glucose* metabolism.<sup>22</sup> Given that humans cannot synthesize thiamine, a regular intake of thiamine from external sources (yeasts and plants) is needed to maintain normal body storage levels. The average daily nutritional intake of vitamin B1 is only 1 mg. In diabetics, thiamine's various roles can prevent toxic cellular changes induced by hyperglycemia (high glucose levels) from taking place.<sup>22</sup> Several studies have shown that type 1 and 2 diabetics suffer from thiamine deficiency.<sup>20,24,23</sup> Lack of thiamine can cause a number of severe vascular disorders that result in, for example, retina, kidney, and nerve damage, as well as heart disease and stroke. In the thiamine-deficient state, glucose undergoes metabolism via alternate pathways (that are not thiamine-dependent), leading to formation of *harmful by-products* that can damage blood vessels and induce ADR. In addition, thiamine has direct action on the insulin-secreting function of the pancreas, and therefore, thiamine deficiency may contribute to hyperglycemia through mechanisms other than impaired glucose metabolism. *Thiamine supplementation can counteract the damaging effects of hyperglycemia on retinal blood vessels.* It does this by preventing formation of harmful by-products produced by glucose metabolism via alternate thiamine-independent pathways, as well as by restoring pancreatic function to normal. Supplementation of thiamine analogues in animal models of diabetes has, indeed, been shown to prevent DR disease progression.<sup>25,26</sup>

Hence, supplementary thiamine is key to warding off retinal vascular problems and ADR. In human diabetics, the simple link between thiamine deficiency and diabetes complications was demonstrated by Thornalley and his team.<sup>20,23</sup> They measured thiamine levels in blood plasma and found that concentrations were 76% lower than normal in type 1 diabetics and 75% lower in type 2 diabetics. They also found that type 1 and 2 diabetics expelled thiamine from their bodies at 15 times the normal rate. To keep blood vessels in good health, diabetics with low vitamin B1 levels clearly need additional thiamine intake to return vitamin B1 levels to normal. Since daily nutritional intake of vitamin B1 is only 1 mg, changes to diet would not be enough to have an effect. Accordingly, Thornalley successfully treated his diabetic patients with a high-dose of 300 mg vitamin B1 daily.<sup>20,21</sup>

**Treatment T3:** The relationship between vitamin D deficiency (VDD) and DR has most recently (October 2016) been reviewed.<sup>27</sup> Evidence is strongly suggestive that significant VDD is present in both type 1 and 2 diabetics, compared to non-diabetics, and of a *link between VDD and the severity of DR*.<sup>28</sup> VDD has also been associated with increased odds of age-related macular degeneration,<sup>29</sup> which is the most

common cause of blindness in the elderly. Since vitamin D plays many important and beneficial roles in our eyes and bodies,<sup>30</sup> it was expected that a substantial vitamin D intake (below toxic levels) may help ‘repair’ and reduce diameter D and area A of holes in retinal veins.

**Treatment T4:** Aspirin is an antiplatelet drug (anti-aggregant) that decreases platelet aggregation and inhibits thrombus formation. Aspirin is *widely used* in primary and secondary prevention of thrombotic cardiovascular disease, and has demonstrated mortality benefit in prevention of cardiovascular death in specific populations. The American Heart Association (AHA) recommends that people at high risk of heart attack should take a daily low-dose of aspirin, and that heart attack survivors regularly take low-dose aspirin. Many individuals follow the AHA’s advice, and even individuals at *no risk* of heart attack also take daily low-dose aspirin as a preventive measure. The blood-thinning effects of aspirin have traditionally been ascribed to antiplatelet mechanisms. *Aspirin has more recently been demonstrated to lower blood viscosity.* Though various mechanisms have been proposed, aspirin-induced changes to the erythrocyte cell membrane were shown to decrease red blood cell rigidity, and to decrease whole blood viscosity.<sup>31</sup> In 2008, Vekasi<sup>32</sup> demonstrated a relationship between aspirin use and lowered blood viscosity in patients with DR. So, stopping aspirin intake leads to an increase in blood viscosity  $\mu$ , which in turn, reduces the rate of fluid leakage  $Q(t)$  from vein holes into the retina. The reduced leakage rate is due to the inverse relationship between  $Q(t)$  and  $\mu$ , defined in Equations (8). The higher the viscosity, the lesser the rate (and volume) of fluid leaking into the retina from holes in damaged veins. A simple intuitive example illustrates the effect that viscosity has on leakage flow. Compare a short-duration burst of low-viscosity water flowing from the end of a garden hose with a short burst of viscous oil flowing from the end of the same hose. A small amount of oil will land next to your feet, while a much larger volume of water will land a few meters further away. The higher the viscosity, the lesser the volume of fluid ejected from the end of the hose will be.

**Treatment T5:** Caffeine can cause a short, but dramatic, increase in blood pressure, even in subjects with normal blood pressure. It is unclear what causes this spike in blood pressure (Mayo Clinic).<sup>34</sup> Being a mathematician, AH consumed between 10 to 15 cups of coffee daily. This has been reduced to only 2-3 cups daily, with long-term beneficial effects.

### 3. Results

Primary author AH has had type 2 diabetes for 43 years, and in the distant past suffered from ADR. He successfully treated his ADR with T1-T5, and has now been free of ADR for over ten years. From mid-2004 (13.5 years ago), AH’s retinas

continued swelling despite laser treatments, eventually reaching 477 microns by June 28, 2007. As laser therapy had become ineffective, and offers of intra-vitreous Avastin injections were most unappealing, AH turned to mathematics, rather than medicine, to find new effective treatments for his ADR and impaired (blurred) vision. With a sense of great urgency attributed to fear of fast-approaching blindness, and while still being able to see modestly well, AH derived the above mathematical model of ADR and treatments T1-T5 ten years ago. (Writing of this paper also started ten years ago.) *Simultaneous* application of treatments T1-T5 started at the end of June 2007. Remarkably, after only 42 days, AH's retinal thickness returned to normal and stayed normal ever since, without Avastin injections. Noteworthy was some detectable vision improvement 11 days after initiation of T1-T5. Treatments T1-T5 have clearly diminished fluid leakage in AH's retinas, and achieved a long-lasting recovery from ADR. It is not possible to select the most effective of T1-T5. All of them have probably combined to reduce retinal thickness to normal and keep it normal up to this day.

### 3.1. Advancing DR and recovery from ADR

Table 2 summarizes results of calculations with fluid leakage equations derived earlier. Calculations were based on five OCT thicknesses, measured on five visits to the ophthalmologist. DR advanced to unmanageable levels between Visits 1 and 4, while recovery from ADR occurred between Visits 4 and 5. Rows 1 and 2 in Table 2 list OCT scan number (visit number) and date, respectively. Row 3 lists  $n$  (number of days between two successive scans) and  $\tilde{n}$  (number of days needed to recover from ADR). Measured macular thicknesses are tabulated in row 4, and corresponding macular volumes in row 6. On Visit 1, macular volume was  $7.590 \text{ mm}^3$  and on Visit 4 it was  $13.487 \text{ mm}^3$ , but on Visit 5 it was almost normal at  $7.04 \text{ mm}^3$ . *Accumulated* fluid volumes, calculated from Equation (18) with  $S = S_m$ , are listed in row 7. Dividing them by  $n$  or  $\tilde{n}$  yielded  $\bar{Q}_{ACUM}$ , the average daily *rates* of fluid volume accumulation in the macula (row 8). Between Scans 2 and 3,  $\bar{Q}_{ACUM}$  was  $44.01 \times 10^{-4} \text{ mm}^3/\text{day}$ . But between Scans 3 and 4,  $\bar{Q}_{ACUM}$  had a huge jump to  $848.22 \times 10^{-4} \text{ mm}^3/\text{day}$  (a 19-fold hike) in only 28 days. Happily, between Scans 4 and 5,  $\bar{Q}_{ACUM}$  became negative at  $-1534.87 \times 10^{-4} \text{ mm}^3/\text{day}$  due to the pumps regaining control and removing fluids from a macula in recovery from ADR. The rate of fluid volume removal by pumps (pumping rate) was found to be high:  $\bar{Q}_{PUMP} = 1534.87 \times 10^{-4} \text{ mm}^3/\text{day}$ ; calculated from Equation (21b) with  $\bar{H}_\infty = 0.249 \text{ mm}$ . This reveals a previously 'hidden' capacity of eye pumps to clear macular fluids at very substantial rates (discussed in more depth in the next section).

Under 'emergency' conditions prevailing in ADR, the eye's pumping apparatus operates at, or close, to full capacity. *It was therefore assumed that, in ADR, pumping rate is constant and about maximal, with magnitude dictated by pathological conditions prevailing in ADR.* This rate was then applied in previous four inter-scans periods (row 9).

*Leakage rates*,  $\bar{Q}_{LEAK}$ , were calculated with Equation (21c) and tabulated in row 10. Between Scans 1 and 2 and between 2 and 3,  $\bar{Q}_{LEAK}$  and  $\bar{Q}_{PUMP}$  were almost identical, and so a modest volume of fluid accumulated in the macula in these periods. A large increase in leakage rate to 0.23831 mm<sup>3</sup>/day (51% higher than the previous rate) occurred between Scans 3 and 4. Its significance is analyzed in the next subsection. Actual *volumes* (mm<sup>3</sup>) of removed fluid and leaked fluid for all inter-scan periods are tabulated in rows 11 and 12, respectively. Expressing these volumes in multiples of  $\bar{V}_{m\infty} = 6.76$  mm<sup>3</sup> (rows 13, 14), showed that the volume of fluid leaked in 28 days between Scans 3 and 4 was 1.0  $\bar{V}_{m\infty}$ , while fluid volume removed in 42 days of recovery from ADR (inter-scans 4-5) was also 1.0  $\bar{V}_{m\infty}$ . Thus, *fluid volumes equivalent to the volume of an entire macula were leaked and removed in two brief and crucial inter-scan periods!*

Finally, at an average heart rate of 78 bpm (1.3 Hz), the number of heartbeats N in each inter-scan period is listed in row 16. Inserting N into Equation (23b) yielded the important product  $M \bar{V}_{DROPLET}^{LEAK} = \bar{V}_{1-BEAT}^{LEAK}$  for all inter-scan periods (row 17). Between Scans 1 and 3, leaked  $M \bar{V}_{DROPLET}^{LEAK}$  averaged 1.385 mm<sup>3</sup> x 10<sup>-6</sup>. But in the next 28 days (inter-scans 3-4), it grew by a hefty 53.2% to 2.122 mm<sup>3</sup> x 10<sup>-6</sup>, and then dropped to zero in the 42 days of recovery from ADR. The significance of the large rise and large fall in  $M \bar{V}_{DROPLET}^{LEAK}$  is explained in the next two subsections.

### 3.2. Profound effect of small changes in hole diameter on fluid leakage

Because of *shortness* of inter-scan period 3-4 (only 28 days), it is unlikely that M (number of holes) had risen sharply in this short period. Hence, the large rise in product  $M \bar{V}_{DROPLET}^{LEAK}$  was likely due to a large increase in leaked droplet volume,  $\bar{V}_{DROPLET}^{LEAK}$ , and not due to M. Two parameters in  $\bar{V}_{DROPLET}^{LEAK}$  Equations (9) and (10) could have varied sharply in a short time; diameter D and area under the pressure curve  $A_{UPC}$ . Since AH's medications were inefficient in controlling his hypertension for more than a year, his already large  $A_{UPC}$  was not likely to explain the large rise in  $\bar{V}_{DROPLET}^{LEAK}$ . An increase in hole diameter D is then the likely cause for the large rise in  $\bar{V}_{DROPLET}^{LEAK}$ , as explained below.

For a fixed number of holes M, from smallest to largest, let the diameter of each hole be expanded ( $\varphi > 0$ ) or contracted ( $\varphi < 0$ ) by a factor  $\varphi$ . Then we can write:

$$\frac{D_i^\varphi}{D_i} = \varphi \quad \text{for } i = 1, 2, 3, \dots, M \quad (24a)$$

where  $D_i$  is the original hole diameter, and  $D_i^\varphi$  is the enlarged or contracted diameter of hole i. It is assumed that no other changes take place. Substituting Equation (24a) into Equations (10) and (13) shows that mean leaked droplet volume increases or decreases by a factor of  $\varphi^4$  to give:

$$\frac{\bar{V}_{DROPLET}^{LEAK-\varphi}}{\bar{V}_{DROPLET}^{LEAK}} = \varphi^4 \quad (24b)$$

Table 2. Results of calculations with ADR model

Macular parameter	Symbols and equations		ADR	
	Symbol or formula	Equation and/or Equation number	OCT scan	Inter-scan parameters
OCT scan or visit number			1	
Date of scan			05-Nov-04	
Number of inter-scans days	$n$ or $\hat{n}$			$n = 130$
Macular thickness (mm)	$\bar{H}$		0.268	
Macular surface area (mm <sup>2</sup> )	$S = S_m$		28.274	
Macular volume (mm <sup>3</sup> )	$\bar{V}_m$	$S_m \bar{H}$	7.590	
Volume of fluid <i>Accumulated</i> between scans (mm <sup>3</sup> )	$\bar{V}_{n\text{-days}}^{\text{ACUM}}$	Eq. (18)		-0.03
Rate of fluid volume <i>Accumulation</i> (10 <sup>4</sup> x mm <sup>3</sup> /day)	$\bar{Q}_{\text{ACUM}}$	Eq. (21a) $\frac{1}{n} \bar{V}_{n\text{-days}}^{\text{ACUM}}$		-2.31
Rate of fluid volume <i>Removal</i> (10 <sup>4</sup> x mm <sup>3</sup> /day)	$\bar{Q}_{\text{PUMP}}$	Eq. (21b)		1534.87
Rate of fluid volume <i>Leakage</i> (10 <sup>4</sup> x mm <sup>3</sup> /day)	$\bar{Q}_{\text{LEAK}}$	Eq. (21c) $\bar{Q}_{\text{ACUM}} + \bar{Q}_{\text{PUMP}}$		1532.57
Volume of fluid <i>Removed</i> between scans (mm <sup>3</sup> )	$\bar{V}_{n\text{-days}}^{\text{PUMP}}$	$n \bar{Q}_{\text{PUMP}}$		19.95
Volume of fluid <i>Leaked</i> between scans (mm <sup>3</sup> )	$\bar{V}_{n\text{-days}}^{\text{LEAK}}$	$n \bar{Q}_{\text{LEAK}}$		19.92
Volume of fluid <i>Removed</i> in multiples of $\bar{V}_{m\infty}$	$\bar{V}_{n\text{-days}}^{\text{PUMP}} / \bar{V}_{m\infty}$			3.0
Volume of fluid <i>Leaked</i> in multiples of $\bar{V}_{m\infty}$	$\bar{V}_{n\text{-days}}^{\text{LEAK}} / \bar{V}_{m\infty}$			2.9
Average heart rate (bpm)	$f$			78
Number of heartbeats between successive scans	$N$	$60 \cdot 24 \cdot n \cdot f$		14,601,600
$M\bar{V}_{\text{DROPLET}} = \bar{V}_{1\text{-BEAT}}^{\text{LEAK}}$ product in mm <sup>3</sup> x 10 <sup>6</sup>	$n \bar{Q}_{\text{LEAK}} / N$	Eq. (23b)		1.364

$\bar{V}_{m\infty} = 6.76 \text{ mm}^3$  = mean macular volume in normal subjects; ADR = advanced diabetic retinopathy;  $\hat{n} = 42$  = number of days in recovery from ADR (inter-scans 4-5)

ADR				Recovery from ADR		
OCT scan	Inter-scan parameters	OCT scan	Inter-scan params	OCT scan	Inter-scan parameters	OCT scan
2		3		4		5
15-Mar-05		31-May-07		28-Jun-07		09-Aug-07
	n = 807		n = 28		$\tilde{n} = 42$	
0.267		0.393		0.477		0.249
28.274		28.274		28.274		28.274
7.560		11.112		13.487		7.040
	3.55		2.38		-6.45	
	44.01		848.22		-1534.87	
	1534.87		1534.87		1534.87	
	1578.89		2383.09		0.00	
	123.86		4.30		6.45	
	127.42		6.67		0.00	
	18.3		0.6		1.0	
	18.8		1.0		0.0	
	78		78		78	
	90,642,240		3,144,960		4,717,440	
	1.406		2.122		0.0	

$M\bar{V}_{\text{DROPLET}}^{\text{LEAK}}$  was  $1.406 \cdot 10^{-6} \text{ mm}^3$  and  $2.122 \cdot 10^{-6} \text{ mm}^3$  in inter-scan periods 2-3 and 3-4 (Table 2). Dividing them gives:

$$\frac{\bar{V}_{\text{1-BEATS}}^{\text{LEAK-}\varphi}}{\bar{V}_{\text{1-BEATS}}^{\text{LEAK}}} = \frac{M\bar{V}_{\text{DROPLET}}^{\text{LEAK-}\varphi}}{M\bar{V}_{\text{DROPLET}}^{\text{LEAK}}} = \frac{\bar{V}_{\text{DROPLET}}^{\text{LEAK-}\varphi}}{\bar{V}_{\text{DROPLET}}^{\text{LEAK}}} = \frac{2.122 \times 10^{-6}}{1.406 \times 10^{-6}} = 1.5092 = \varphi^4, \quad \varphi = 1.1084 \quad (24c)$$

Thus, a mere 10.84% increase in the diameters of all holes ( $\varphi = 1.1084$ ) produced an impressive 50.9% increase in mean leaked droplet volume. This exposes the profound effect that *small* increases in hole diameters  $D$  have on volume of leaked fluid droplets in ADR. This may also explain AH's vision problems in the inter-scan period 3-4. Often, large leakages originate from a few large micro-aneurysms. The above analysis applies to them as well, because *mean* leaked droplet volume is calculated from a distribution of hole diameters, ranging from 'small-leaking', small-diameter holes to 'big-leaking', large-diameter holes. They all had their diameter enlarged by a factor  $\varphi$ .

Diameter contraction ( $\varphi < 1$ ) probably takes place during recovery from ADR. A modest -8.5% reduction in all diameters  $D$  ( $\varphi = 0.915$ ) will result in a large -30.0% ( $0.915^4 - 1$ ) reduction in fluid leakage into the macula. This is both impressive and clinically significant. *It means that shrinkage in hole diameters may only need to be small, or modest, to be highly effective in reducing ADR swelling.* In AH's case, it is possible that treatments T2 (vitamin B1) and T3 (vitamin D) induced small 'repairs' in AH's retinal blood vessels, resulting in modest 'shrinking' of hole diameters, and in sustained recovery from ADR.

Table 3 lists  $\varphi^4 - 1$  values (relative increase or decrease in leakage volume) for a range of expansion and contraction factors  $\varphi$ . In ADR, small to modest increases of 2.4%, 5.7%, 10.7%, 15%, and 19% in hole diameters induce impressive 10%, 25%, 50%, 75%, 100% (volume-doubling) increases in leakage-volumes, respectively. In recovery from ADR, small to modest decreases of -2.6%, -5.4%, -8.5%, -12%, and -15.9% in hole diameters induce equally impressive -10%, -20%, -30%, -40%, and -50% decreases in leakage volumes, respectively. The -50% decrease constitutes an awe-inspiring halving in fluid leakage during recovery from ADR. Since it takes time for the eyes to 'repair' and restore blood vessels to good health, hole 'shrinkage' is probably not a fast process.

### 3.3. Reducing RS in ADR with efficient anti-hypertensive drugs

AH's blurred vision improved slightly, but noticeably, after only 11 days on more efficient anti-hypertensive drugs. In the recovery from ADR period, only parameter  $A_{\text{UPC}}$  in droplet volume Equations (9) and (10) could respond in just 11 days. When  $A_{\text{UPC}}$  becomes zero due to the action of efficient drugs, the pressure force driving fluids through holes vanishes, and leakage flow soon comes to a halt. Thus, in the first 11 days of recovery, the pumps probably succeeded in partially reducing AH's macular volume, which explains his slight but noticeable vision improvement. It is tempting to speculate that all that needs to be done to achieve recovery from ADR

Table 3. Large changes in volume of fluid leaking into the macula in response to small changes in diameters of holes in macular blood vessels

Macula parameter	Equation	◀ Recovery from DR or ADR					Advancing DR ▶				
Hole diameter expansion or contraction factor	$\frac{D_i^\phi}{D_i} = \phi$	0.841	0.880	0.915	0.946	0.974	1.024	1.057	1.107	1.150	1.190
Relative volume of fluid leaking into the macula	$\phi^4$	0.500	0.600	0.701	0.801	0.900	1.100	1.248	1.502	1.749	2.005
Relative increase or decrease in hole diameter	$\phi - 1$	-15.9%	-12.0%	-8.5%	-5.4%	-2.6%	2.4%	5.7%	10.7%	15.0%	19.0%
Relative increase or decrease in volume of fluid leaking into the macula.	$\phi^4 - 1$	-50.0%	-40.0%	-29.9%	-19.9%	-10.0%	10.0%	24.8%	50.2%	74.9%	100.5%

$D_i$  = original hole diameter;  $D_i^\phi$  = expanded or contracted hole diameter;  $i = 1,2,3,\dots,M$ ;  $M$  = number of holes in macular blood vessels

is to efficiently control BP. Sadly, this is only helpful in reducing macular swelling for about four to five years, but not in halting progression of ADR and further damage to retinal blood vessels.<sup>33</sup> Additional treatments to T1, e.g., T2 to T5, may help ‘repair’ damaged vessels and sustain ADR recovery.

## 4. Discussion and conclusions

This paper asserts usefulness of mathematics in finding new ways of avoiding blindness in diabetics. A mathematical model of ADR, based on fluid leakage from retinal micro-vessels, was used to design five alternative treatments, T1-T5, to recover from ADR. AH treated his ADR with T1-T5, with very successful and beneficial outcome; he recovered from ADR in six weeks, and has been free of ADR for over ten years. *Treatments T1-T5 are not a proven ‘cure’ for ADR, because they are based on a*

single patient application of T1-T5. However, successful and ‘fruitful’ single reports are often the basis for initiating medical trials based on numerous observations. It is, therefore, hoped that future clinical trials will confirm that treatments T1-T5 can achieve sustained recovery from ADR.

Progression of AH’s ADR was halted because all five treatments T1 to T5 were applied *simultaneously*. Applying T1 alone (efficient BP control) is not sufficient to achieve a durable outcome since benefits last for only four to five years.<sup>33</sup> Treatments T2-T5 must be applied together with T1 to achieve long-lasting freedom from DR or ADR.

The unique case of recovery from ADR allowed calculation of the hitherto ‘hidden’ and unknown pumping rate  $\bar{Q}_{\text{PUMP}}$ . During recovery, leakage rates are almost zero, and so the rate of macular volume ‘shrinkage’ is solely determined by  $\bar{Q}_{\text{PUMP}}$ . This rate is colossal;  $\bar{Q}_{\text{PUMP}} = 0.1535 \text{ mm}^3/\text{day}$ . At this rate, eye pumps can remove an entire normal macula-volume-equivalent in 44 days ( $6.76 \text{ mm}^3 / 0.1535 \text{ mm}^3/\text{day}$ ). This actually happened during AH’s recovery from ADR; a volume of  $6.45 \text{ mm}^3$  (close to  $1.0 \bar{V}_{\text{m}\infty}$ ) was cleared in 42 days (row 13 in Table 2). By any measure, this is a very large fluid volume for such microscopic pumps.  $\bar{Q}_{\text{PUMP}}$  can vary, of course, from one diabetic subject to another. In mild DR, eye pumps can easily remove average-sized leakages from the macula. In severe ADR, pumps get overpowered by leakage rates markedly higher than  $\bar{Q}_{\text{PUMP}}$ , and so significant macular swelling occurs. To reduce swelling and recover from ADR, all that needs to be done is reduce leakage rates to *below*  $\bar{Q}_{\text{PUMP}}$ . This applies to all diabetics, each with its own  $\bar{Q}_{\text{PUMP}}$ .

The actual volume of fluid that leaked ( $n\bar{Q}_{\text{LEAK}}$ ) in the *short* 28 days period of severe ADR was huge:  $1.0 \bar{V}_{\text{m}\infty}$  (inter-scans 3-4, row 14). Thus, in severe ADR and also in recovery from ADR, whole macula-volume-equivalents were leaked then removed (see above) in two successive, short, and crucial inter-scan periods.

At present, M (total number of holes in retinal blood vessels) is not known. But when it is finally measured in the future, it may serve as a useful index in clinical assessment of progression or recovery from DR or ADR.

Finally, leakage volumes are very sensitive to small changes in hole-diameters. A small 5.7% increase, or a -5.4% decrease, in hole diameter results in a sizeable 25% increase or a -20% decrease in leakage volumes, respectively. A modest 19% increase, or a -15.9% decrease, results in massive doubling or halving of leakage volumes, respectively (Table 3). With such sensitivity, advancing DR can easily become unmanageable, while long-lasting recovery from ADR may be achievable in less than two months with efficient BP control and small ‘repairs’ to blood vessels. These ‘repairs’ lead to *modest* shrinkage in hole diameters, and to much diminished leakage from shrunken holes. It is speculated that *long-term sustained* recovery from ADR may be greatly assisted by treatments T2 (vitamin B1) and T3 (vitamin D). These vitamins may induce holes shrinkage, which needs only be modest to be effective! In some diabetics already blinded by ADR; treatments T1-T5 may, hopefully, succeed in restoring their sight, since this only entails pumping fluids out of very thick retinas.

## References

1. Dirani M. Out of sight. A report into diabetic eye disease in Australia. Australia: Co-published by the Baker IDI Heart and Diabetes Institute and the Centre for Eye Research; 2013. Available from: <https://www.cera.org.au/wp-content/uploads/2015/11/OutOfSightReport.pdf>.
2. Lee R, TY Wong, C Sabanayagam. Review: Epidemiology of diabetic retinopathy, diabetic macular edema and related vision loss. *Eye Vis.* 2015;2(17):1-25. doi: 10.1186/s40662-015-0026-2.
3. Wu G. Diabetic retinopathy: The essentials. 1st ed. Philadelphia: Lippincott Williams & Wilkins; 2010.
4. Maturi RK, Walker JD, Chambers RB. Diabetic retinopathy for the comprehensive ophthalmologist. 2nd ed. Fort Wayne: Deluma Medical Publishers; 2015. Available from: <http://www.drcobook.com/download.php>.
5. American Optometric Association. Diabetic Retinopathy [Internet]. St. Louis (MO); c2018 American Optometric Association. Available from: <https://www.aoa.org/patients-and-public/eye-and-vision-problems/glossary-of-eye-and-vision-conditions/diabetic-retinopathy>
6. Chan A, Duker JS, Ko TH, Fujimoto JG, Schuman JS. Normal macular thickness measurements in healthy eyes using stratus optical coherence tomography. *Arch Ophthalmol.* 2006;124(2):193-198.
7. Browning DJ. The relationship between OCT-measured central retinal thickness and visual acuity in diabetic macular edema. *Ophthalmology.* 2007;114 (3):525-536.
8. Duan XR, Liang YB, Friedman DS, et al. Normal macular thickness measurements using optical coherence tomography in healthy eyes of adult Chinese persons: the Handan Eye Study. *Ophthalmology.* 2010;117(8):1585-1594.
9. Nagra M, Gilmartin B, Thai NJ, Logan NS. Determination of retinal surface area. *J Anat.* 2017; doi:10.1111/joa.12641.
10. Caro CG, Pedley TJ, Shrouter RC, Seed WA. The mechanics of the circulation. 2nd ed. Cambridge: Cambridge University Press; 2012. Chapter 13, The systemic microcirculation.
11. Batchelor GK. An introduction to fluid dynamics. 3rd ed. Cambridge: Cambridge University Press; 2000. Chapter 4, Flow of a uniform compressible viscous fluid.
12. da Silva AVB, Gouvea SA, da Silva APB, et al. Changes in retinal microvascular diameter in patients with diabetes. *Int J Gen Med.* 2015;8:267-273.
13. Tan PE, Balaratnasingam C, Xu J, et al. Quantitative comparison of retinal capillary images derived by speckle variance optical coherence tomography with histology. *Invest Ophthalmol Vis Sci.* 2015;56(6):3989-3996.
14. Wang Q, Kocaoglu OP, Cense B, et al. Imaging retinal capillaries using ultra- high-resolution optical coherence tomography and adaptive optics. *Invest Ophthalmol Vis Sci.* 2015;52(9):6292-99.
15. Lombardo M, Parravano M, Serrao S, Ducoli P, Stirpe M, Lombardo, G. Analysis of retinal capillaries in patients with type 1 diabetes and non proliferative diabetic retinopathy using adaptive optics imaging. *Retina - J Ret Vit Dis.* 2013; 33(8):1630-1639
16. Kundu PK, Cohen IM. Fluid Mechanics. Cambridge, MA: Academic Press; 2007. Chapter 17, Introduction to Biofluid Mechanics.
17. Munson BR, Okiishi TH, Huebsch WW, Rothmayer AP. Fluid Mechanics. 7th ed. Wiley; 2013.
18. Muraoka Y, Tsujikawa A, Kumagai K, et al. Age- and hypertension-dependent changes in retinal vessel diameter and wall thickness: an optical coherence tomography study. *Am J Ophthalmol.* 2013;156(4):706-714.
19. Rim TH, Choi YS, Kim SS, et al. Retinal vessel structure measurement using spectral-domain optical coherence tomography. *Eye.* 2016;30(1):111-119.
20. Thornalley PJ, Babaei-Jadidi R, Al Ali H, et al. High prevalence of low plasma thiamine concentration in diabetes linked to a marker of vascular disease. *Diabetologia.* 2007;50(10):2164-2170.
21. Rabbani N, Alam SS, Riaz S, et al. High-dose thiamine therapy for patients with type 2 diabetes and microalbuminuria: a randomised, double-blind placebo-controlled pilot study. *Diabetologia.* 2009;52(2):208-212.

22. Beltramo E, Berrone E, Tarallo S, Porta M. Effects of thiamine and benfotiamine on intracellular glucose metabolism and relevance in the prevention of diabetic complications. *Acta Diabetol.* 2008;45(3):131-41.
23. BBC NEWS Article. Diabetes Problems 'Vitamin Link' [Internet]; c2018 [Last updated 7 August 2007]. Available from: <http://news.bbc.co.uk/2/hi/health/6935482.stm>
24. Page, GL, Laight D, Cummings MH. Thiamine deficiency in diabetes mellitus and the impact of thiamine replacement on glucose metabolism and vascular disease. *Int J Clin Pract.* 2011;65(6):684-90.
25. Cinici E, Ahiskali I, Cetin N, et al. Effect of thiamine pyrophosphate on retinopathy induced by hyperglycemia in rats: A biochemical and pathological evaluation. *Indian J Ophthalmol.* 2016;64(6):434-439.
26. Hammes HP, Du X, Edelstein D, et al. Benfotiamine blocks three major pathways of hyperglycemic damage and prevents experimental diabetic retinopathy. *Nat Med.* 2003;9(3):294-299.
27. Mukherjee C, Wilcox M, Elsherbiny S. Does vitamin D deficiency affect diabetic retinopathy?: A primary care survey and literature review. *EC Ophthalmol.* 2016;4(1):451-458.
28. Payne JF, Ray R, Watson DG, et al. Vitamin D insufficiency in diabetic retinopathy. *Endocr Pract.* 2012;18 (2):185-103.
29. Millen AE, Meyers KJ, Liu Z, et al. Association between vitamin D status and age-related macular degeneration by genetic risk. *JAMA Ophthalmol.* 2015;133 (1):1171-1179.
30. Richer SP, Pizzimenti JJ. The importance of vitamin D in systemic and ocular wellness. *J Optim.* 2013;6(3):124-133.
31. Elblbesy MA, Hereba AR, Shawki MM. Effects of aspirin on rheological properties of erythrocytes in vitro. *Int J Biomed Sci.* 2012;8(3):188-193.
32. Vekasi J, Koltai K, Gaal V, Toth A, Juricskay I, Kesmarky G. The effect of aspirin on hemorheological parameters of patients with diabetic retinopathy. *Clin Hemorheol Microcirc.* 2008;39(1-4):385-389.
33. Do DV, Wang X, Vedula SS, et al. Blood pressure control for diabetic retinopathy. *Cochrane Database Syst Rev.* 2015;1:CD006127. doi: 10.1002/14651858.CD006127.pub2.
34. Sheps SG. Mayo Clinic Article. Caffeine: How does it affect blood pressure? [Internet]; [Last updated 19 Oct 2017]. Available from: <https://www.mayoclinic.org/diseases-conditions/high-blood-pressure/expert-answers/blood-pressure/faq-20058543>



# Condensation on intraocular lenses during vitrectomy: effect of perfluorocarbon liquids

Yann J. Dacquay<sup>1</sup>, Joseph R. Lee<sup>2</sup>, Andrea Govetto<sup>1</sup>, Matthias Elgeti<sup>3</sup>, Wayne L. Hubbell<sup>3</sup>, Pirouz Kavehpour<sup>2</sup>, Jean-Pierre Hubschman<sup>1</sup>

<sup>1</sup>Retina Division, Stein Eye Institute, David Geffen School of Medicine, University of California, Los Angeles, Los Angeles, CA, USA; <sup>2</sup>UCLA Engineering, Mechanical and Aerospace Engineering, University of California, Los Angeles, Los Angeles, CA, USA; <sup>3</sup>Department for Chemistry and Biochemistry, Stein Eye Institute, David Geffen School of Medicine, University of California, Los Angeles, Los Angeles, CA, USA

## Abstract

**Purpose:** To evaluate whether perfluorocarbon (PFO) liquids can exacerbate condensation on intraocular lenses (IOL).

**Methods:** Two separate experiments were carried out. In the first experiment, a two-segment chamber was constructed out of glass and acrylic panels to serve as an *in-vitro* eye model. The chamber was placed on a non-activated cooling plate with two IOLs of the same material, one in each segment. 2.0 ml of PFO and/or water for the control were placed in the respective receptacle. The cooling plate was then activated to the desired temperatures. Condensation on the lenses was visually assessed via high-definition ultra-zoom camera by trained observers for three temperatures and three IOL materials.

In the second experiment, Fourier transform infrared (FTIR) spectroscopy was employed to determine the composition of the droplets forming after condensation.

**Results:** The presence of PFO liquid in a closed chamber exacerbates the intensity and likelihood of condensation on all intraocular material types. Condensation of PFO on surfaces in the presence of water was confirmed with FTIR spectroscopy by the isolation of specific absorption bands. Furthermore, material type also affects the characteristics of condensation, with silicone lenses inducing the fastest rate and intensity of condensation.

---

**Correspondence:** Jean-Pierre Hubschman, Stein Eye Institute, David Geffen School of Medicine, University of California, Los Angeles, 100 Stein Plaza Driveway, Los Angeles, CA 90095, USA. E-mail: hubschman@jsei.ucla.edu

---

*Conclusions:* Our study shows that the presence of perfluoro-n-octane is a significant factor in the formation of condensation on the posterior surface of IOLs when performing vitrectomy in a pseudophakic patient with posterior capsulotomy.

## 1. Introduction

The frequency of cataract surgeries has been consistently increasing in the last 20 years.<sup>1</sup> Projections estimate the total number of persons with cataracts will rise to 30 million by 2020, while the number of pseudophakic/aphakic persons will increase to 9.5 million.<sup>1</sup> However, cataract surgery is not risk free. It is known that cataract surgery results in a 5.5 times greater risk of developing rhegmatogenous retinal detachment (RRD).<sup>2</sup> Surgical treatment of RRD frequently involves the use of perfluoro-n-octane liquid (PFO) during pars plana vitrectomy (PPV). In our own surgical experience, use of PFO on pseudophakic patients with a posterior capsulotomy may accelerate IOL surface condensation during fluid-air exchange (FAX), leading to a deteriorated view of the fundus and limiting the surgeon's ability to safely operate.

Condensation on the posterior surface of an IOL during FAX in the presence of a posterior chamber intraocular lens (PCIOL) after posterior capsulotomy or in the presence of an anterior chamber IOL (ACIOL) has been previously reported.<sup>5-12</sup> However, there is little data in the literature that addresses whether condensation on IOLs is altered by the presence of PFO. The purpose of this study is to determine whether PFO affects condensation on IOL surfaces.

## 2. Materials and methods

Two separate experiments were carried out. In the first experiment, a high-definition ultra-zoom camera was used to confirm the presence of condensation on three different types of IOLs placed in a closed acrylic and glass chamber. In the second experiment, we employed FTIR spectroscopy to determine the composition of the droplets forming on the surface of the lens.

### 2.1. First experiment: high-definition ultra-zoom camera

Three IOLs were tested, one in polymethylmethacrylate (Multiflex™ III PMMA Single-Piece IOL, model MTA2UO, Alcon Laboratories, Fort Worth, TX, USA) one in acrylic (ACRYSOF® Single-Piece IOLS, model SA60AT, Alcon Laboratories, Fort Worth, TX, USA), and one in silicone (Elastic Silicone IOL, model AA4204VL, STAAR® SURGICAL, Monrovia, CA, USA). The PFO liquid used was PERFLUORON® Liquid 8065900163 (Alcon Laboratories, Fort Worth, TX, USA).

A chamber was constructed from glass and acrylic panels to serve as an *in-vitro* eye model. Both chambers were divided into two separate compartments (Fig. 1).

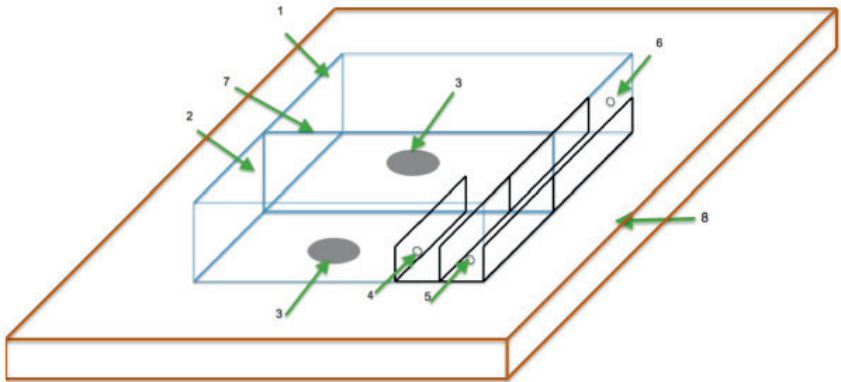


*Fig. 1.* Scheme of the chamber used in the first experiment. 1. Chamber B; 2. Chamber A; 3. IOL; 4. PFO dispensary dish injection site/dish; 5. Water dispensary dish injection site/dish; 6. Water-only dispensary dish injection site/dish; 7. Chamber divider; 8. Cooling/heating plate.

In the test compartment (chamber A), two small containers were fabricated to accommodate 2.0 ml of water and 2.0 ml of PFO, respectively, with a vacant anterior space for IOL placement. The control compartment (chamber B) had one container, which accommodated 2.0 ml of water, with a vacant anterior space for IOL placement. Two holes were drilled on each side of the chambers to allow for injections of PFO and water into their respective dishes, which were later covered with sealing tape during the trials. The IOLs were placed on a controlled temperature cooling platform, while chamber edges were sealed to assure adequate seal and isolation from the external environment. The chamber was then placed over the IOL, at which time the cooling plate could be activated to a desired temperature. The temperature of the cooling platform (custom built) was monitored by a K-type thermocouple (Model: 39658-K Atkins Technical Inc., Gainesville, FL, USA). A high-definition ultra-zoom camera (LW-1.3-G-1394-M, Imaging Solutions Group, Fairport, NY, USA) was placed above the chamber to record images of the IOL. Recordings of the time of initial condensation and maximum condensation of the IOLs in test and control containers were taken. Prior to the recording of time point data, two observers were asked to run 20 trials to become proficient in recognizing initial and maximum condensation. After each trial, the lenses were plasma cleaned using (Model: PDC-32G, Harrick Plasma, Ithaca, NY, USA). In vitro experiments, IOLs from different materials were tested twice at 10°C, 15°C, and 20°C, resulting in 18 trial runs for each chamber and a total of 36 trials. Images were taken, and time points were recorded immediately at the observation of initial and maximum condensation. We measured the relative humidity using a relative humidity sensor (Model: RH32S-C2, Omega, Stamford, CT, USA), finding the test and control containers having humidity levels within 1% of each other at varying temperatures. Humidity levels for temperatures 10°C, 15°C, and 20°C were 41.0%, 50.0%, and 67.0%, respectively.

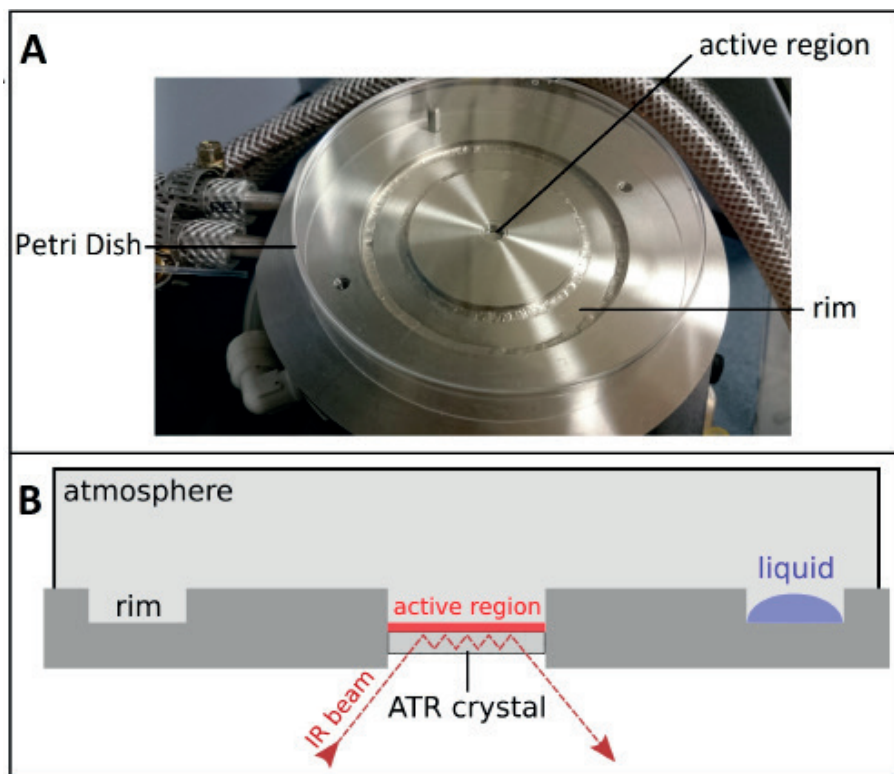


Fig. 2. FTIR spectrometer. (A) Photograph of the rim and active region of the measuring chamber, covered by a Petri dish to create closed and controlled environment. (B) Liquids (PFO and water) were placed either directly on the ATR crystal or in the surrounding rim.

## 2.2. Second experiment: FTIR spectroscopy

FTIR is routinely used to identify compounds based on their molecular vibrations with very high accuracy.<sup>13,14</sup> The setup used in our investigation is an attenuated total reflection (ATR) system (BioATRCeII, Harrick, NY, USA) and a dry air purged FTIR spectrometer (Tensor 27, Bruker Corp., MA, USA). Fluids can be placed either directly on the ATR crystal or into a rim surrounding the crystal. An atmosphere of approximately 50 mL volume enclosing crystal and surrounding rim was accomplished using the lid of a Petri dish (Fig. 2).

Reference spectra of water and PFO were recorded placing 20  $\mu\text{L}$  of the respective liquid on the ATR crystal. To investigate condensates of vapor formed during the experiment, water, PFO, or both were placed into the surrounding rim. In all FTIR experiments the ATR crystal and surrounding rim was cooled to 15°C by a temperature controlled circulating water bath.

### 3. Results

#### 3.1. First experiment: high-definition ultra-zoom camera

In chamber B (water-only chamber), condensation was observed in 0 out of 18 trials for all temperatures and lens materials. In chamber A (PFO and water chamber), condensation was observed in 18 out of 18 trials for all temperatures and material types.

*In-vitro* findings show that silicone-based lenses consistently had the fastest time of condensation throughout all temperature ranges when compared to PMAA and acrylic lenses. Condensation on silicone lenses at 10°C occurred 3.19 minutes prior PMAA and acrylic materials, 3.36 minutes prior at 15°C, and 8.26 minutes prior at 20°C. Similarly, maximum condensation occurred faster in silicone IOLs. Disregarding an outlier result of maximum condensation occurring after 45 minutes on an acrylic lens, we found that silicone lenses compared to PMAA and acrylic lenses reached maximum condensation an average of 14.71 minutes earlier at 10°C, 6.44 minutes earlier at 15°C, and 3.24 minutes after at 20°C.

#### 3.2. Second experiment: FTIR spectroscopy

Two spectral regions were investigated (Fig. 3A and B): Between 3500 and 3000  $\text{cm}^{-1}$ , the O-H stretching vibration of water causes a broad and intense absorption band (Fig. 3B, blue line). The fingerprint region (1350-1100  $\text{cm}^{-1}$ ) facilitates unequivocal identification of almost all materials by their specific vibrations; e.g., PFO causes a

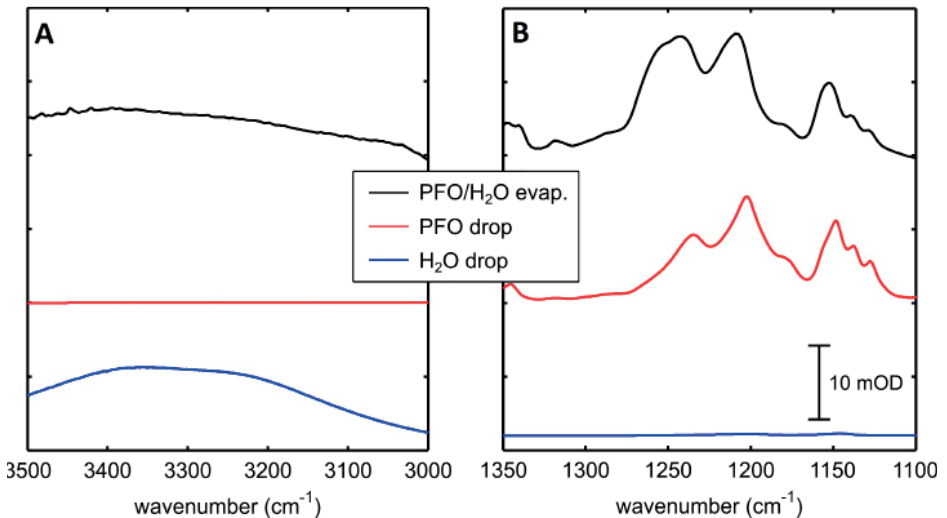


Fig. 3. Spectral regions analyzed. PFO and H<sub>2</sub>O absorption bands. (A) Between 3500 and 3000  $\text{cm}^{-1}$  (O-H stretching vibrations). (B) Between 1350 and 1100  $\text{cm}^{-1}$  (fingerprint region).

characteristic pattern of C-F vibrations when a drop is placed directly on the crystal (red line). When water and PFO are simultaneously placed into the rim surrounding the ATR crystal, after ~15 min a combination of both the H<sub>2</sub>O and PFO spectra is observed (black line). The above results prove that PFO and water are both present on the ATR crystal after evaporation and condensation of both liquids.

## 4. Discussion

A clear, unobstructed view of the posterior segment is required during retinal surgeries. It has been previously reported that visualization could be compromised by the presence of condensation on the posterior surface of ACIOL or PCIOL in the presence of a posterior capsulotomy.<sup>5-12</sup> However, there is little data on whether the presence of PFO may alter the characteristics of condensation. The purpose of this study is to determine if PFO affects condensation on IOL surfaces.

In the present report, it was demonstrated that PFO affects the occurrence, rate, and intensity of condensation on IOL surfaces. Observers were not able to appreciate visible condensation on the IOLs exposed to the water-only chamber, but consistently recorded condensation on the IOLs in the PFO chamber. Furthermore, the study demonstrates that lens material also affects rates and intensities of condensation, with silicone oil lenses being the most conducive in facilitating condensation, which supports previous reports.<sup>7</sup> The condensation of PFO in presence of water was confirmed by FTIR spectroscopy, which recorded the characteristic spectra of absorption of both PFO and water over the ATR crystal.

Condensation was clearly visible on lenses in the presence of PFO when compared to lenses in the water-only chamber (Fig. 4A and B).

The mechanism for these findings is based on the formation of water vapors and condensation on the IOLs.<sup>15-16</sup> During film-wise condensation, the interfacial tension

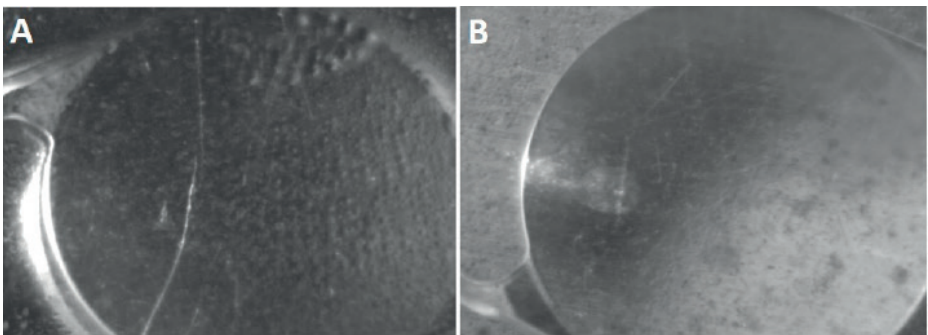


Fig. 4. High-definition photograph of silicone IOL. (A) Silicone lens in the PFO filled chamber at 10°C after 20 minutes; condensation is appreciated. (B) Silicone lens in the water-only chamber at 10°C after 20 minutes; no condensation can be appreciated.

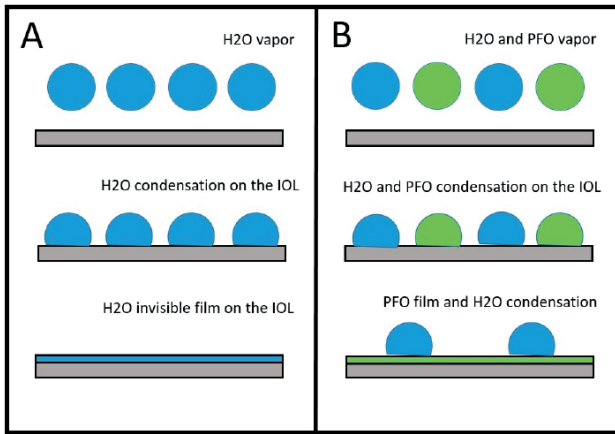


Fig. 5. Interaction between H<sub>2</sub>O and perfluorocarbon at the surface of the IOL. (A) Presence of H<sub>2</sub>O only. H<sub>2</sub>O condensates on the IOL, forming an invisible film without the appearance of fog. (B) Presence of H<sub>2</sub>O and PFO. PFO wets on the surface of the lens, forming a thin film due to its very low surface tension. Water cannot wet on the lens and condensates on top of the PFO film, causing the fog.

between water and the IOL allows water to fully wet the surface, creating a uniform and invisible film on the surface of the IOL (Fig. 5).<sup>11</sup>

However, water in the presence of PFO cannot form film-wise condensation, resulting in droplet formations on the IOL. The lower surface tension of PFO (14.2–15 dyne/cm) allows PFO to preferentially wet the surface of the IOL, which acts as a barrier between IOL surface and water (74 dyne/cm). Water vapors form on top of the PFO film, and due to the interactions between water and PFO, droplets are appreciated. It should be noted that the choice of temperatures (10°C, 15°C, and 20°C) are to show the effect of concurrent condensation of PFO and water on IOL as a function of temperature. The authors tested voluntary lower temperature than found in classic clinical settings to “expedite” the formation of fog; the lower IOL temperatures produce larger drops at faster rates. However, the physics of the fogging process remains the same. These findings are consistent with our intraoperative experience, in which IOL condensation occurs more easily when PFO is being used.

Different lens materials have different interfacial relationships with PFO and water, resulting in varying intensities of condensation. The varying rates and intensities of condensation found on PMMA, acrylic, and silicone IOLs are due to the differences in the materials surface free energy. Surface free energy can be measured with contact angle as a means to quantify hydrophobicity. Contact angle is defined as the angle between the material surface and a tangent on the surface of a droplet. Silicone (114.1°) has the largest contact angle, followed by hydrophobic acrylic (88.7°) and PMMA (77.1°).<sup>17</sup> Our findings indicate that materials with greater

surface free energy correlate with greater intensities of condensation. Silicone has the greatest rate and intensity of condensation, followed by acrylic and PMMA lenses. Based on our findings, PFO has the potential to exacerbate condensation on acrylic, silicone, and PMAA IOLs by acting as a buffer between water droplets and the surface of the IOL, not allowing film-wise condensation. We conclude that PFO increases the risk of condensation on the posterior surface of IOLs, regardless of material type. These findings are relevant, as surgeons utilizing PFO in pseudophakic patients with posterior capsulotomies increase the risk of operating with a deteriorated view of the fundus, which can lead to intraoperative complications.

## 5. Summary

Condensation on the posterior surface of an IOL in the presence of a posterior capsulotomy results in a deteriorated view of the retina. A diminished view of the retina can result in surgical complications, as unobstructed visualization of the posterior segment of the eye is required in various retinal surgeries. The results of this study indicate that there is a significant correlation between the presence of PFO and an increased occurrence and intensity of condensation. Furthermore, our study demonstrates that silicone IOLs are the most conducive lenses for condensation, which supports the findings of previous studies. Future studies could employ mathematical modeling in identifying, quantifying, and characterizing the surgical conditions and material properties that will help reduce surgical complications associated with PFO and IOLs.

## Acknowledgements

None of the authors have proprietary interest.

## References

1. Congdon N, Vingerling JR, Klein BE, et al. Eye Diseases Prevalence Research Group. Prevalence of cataract and pseudophakia/aphakia among adults in the United States. *Arch Ophthalmol.* 2004;122(4):487-494.
2. Rowe JA, Erie JC, Baratz KH, et al. Retinal detachment in Olmsted County, Minnesota, 1976 through 1995. *Ophthalmology.* 1999;106:154-159.
3. Brazitikos PD, Androudi S, D'Amico DJ, MD, et al. Perfluorocarbon liquid utilization in primary vitrectomy repair of retinal detachment with multiple breaks. *Retina.* 2003;23(5):615-21.
4. Chang S, Ozmerit E, Zimmerman NJ, et al. Intraoperative perfluorocarbon liquids in the management of proliferative vitreoretinopathy. *Am J Ophthalmol.* 1998;106: 668-674.
5. Brazitikos, PR. Perfluorocarbon liquid utilization in primary vitrectomy repair of
6. retinal detachment with multiple breaks. *Retina.* 2003; 23:615-621.
7. Eaton AM, Jaffe GJ, McCuen BW 2nd, et al. Condensation on the posterior surface of silicone intraocular lenses during fluid-air exchange. *Ophthalmology.* 1995;102(5):733-736.
8. Hainsworth DP, Chen SN, Cox TA, et al. Condensation on polymethylmethacrylate, acrylic polymer, and silicone intraocular lenses after fluid-air exchange in rabbits. *Ophthalmology.* 1996;103(9):140-148.
9. Jaffe GJ. Management of condensation on a foldable acrylic intraocular lens after vitrectomy and fluid-air exchange. *Am J Ophthalmol.* 1997;124:692-693.
10. Kusaka S, Kodama T, Ohashi Y. Condensation of silicone oil on the posterior surface of a silicone intraocular lens during vitrectomy. *Am J Ophthalmol.* 1996;121:574-575.
11. Eaton AM, Jaffe GJ, McCuen BW II, et al. Condensation on the posterior surface of silicone intraocular lenses during fluid-air exchange. *Ophthalmology.* 1995;102:733-736.
12. Porter RG, Peters JD, Bourke RD. De-misting condensation on intraocular lenses. *Ophthalmology.* 2000;107:778-782.
13. Browning DJ, Fraser CM. Clinical management of silicone intraocular lens condensation. *Am J Ophthalmol.* 2005;139(4):740-742.
14. Stuart BH. In *Infrared spectroscopy: fundamentals and applications.* John Wiley & Sons, Inc.; 2005:71-93.
15. Stuart BH. In *Infrared spectroscopy: fundamentals and applications.* John Wiley & Sons, Inc.; 2005:95-111.
16. Moran MJ, Shapiro HN, Boettner DB, Bailey MB. *Fundamentals of engineering thermodynamics.* Dec 2010 Wiley; 7th edition
17. Bergman TL, Lavine AS, Incropera FP, et al. *Fundamentals of heat and mass transfer.* April 2011. Wiley; 7th edition.
18. Baillif S, Baziard-Mouysset G, Roques C, et al. Calculation of intraocular lens surface free energy and its components from contact angle measurements. *Ophthalmic Res.* 2013;50(3):165-173.